UNIVERSIDADE
BEIRA INTERIOR

Design of a Single Expansion Ramp Nozzle and Numerical Investigation of Operation at Over-Expanded Conditions

(Versão corrigida após defesa)

Jorge Filipe Suadate Correia de Magalhães

Dissertação para obtenção do Grau de Mestre em
Engenharia Aeronáutica
(Ciclo de estudos integrado)

Orientador: Prof. Doutor Francisco Miguel Ribeiro Proença Brójo

Covilhã, novembro de 2021

Dedicatory

Dedicated to my parents, for all their love and support over the years.

Acknowledgement

A thank you to professor Francisco Brójo, for all his help and availability throughout this dissertation.

To the friends who accompanied me along this unforgettable journey, for all the moments and memories we shared.

And last but not least, to my parents Luis Magalhães and Samai Suadate, for all the help and support over all these years, without whom none of this would be possible.

Resumo

Na presente tese, um bocal de rampa de expansão única (SERN) é projetado e investigado. Um algoritmo de Python baseado no método das características é desenvolvido, o qual calcula o contorno otimizado de um bocal 2D supersónico caloricamente perfeito de comprimento mínimo, para expansão ideal dos gases, sem choques. Além disso, calcula também várias propriedades do escoamento no interior do bocal. Os resultados do algoritmo são coroborados pelos fundamentos teóricos, literatura prévia e simulações CFD, validando assim o código. A geometria otimizada de um SERN (com um Mach à saída de $M_E = 4$ e um coeficiente de expansão adiabática de $\gamma = 1,4$) é então obtida com recurso ao algoritmo, e truncada a 40% do seu comprimento sem perda significativa de tração, para integração viável num veículo. Um modelo numérico foi criado em ANSYS FLUENT 16.2, e validado com dados de uma prévia investigação experimental efetuada em SERN's. O modelo validado foi então aplicado ao SERN projetado neste estudo, onde várias simulações foram efetuadas em diferentes condições de operação. As simulações numéricas são resolvidas em regime permanente, 2D, utilizando o solver baseado em densidade e o modelo de turbulência $k-\varepsilon$ RNG. O Caso A simula a operação do SERN à altitude (22 km) e velocidade (Mach 4) de projeto, variando a razão de pressão do bocal (NPR) de 133,65 (projeto), 100, 75, 50 e 25. Ao NPR de projeto, observa-se uma expansão quase perfeita dos gases. À medida que o NPR é reduzido, a escoamento torna-se sobre-expandido, com a formação de ondas de choque incidentes à saída do bocal e ondas de choque refletidas a jusante, redução da velocidade do escoamento e contração da pluma do jato. Entre os NPR's 133,65 a 25, a tração, sustentação e momentos do SERN sofrem uma redução linear de 81,33%, 80,7% e 81,17%, respetivamente. O Caso B simula a operação do SERN a uma velocidade (0.4 Mach) e altitude (8 km) fora do ponto de projeto, variando o NPR de 4, 5, 6, 8, 10, 12, 15 até 20. Observa-se extrema sobre-expansão do escoamento e padrões de ondas de choque complexos, tais como o padrão de separação de choque restrito (RSS), incluindo a formação de uma bolha de recirculação na rampa, entre os pontos de separação e religação do jato principal, uma grande região de recirculação no flap, discos de Mach, estruturas de choque λ e cadeias de choque. Entre os NPR's 4 a 20, a tração, sustentação e momentos do SERN sofrem uma certa variação, com um aumento global de 38,2%, 5,27% e 42,3%, respetivamente.

Palavras-chave

Método das Características, Otimização do Design de Bocal, Bocal de Comprimento Mínimo, Bocal de Rampa de Expansão Única, Separação Sobre-Expandido, Padrão de Separação de Escoamento, Onda de Choque, Simulação Numérica, Algoritmo, Python, ANSYS FLUENT

Abstract

In the present thesis, a single expansion ramp nozzle (SERN) is designed and investigated. A Python algorithm based on the method of characteristics (MOC) is developed, which generates the optimised contour of a 2D supersonic calorically perfect minimum length nozzle (MLN), for ideal shock-free flow expansion, and calculates various flow-field properties within the nozzle. The algorithm results shows good agreement with theoretical background, previous literature and CFD simulations, thus validating the code. An optimised SERN geometry is then designed using the algorithm, operating with an exit Mach number of $M_E = 4$ and a specific heat ratio of $\gamma = 1.4$. The optimal geometry is truncated at 40% of its length for viable integration into a vehicle, without significant loss in thrust. A numerical framework is created in ANSYS FLUENT 16.2, and validated by comparison with data from previous experimental investigations conducted on SERN's. The validated model is then applied to the SERN designed in this study, where various simulations of design and off-design conditions are conducted. The numerical simulations are solved in a steady-state 2D environment, using the density-based solver and the $k - \varepsilon$ RNG turbulence model. Case A simulates SERN operation at design altitude (22 km) and speed (Mach 4), through nozzle pressure ratios (NPR's) 133.65 (design), 100, 75, 50 and 25. Near perfect expansion of the gases is achieved at the design NPR. As the NPR is reduced, the flow becomes over-expanded, with the formation of incident shock-waves at the nozzle exit and reflected shock-waves further downstream, reduction of exhaust flow speed and contraction of the exhaust plume. From NPR = 133.65 to NPR = 25, the SERN's thrust, lift and moments suffer a linear reduction of 81.33%, 80.7% and 81.17%, respectively. Case B simulates SERN operation at off-design speed (Mach 0.4) and altitude (8 km), through NPR's 4, 5, 6, 8, 10, 12, 15 and 20. Severe over-expanded flow and complex shock-wave patterns are observed, such as the restricted shock separation (RSS) pattern, including separation and reattachment of the main jet to the ramp, formation of a separation bubble on the ramp, a large re-circulation region on the flap, Mach disks, λ shock structures and shock-trains. From NPR = 4 to NPR = 20, the SERN's thrust, lift and moments varied to some degree, with an overall increase of 38.2%, 5.27% and 42.3% respectively.

Keywords

Method of Characteristics, Nozzle Design Optimisation, Minimum Length Nozzle, Single Expansion Ramp Nozzle, Over-expanded Separation, Flow Separation Pattern, Shock-Wave, Numerical Simulation, CFD, Algorithm, Python, ANSYS FLUENT

Contents

List of Figures

List of Tables

Nomenclature

$\bar{\bar{\tau}}$	Stress tensor	Pa
γ	Specific Heat Ratio	–
μ	Mach Angle	°
ν	Prandtl-Meyer Angle	°
ω	Specific Dissipation Rate	s^-1
Φ	Velocity Potential	–
Φ_d	Viscous Dissipation term	–
ρ	Density	kgm^{-3}
θ	Flow Turning Angle	°
ε	Turbulent Dissipation Rate	m^2/s^3
$\vec{F}$	Force Vector	N
A	Area	m^2
a	Speed of Sound	m/s
C	Characteristic	–
C	Turbulence Model Constants	–
c_p	Specific Heat Capacity at Constant Pressure	$Jkg^{-1}K^{-1}$
c_v	Specific Heat Capacity at Constant Volume	$Jkg^{-1}K^{-1}$
D	Denominator	–
G	Turbulence Kinetic Energy Generation	–
I	Unit Tensor	Pa
i	Internal Thermal Energy	J

K	Constant	–
k	Thermal Conductivity	W/mK
M	Mach Number	–
M_w	Molecular Weight	$kg/kgmol$
N	Numerator	–
n	Number of Characteristic Lines	–
p	Pressure	Pa
q	Dynamic Pressure	N/m^2
q	Heat	Jkg^{-1}
R	Universal Gas Constant	$m^2s^{-2}K^{-1}$
S	User-Defined Source Terms	–
s	Specific Entropy	$Jkg^{-1}K^{-1}$
Sa	Stream Thrust	–
T	Temperature	K
u	Velocity Horizontal Component	m/s
U^+, U^*	Dimensionless Velocity	–
V	Velocity	m/s
v	Velocity Vertical Component	m/s
x	Distance Along x axis	m
y	Distance Along y axis	m
y^+, y^*	Dimensionless Distance to the Wall	–
Y_M	Contribution of the Fluctuating Dilation	$kg/(ms^3)$

List of Acronyms

C-D	Convergent-Divergent
CAD	Computer Aided Design
CFD	Computational Fluid Dynamics
FSS	Free Shock Separation
GEN	Gradual Expansion Nozzles
MD	Mach Disk
MLN	Minimum Length Nozzles
MOC	Method of Characteristics
NAR	Nozzle Area Ratio
NPR	Nozzle Pressure Ratio
ODE	Ordinary Differential Equations
PDE	Partial Differential Equations
PIV	Particle Image Velocimetry
RANS	Reynolds-Averaged Navier-Stokes
RBCC	Rocket-Based Combined Cycle
RSS	Restricted Shock Separation
SERN	Single Expansion Ramp Nozzle
SIS	Shock-Induced Separation
SST	Supersonic Transport
TBCC	Turbine-Based Combined Cycle
TIC	Truncated Idealised Contoured
TOC	Thrust-Optimised Contoured
TP	Triple Point

Chapter 1

Introduction

1.1 Motivation

Since the dawn of aviation, mankind has been pushing the boundaries to fly further, faster and higher.

We have come a long way since the Wright brothers first successful flight, and over the last 100 years there has been an exponential growth in the aerospace industry the technology, fuelled by the desire of achieving more, better and faster.

In 1930, cruising roughly at 160 km/h, a flight from New York to Los Angeles took a total of 36 hours with 11 stops along the way! Nowadays, cruising at 0.83 the speed of sound, the same route is done nonstop in about 5 hours.

For several years, supersonic (faster than the speed of sound (Mach ≥ 1)) flight was deemed impossible. Because of the complex phenomena that occurred at speeds near Mach 1, such as strong shock-waves, this sound barrier was thought to be impenetrable. However, in 1947 history was made when the Bell X-1 broke to the sound barrier and was able to achieve a top speed of Mach 1.06, making it the first aircraft to fly at supersonic speeds.

Thereafter, the supersonic flight technology boomed in the military sector, with many military aircraft capable of supersonic flight being built, some capable of achieving speeds up to Mach 2.5.

The first supersonic transport (SST) was the Soviet Tupolev Tu-114 in 1969, which began by flying mail. The SST passenger-carrying commercial airplane, the well known Concorde, made its first transatlantic crossing in 1973, and was able to fly from New York to London in just 3 hours and 15 minutes, with a maximum cruise speed of Mach 2.04 [15]. It was retired in 2003, and since then has been no civilian SST in service.

The Lochheed SR-71 Blackbird, a military strategic reconnaissance aircraft developed in the 1960s during the Cold War and retired in 1998, remains to this date the fastest and highest flying air-breathing manned aircraft, with an astonishing record of flight at 85000 ft of altitude, and a top speed of approximately Mach 3.5 [16].

In the modern day, life is fast paced, and time is the most valuable asset. In recent years

there has been a increase in demand for high Mach and even hypersonic vehicles, for a wide range of applications, such as military purposes, commercial high supersonic an hypersonic travel, access to Earth orbit and even outer space.

Thus, technology must keep up with this demand in order to propel aviation and flight to the next level. In recent years, high supersonic and hypersonic air-breathing aircraft have become a growing topic of interest, leading to an increase in research about several aspects regarding the physics of such high speed flight.

Being one of the fields in aerospace that I am most interested in, and the believe that there is a lot to discover and improve, motivates me to contribute in some way to the research about such a fascinating realm of aviation.

1.2 Objectives

In high Mach / hypersonic air-breathing propulsion, the nozzle through which the high energy exhaust gases are expanded and accelerated is a vital component to the overall efficiency of the vehicle, and must be optimised in order to prevent losses and maximise its performance.

Thus, the main goal of this research thesis is the creation of an algorithm written in Python that can compute the optimised contour for the conceptual design of a 2D nozzle for such applications, through the Method of Characteristics (MOC). Then, Computational Fluid Dynamics (CFD) analysis of the designed nozzle are to be performed in ANSYS FLUENT, in order to evaluate its performance and phenomena that can occur at various design and off-design conditions.

To achieve the described objectives, the following tasks must be fulfilled:

1. Study of previous research on the topic, to acquire knowledge and understand the current state of the art;

2. Review of the theoretical fundamentals and techniques underling the research;

3. Creation of a Python algorithm able to compute the optimised nozzle contour;

4. Investigation of parameters affecting nozzle geometry and properties, using the created algorithm;

5. Construction of the computational domain and appropriate numerical model in ANSYS FLUENT for the CFD analysis of the nozzle geometry;

6. Evaluation the nozzle performance, and investigation of occurring flow phenomena at

various design and off-design conditions.

1.3 Thesis Layout

This thesis is divided in six chapters.

In the first chapter the motivations and objectives of the study are presented, as well as the overall structure of the document.

The second chapter focuses on the current state of the art of the technology related to high Mach / hypersonic air-breathing propulsion, with particular emphasis on the various types of nozzles employed.

The third chapter reviews various fundamental theoretical notions and foundations, mainly on compressible flow, the method of characteristics and computational fluid dynamics, essential for the comprehension of the work developed in this thesis.

In the forth chapter the methodology of the work is described, which encompasses the optimised nozzle design algorithm with its results and validation, the numerical simulation framework to be employed in the various simulations conducted in the study, as well as its validation, and the selected nozzle design and conditions to be tested.

In the fifth chapter, the results of the numerical simulations conducted are presented and analysed.

The conclusion in the last chapter summarises the work conducted throughout the study, with emphasis on the discussion of the results obtained. The limitations of the study are also presented, as well as a proposal for future work.

Chapter 2

State of the Art

2.1 Historical Perspective

High Mach and hypersonic flight is considered the next great advancement within the aviation industry. In recent decades it has been an important area of research interest in the aerospace sector due to its potential in military and civil applications.

There has been an increase in demand for commercial supersonic and hypersonic travel as aerospace companies have been looking to replace long haul subsonic flights with super and hypersonic aircraft designs that could be economically and environmentally viable. More aerospace companies are investing in new engine technologies and developing concept aircraft designs capable of supersonic and hypersonic travel. Even though this has been investigated for over half a century, there have been only few breakthroughs which have made hypersonic flight available on a commercial level. This is mainly due to the challenges ranging from structural demands, fuel economy, maintenance issues, direct operating costs, and supersonic combustion [17].

Historically, the approach to hypersonic flight research has spanned several decades with constant improvements in performance through improvements in aerodynamics, structures, and propulsion systems leading to successively higher flight speeds. For flight above Mach 3, the main representative was the Lockheed SR-71, which utilised Turbine-Based Combined Cycle (TBCC) engines to propel the aircraft. Powered by two Pratt and Whitney J-58 engines, the aircraft was capable of achieving Mach 3.5 flight speeds, making it the fastest air-breathing aircraft to take off under its own power [18].

Perhaps the most noteworthy aeronautical research effort in history is the rocket-powered hypersonic research aircraft X-15 that holds the record for the fastest manned aircraft achieving a speed of Mach 6.72. The structure of the aircraft was influenced by intercontinental missile development research being conducted at the time, and it was capable of reaching an altitude of over 350 000 ft, demonstrating that the pilots can fly rocket-powered vehicles from the Earth's atmosphere to the edge of outer space and returning with valuable data utilised in the design of succeeding aircrafts and spacecrafts [19].

The most of successful supersonic commercial transportation aircraft was the Concorde, a joint collaboration project between Britain and France which revolutionised commercial air travel by cutting down air journey time by half—bridging London and New York with only

a 3h15 flight time. At the same time efforts in the then Soviet Union resulted in the Tu-144 aircraft which was, however, less successful and short-lived. The Concorde was capable of Mach 2 cruise speeds, powered by four Rolls-Royce/Snecma Olympus 593 afterburning turbojets [20].

However, the significant fuel consumption coupled with escalating fuel prices and fears of another oil crisis caused its retirement as its popularity plummeted. Presently, there exists a large gap in the market, primarily business travellers, for the potential revival of supersonic, or better yet hypersonic travel. Focussing available resources on the design and development of airliners capable of achieving hypersonic cruise speeds can be achieved by extending the research on air breathing propulsion [21].

Nevertheless, high speed air travel seems to be reviving with aerospace companies like BOOM [22], Aerion [23] and Hermeus [24] leading the industry, contribution with major partnerships, technological advances and even scaled prototypes of high Mach / hypersonic aircrafts, with the goal of redefining air travel and pushing aviation to the next level.

2.2 High Mach / Hypersonic Air-Breathing Propulsion

Air-breathing high Mach and hypersonic propulsion can play a part in putting aircrafts into orbit or sustain flight within the atmosphere with lower weight and propulsion required compared to rockets, as the oxidiser (air) is taken from the environment as opposed to being carried on-board. Hypersonic air-breathing flight will potentially offer great advancements in reliability, reusability, as well as economical for high-speed atmospheric cruising. By removing the need to carry oxidisers, among other limitations rocket engines face, these proposed propulsion methods increase the possibility of achieving the desired range, payload and efficiency [17].

Several air-breathing propulsion methods like turbojet, turbofan, ramjets, and scramjets have been adopted in the past to utilize high-speed air-breathing flight. Conventional air-breathing engines, such as those associated with the present commercial aircraft, rely on rotational components for both starting and continued generation of thrust. Sustained hypersonic flight is associated with severe thermal, aerodynamic, and stress-related loading factors that hinder a turbine engine's ability to operate [25]. The limitations observed within the turbojet are that the maximum rotational speed of the rotor and the maximum temperature of the gases in front of the turbine affect the durability of the turbine blades. Consequently, engine reliability is risked during operation and the flight speed is limited [26].

Ramjets and Scramjets (supersonic combustion ramjet) appeared as a solution to this problem, taking advantage of the high-speed operational environment. This type of engines utilize the "ram" effect, by exploiting the high speeds and dynamic air pressure to compress the intake air, and thus, avoid the need for rotational components.

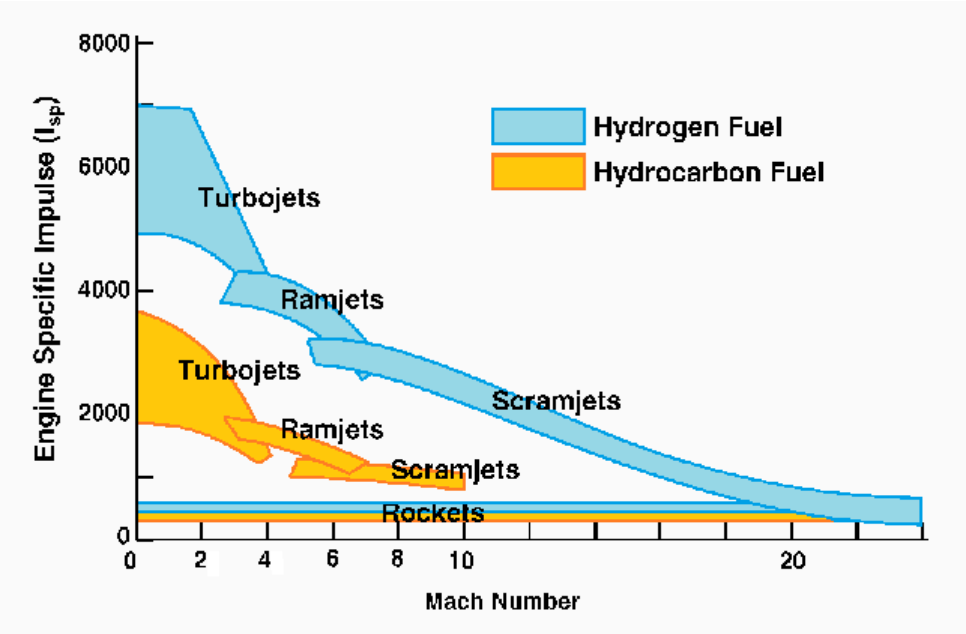

Figure 2.1: Operation envelopes and efficiency of different engine types [2]

Specific impulse (I_{sp}) can be used to compare efficiencies between various engine types and performance levels. In Fig 2.1, different engine types are shown on a graph Specific Impulse versus Mach Number, and it is clear that hydrogen is more efficient than hydrocarbon fuel. Also, it is clearly shown that at Mach numbers higher than 6-7, only rockets and scramjets are feasible, and scramjets are more advantageous with having higher specific impulse compared to rockets [27].

Ramjet engines have an operational regime of approximately Mach 2.5 to around Mach 5-6, relying on subsonic flow behaviour throughout the engine.

The scramjet is a variant of the ramjet engine and similarly relies on the vehicle's speed to compress the air prior to combustion. Scramjets are usually utilized at Mach 5 and above because of the ramjet's inability to overcome the drag above such speeds. In scramjets, the airflow remains supersonic as it passes through the engine including the combustor, whereas in the ramjet, flow is decelerated to subsonic velocity for combustion. A scramjet operates efficiently at hypersonic speeds and allows for supersonic combustion by compressing the incoming airflow without decelerating it below Mach 1 [28].

A typical scramjet consists of a converging inlet, isolator, combustion chamber, and a diverging nozzle. The basic scramjet schematic can be seen in Fig. 2.2

On the downside, these type of engines can only operate when the aircraft is already moving at a high enough speed, meaning other propulsion systems are necessary to accelerate the aircraft from take-off and through subsonic speed, until a speed where the ramjet or scramjet becomes operable is achived. Thus, air-breathing hypersonic aircraft require a scramjet system in a combined-cycle propulsion architecture that also involves conventional gas tur-

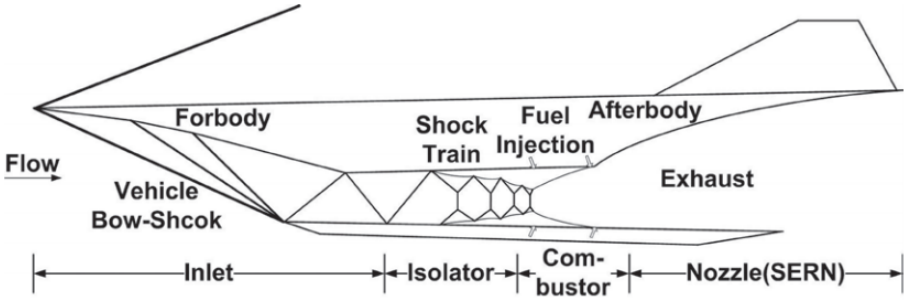

Figure 2.2: Simplified scramjet schematic diagram [3]

bines and ramjets. Such layout is called Turbine-Based Combined Cycle (TBCC). Another kind of combined cycle engine is the Rocket-Based Combined Cycle (RBCC), which usually has four operation modes: ejector-jet (Mach 0-3), ramjet (Mach 3-7), scramjet and rocket (Mach > 7) [29]. The Nozzle Pressure Ratio (NPR, the ratio of internal total pressure at the nozzle entrance to the static ambient pressure) of combined cycle engines can range from as little as 2 at low Mach numbers up to 600 or higher for hypersonic flight.

Combined cycle engines allow each engine type to operate within a different flight speed regime at which is optimized, and are required for successful operation throughout the hypersonic aircraft flight envelope [21].

2.3 Nozzles

A nozzle is a duct of varying cross-sectional area which has the purpose of accelerating the flow passing through it. The nozzle converts the flow's available thermal energy at the end of the combustor to kinetic energy by expanding the hot exhaust gases to the atmosphere. The nozzle also controls the direction of the exhaust flow, and generates thrust through the change in flow momentum and pressure.

Generally, supersonic nozzles are Convergent-Divergent (C-D), also called "De Laval" nozzles, after Carl G.P. De Laval, who first used such a configuration in his steam turbines in the late nineteenth century. In C-D nozzles, subsonic flow velocity increases until sonic conditions at the minimum area section, also known as nozzle throat, and then accelerates throughout the diverging section, as represented in Fig. 2.3.

Most of the gross nozzle trust, produced from jet momentum with additional thrust from pressure, will cause an imbalance between the throat static pressure and ambient pressure. In contrast to convergent nozzles, at high NPR, the C-D nozzle allows expansion to take place inside the nozzle to maximise the thrust being produced. The area ratio between the throat and the nozzle exit also impacts the flow significantly, known as Nozzle Area Ratio (NAR). Downstream of the throat, the nozzle gradually increases in the cross-sectional area, creating the characteristic parabolic bell profile, which allows the exhausted gases to expand, creating the required thrust [21].

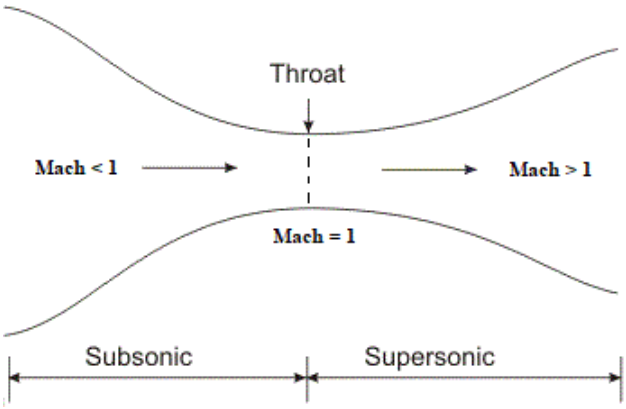

Figure 2.3: Flow through a C-D nozzle

Concepts like NPR, NAR and the nozzle thrust generation mechanism will be explained in detail in the next chapter.

In order to successfully design a nozzle, various geometric, structural and aerodynamical aspects must be taken into consideration, as well as the highly dynamic operational profile and flight envelope. If the nozzle were to always operate at the same ambient conditions, it would be relatively simple to select one optimum geometric design for maximum performance at such conditions. However, in reality the nozzle design must have a fairly acceptable performance at the off-design conditions that are comprised by the flight envelope, where various flow phenomena such as over-expansion and under-expansion can occur.

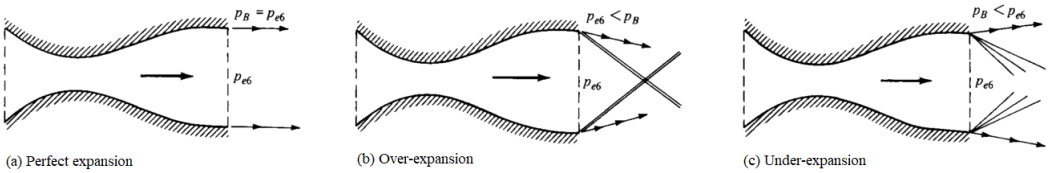

Figure 2.4: Flow regimes at nozzle exit [4]

Over- and under-expansion, depicted in Fig. 2.4, occur when the ambient pressure at which the nozzle is operating is either higher or lower, respectively, than the pressure at the nozzle exit. This will lead to complex flow phenomena where the flow tries to adjust itself to the conditions through a series of shocks and expansion waves, affecting nozzle performance. The physics behind these flow regimes, as well as shock and expansion waves will also be explained in more detail in the next chapter.

2.3.1 Geometric Configurations

2.3.1.1 Conical Nozzles

Historically, the shape of the diverging section of the nozzle has been primarily conical owing to the simplicity and the ease of construction. However, in time, a better understating of the aerothermodynamics of convergent-divergent nozzles has led to the substitution of the conventional conical nozzle with more sophisticated shapes in order to minimise fluid dynamic

losses [21].

Conical nozzles (Fig. 2.5) work on the principle of converting the exhausted gases into axial thrust, and perform best when the axial thrust is uniform throughout the nozzle axis [30].

Conical nozzles can be compared based on their divergence angle (α), which is the angle between the nozzle wall and the centerline.

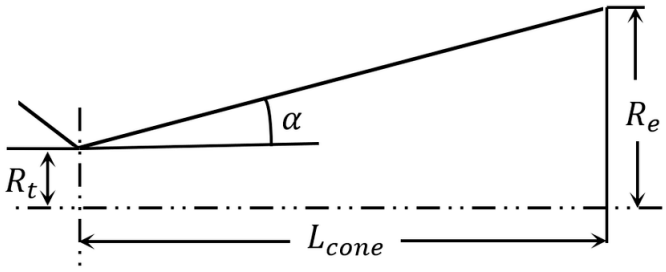

Figure 2.5: Conical nozzle geometry (axisymmetric with respect to centerline) [5]

Hence, smaller divergence angles (α) produce greater axial thrust because they maximise the axial component of the exhaust exit velocity, producing high specific impulse in the process. However, this does result in longer and heavier nozzle divergent sections, which leads to problems with installation. Shortening the nozzles with large divergence angles leads to divergence losses. In a conical divergent nozzle with a semi-angle (α), by the time the exhaust has travelled past the exit, the streamlines have diverged away from the axis of the jet, producing radial thrust instead [31]. Larger divergence angles reduce low altitude performance as high pressures lead to over-expansion, which in turn may lead to flow separation.

2.3.1.2 Contoured Nozzles

Bell-shaped nozzles are currently the most commonly utilised nozzle contour. Nozzle contouring in this case is tailored to yield certain desired pressure gradients to minimise flow separation, thus improving the performance over the simple cone nozzle.

Bell-shaped nozzles consist of two sections. The nozzle contours diverge at a relatively large angle near the throat and taper off further downstream. At the section near the nozzle exit the divergence angle is very small, almost parallel to the jet axis. This configuration allows a maximisation of the performance while minimising the weight, with the length of the nozzle being as much as 25% lower than the conical nozzle equivalent. This type of nozzle achieves the reduction of divergence by turning the flow to provide an axial flow, but typically exhibit one design point where they are most efficient at a given altitude of operation [30].

The bell nozzle basic geometry is provided in Fig. 2.6, with θ_i being the initial nozzle angle immediately downstream of the throat and θ_e the final nozzle exit angle. From these angles, the divergence loss factor, λ, can be calculated:

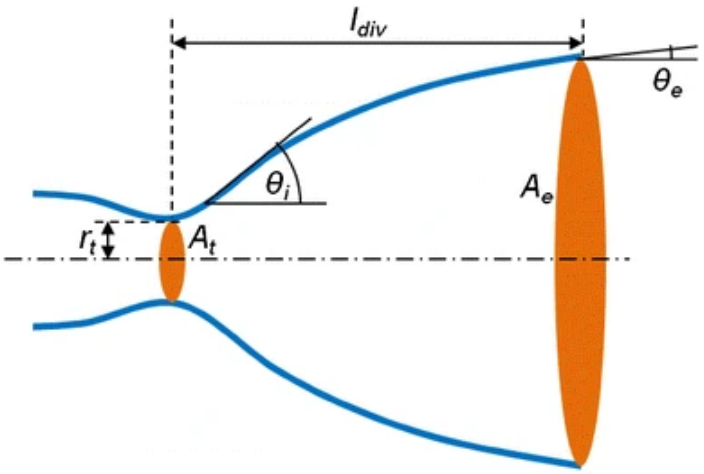

Figure 2.6: Bell nozzle geometry [6]

$$\lambda = \frac{1}{2}(1 + \cos\frac{(\theta_i + \theta_e)}{2}) \quad \textbf{(2.1)}$$

Truncated idealised contoured (TIC) nozzles are a class of bell-shaped nozzle developed to produce a virtually unidirectional exhaust profile. Computational methods to design such contours were developed already before the middle of the last century [32]. The walls of the contour curve near the throat region and become nearly parallel to the nozzle axis at the exit plane. However, the nozzle length ought to be equal to 50 times the throat radius in theory. In cases where this requirement cannot be met, for shorter nozzles, the flow is forced to straighten out earlier, causing a decrease in the nozzle efficiency [33]. Ideal contours are still in use for wind tunnel applications nowadays, where steady parallel flow is imperative, and the nozzle overall size isn't a constraint.

Thrust-optimised contoured (TOC) nozzles, proposed by Rao G. V. R. in 1959 [34] are a step further from TIC nozzles, where the near throat region has a sharp gradient of curve, producing an internal expansion wave at the throat, which corresponds to the greater expansion of the flow [35]. This type of nozzle design maximise the thrust produced while keeping nozzle length to a minimum.

Thus, supersonic contoured nozzles can be divided into two main types:

1. Gradual Expansion Nozzles (GEN);

2. Minimum Length Nozzles (MLN).

Gradual-expansion nozzles, such as the TIC, are typically used in applications where maintaining a high-quality flow at the desired exit conditions is of importance, for example, supersonic wind tunnels.

For other types of applications, such as rocket or aircraft nozzles, the large weight and length penalties associated with gradual-expansion nozzles make them impracticable. Therefore minimum-length nozzles, such as the TOC, which utilize a sharp corner to provide the initial flow expansion, are commonly used.

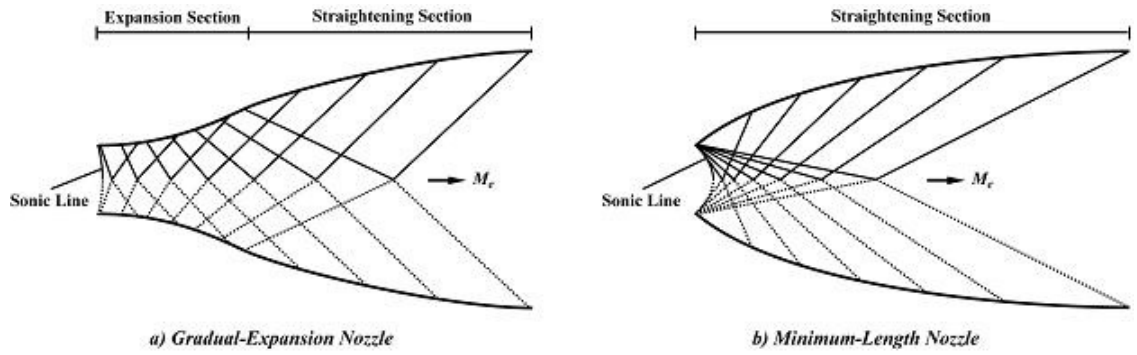

Figure 2.7: Supersonic contoured nozzles [7]

2.3.2 Single Expansion Ramp Nozzle

A single expansion ramp nozzle, or SERN, is a type of physical linear expansion minimum length nozzle where the flow pressure transfers work only on one side. Traditional nozzle geometries described up until now are axisymmetric, which means they exhibit symmetry of geometric and flow properties around the nozzle centerline axis. Unlike these traditional axisymmetric nozzles, a SERN is asymmetrical, thus enabling it to be treated as a two-dimensional (2D) geometry [36].

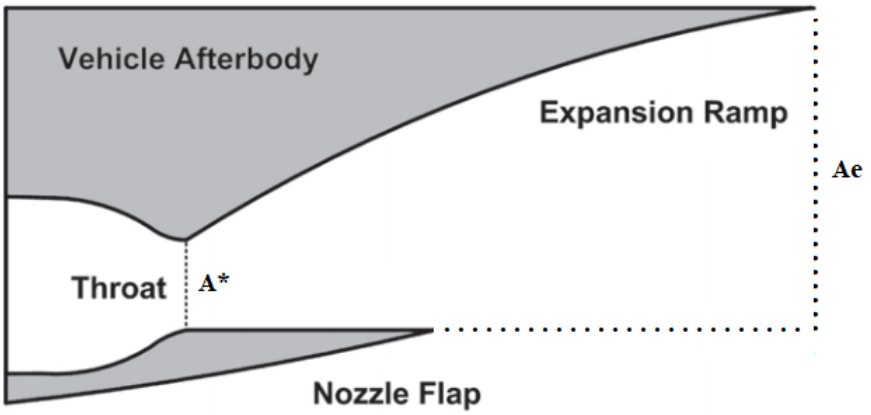

Figure 2.8: SERN schematic diagram [3]

Fig. 2.8 shows the basic geometry of a SERN integrated into a vehicle's afterbody. The upper-side is composed by a contoured expansion ramp downstream of the throat's sharp corner, which enable the flow to expand and accelerate, while the lower side is composed by a straight shorter flap. The physical mechanism that allow such a design to work will be explained in detail in a following chapter.

The SERN is an essential component for air-breathing hypersonic vehicles to achieve maximum thrust and efficiency, due to its qualities of minimizing weight and frictional drag while

producing substantial thrust from high-pressure flow [17].

It's successful operation was demonstrated in 2004 by the NASA X-43, an experimental unmanned hypersonic aircraft, part of the X-plane series and specifically of NASA's Hyper-X program. It set several airspeed records for jet aircraft, being the fastest air-breathing aircraft on record at approximately Mach 9.6 [37].

Advanced nozzles utilized at high speeds, such as the SERN, can be easily integrated and blended into the airframe which can reduce weight at large expansion ratios, reduce drag and improve overall reliability. On the downside, controllability can be affected by thrust vectoring [38]. The SERN also shows great self-adaptability at off-design conditions by managing the changing static pressure over a range of Mach numbers. This adaptability reduces the need to vary the exit area over different operating conditions [17].

The SERN's internal thrust is virtually unaffected by external flow if the pressure ratio remains high but at low-pressure ratios, the nozzle flow field is strongly influenced by external flow [39].

The expansion ramp is one with the aircraft fuselage, producing complex problems such as limited thrust vectoring controlled by throttling. This requires more control of elevators and complex control systems. In addition, flow leakage and cooling are issues. However, integrating the SERN into the airframe greatly reduces the drag and weight of the propulsion system [40], thus being advantageous overall.

SERNs are more efficient than conical nozzles and produce less drag compared to axisymmetric contoured nozzles, as the bottom surface is replaced by a short flap. Nevertheless, divergence losses need to be considered within the SERN design. Larger angles of divergence will increase the flow speed due to the production of expansion fans but the streamlines at the nozzle exit will be at different angles relative to the flight path [28].

Taking all this into consideration, the SERN's characteristics make it the preferred nozzle type for hypersonic air-breathing propulsion purposes, and will be the one selected for the research conducted in this thesis.

2.3.3 Flow Separation and Shock-Wave Patterns

When the aircraft flies at low Mach numbers and the nozzle works under severe over-expanded conditions, flow separation and shock wave boundary layer interactions within the nozzle can occur.

Flow separation is undesirable because it can lead to unsteady forces, threatening the integrity of the nozzle, as well as reducing performance. There are various separation patterns that can occur, and specific patterns occur in a definite range of NPR. Moreover, the separation patterns have their own special forms and make different influences on the perfor-

mance of the nozzle. For example, during the startup or shutdown process, the operating NPR changes continuously, so different separation patterns might occur in sequence, but the performance changes suddenly and intensively during the separation pattern transition processes, which can reduce the life time and the stability of the nozzle [3]. In combined cycle engines, the SERN is always designed at a high Mach number, however, at low flight Mach number the SERN's performance is greatly influenced by flow separation and the location of the separation point.

Shock-wave boundary layer interactions usually accompany flow separation, which may take on various patterns because the shock waves and the beginning of the separation are different [41]. Shock-wave interactions include several complex gas dynamics phenomena, such as incident shocks, Mach reflections, reflected shocks, triple points and shear layers [42].

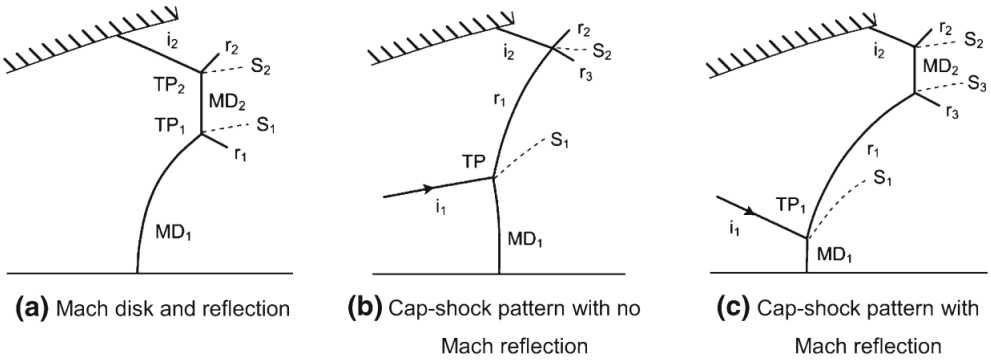

Figure 2.9: Shock interactions in overexpanded supersonic nozzles: incident shock (i), reflected shock (r), Mach disk (MD), triple point (TP), slip-line (S) [8]

Fig. 2.9 shows some shock reflections that might occur within a supersonic nozzle. When a internal shock impinges with the central Mach disk a cap shock pattern is formed. The reflected shock and the incident shock may form either a regular reflection or a Mach Reflection. When a normal shock wave, or Mach disk (MD) form, two typical "λ" shock structures (triple points) form as a result of the interaction of two separation shock waves.

A Particle Image Velocimetry (PIV) experiment was conducted by Xu et al. [43] to observe the flow fields of the over-expanded SERN, and validated a numerical simulation method in his study, which used the $k-\varepsilon$ turbulence model. The PIV results showed clearly the structure of the shock waves and the separation bubble.

In another SERN off-design study [44], two kinds of separation patterns were observed. The first mechanism was free shock separation (FSS). This occurred in over-expanded nozzles when the compression required to bring the boundary layer flow at the trailing edge of the nozzle up to ambient conditions induces boundary layer separation. The second mechanism was shock-induced separation (SIS). This occurred when a shock impinges on the SERN ramp surface and resulted in a pressure increase sufficient to separate the flow [44].

The restricted shock separation (RSS) has also been observed, in which the flow reattached

to the wall downstream the separation point and formed a closed re-circulation bubble. For a long time, it was considered that RSS only occurred in sub-scale experiment with cold air, but it was proven later that RSS could also appear in full-scale nozzles and hot conditions [45].

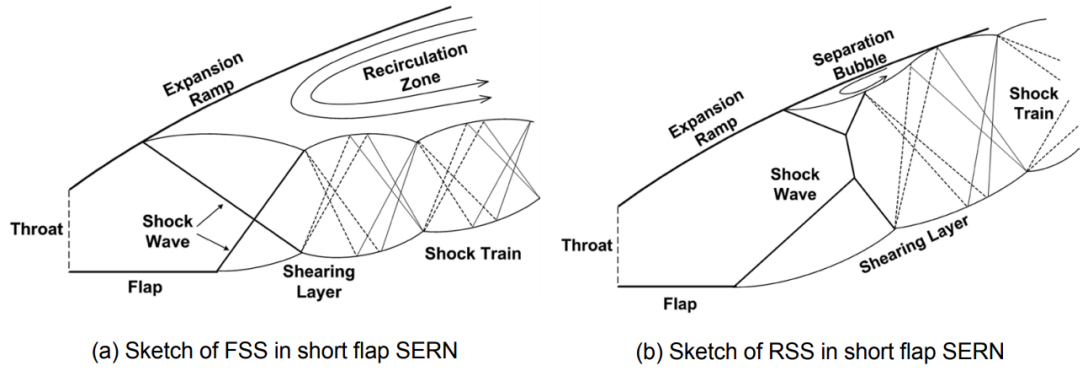

Figure 2.10: Sketch of separation patterns in short flap SERN [3]

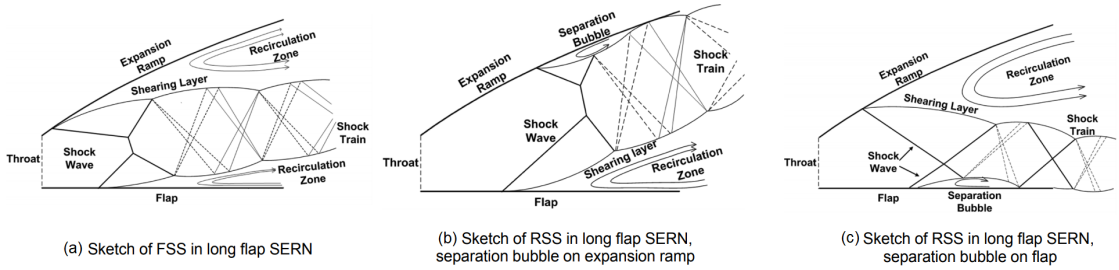

Figure 2.11: Sketch of separation patterns in long flap SERN [3]

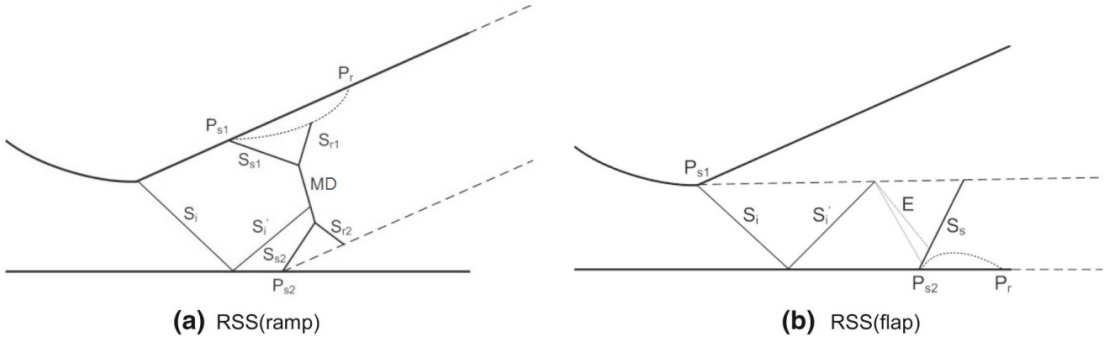

Figure 2.12: Sketch of shock-wave patterns in the SERN: internal shock (S_i), separation shock (S_s), reflected shock (S_r), separation point (P_s), reattachment point (P_r), Mach disk (MD), expansion fan (E) [8]

Figs. 2.10, 2.11 and 2.12 summarise the main flow separation and shock-wave patterns present in over-expanded SERN. According to research, RSS is the most common separation pattern, while the FSS is not very stable and is restricted to a narrow NPR range.

Moreover, experimental studies of off-design SERN separation patterns at various NPR have been conducted by Yu et al. [46, 3, 47], which also validated numerical simulations methods using FLUENT software and the RNG $k-\varepsilon$ turbulence model.

2.3.4 Contour Optimisation Method

As mentioned previously, in order to accelerate a flow through a nozzle at high speeds, the NAR must increase. Based on the quasi-one-dimensional flow theory, local Mach number relations as a function of local NAR can be developed, however, they cannot give information about the proper contour of the nozzle, and shock-waves may occur within the nozzle even at design conditions.

According to literature, the most widely used technique to trace the optimum shock-free contour for the nozzle walls is the method of characteristics. This classic and elegant numerical approach was applied to steady supersonic flow as early as the 1920s, but because of its intensive computational load at the time, only started to become widely used in the 1950s, and is still to this day the preferred method for designing supersonic nozzle contours [4].

Thus, the method of characteristics will be the method of choice employed to design the nozzles required for this study, and will be explained in detail in a following chapter.

Chapter 3

Theoretical Background

3.1 Overview

In order to proceed further, it is necessary to present and briefly go over some fundamental theoretical notions and foundations, on which the remainder of this study is build upon.

This chapter will include a review of basic thermodynamics such as and the specific heat ratio and isentropic processes.

Then, the compressible flow section will cover various important concepts such as the Mach number, isentropic flow relations, oblique shocks and Prandtl-Meyer expansion waves, quasi-one-dimensional flow, as well as over and underexpanded flow regimes, among other important theoretical notions regarding nozzle flow physics.

3.2 Thermodynamics

Thermodynamics is a branch of physics that deals with the energy and work of a system, and it has a significant role in the understanding of high speed compressible flow [48].

In most cases throughout this study, pressures and temperatures are moderate enough that the gas can be considered to be calorically perfect, which means the specific heats c_v and c_p are constant.

3.2.1 Specific Heat Ratio

The specific heat ratio, or adiabatic index, γ, is the ratio of the specific heat capacity at constant pressure, c_p, to specific heat capacity at constant volume, c_V.

$$\gamma = \frac{c_p}{c_v} \quad (3.1)$$

For standard air conditions, $\gamma = 1.4$.

It has an important role for its applications in thermodynamical reversible processes, involving ideal gases [49].

3.2.2 Isentropic Processes

An adiabatic process occurs when no heat is added or taken from the system ($\delta q = 0$). A reversible process is one in which no dissipative phenomena (viscosity effects, thermal conductivity, etc.) occur ($ds_{irrev} = 0$).

A process which is both adiabatic and reversible is called isentropic.

In an isentropic process the entropy is constant, $ds = 0$.

Eq. 3.2 relates pressure, density and temperature for an isentropic process, and is a very important tool in the analysis of compressible flows.

$$\frac{p_2}{p_1} = \left(\frac{\rho_2}{\rho_1}\right)^{\gamma} = \left(\frac{T_2}{T_1}\right)^{\gamma/(\gamma-1)} \quad (3.2)$$

The flow inside a nozzle, with the exception of the thin boundary layer formed at the walls, can be considered isentropic [4].

3.3 Compressible Flow

A compressible flow is characterised by having significant changes in fluid density.

In reality, all flows are compressible. However, at low speeds the flows are usually treated as incompressible, because the compressibility effects are negligible [50].

The ratio of the speed of an object moving through air, V, and the speed of sound, a, determines the magnitude of many of the compressibility effects. This speed ratio is very important and it has become a special parameter present in all high speed flow called the Mach number, M.

$$a = \sqrt{\gamma RT} \quad (3.3)$$

$$M = \frac{V}{a} \quad (3.4)$$

The Mach number is a very important ratio in high speed compressible flow physics, and

allows one to distinguish between some flow regimes in which compressibility effects vary:

- Subsonic flow: $M < 1$. For the lowest subsonic conditions ($M < 0.3$) compressibility can be ignored. For higher subsonic speeds ($M > 0.8$) the compressibility effects become noticeable and it can be refered to as transonic;

- Sonic flow: $M = 1$. Flow travels at the same speed of the sound waves it creates, leading to a formation of a shockwave;

- Supersonic flow: $M > 1$. Flow moving faster than the sound waves created by it, governed by compressible flow dynamics, such as shockwaves and isentropic processes;

- Hypersonic flow: $M > 5$. At such speeds, the energy of the flow is such that it begins to influence the chemical bonds of the molecules of air, and thus its chemistry must be considered.

For supersonic and hypersonic flows, disturbances are transmited downstream, and there is no upstream influence [51].

3.3.1 Isentropic Flow Relations

Consider a fluid element in a flow travelling at a certain Mach number M, velocity V, with a static pressure, temperature and density p, T and ρ.

If the fluid element was isentropically slowed down to zero velocity, the pressure, temperature and density which the element achieves is defined as total pressure p_0, total temperature T_0 and total density ρ_0.

If the general flowfield is isentropic throughout, then T_0, p_0 and ρ_0 are constant values at every point in the flow.

The equations below (plotted in Fig. 3.1) allow one to calculate the ratios of total to static properties of a point in a flow as a function of M and γ [4].

$$\frac{T_0}{T} = 1 + \frac{\gamma - 1}{2} M^2 \quad (3.5)$$

$$\frac{p_0}{p} = \left(1 + \frac{\gamma - 1}{2} M^2\right)^{\gamma/(\gamma-1)} \quad (3.6)$$

$$\frac{\rho_0}{\rho} = \left(1 + \frac{\gamma - 1}{2} M^2\right)^{1/(\gamma-1)} \quad (3.7)$$

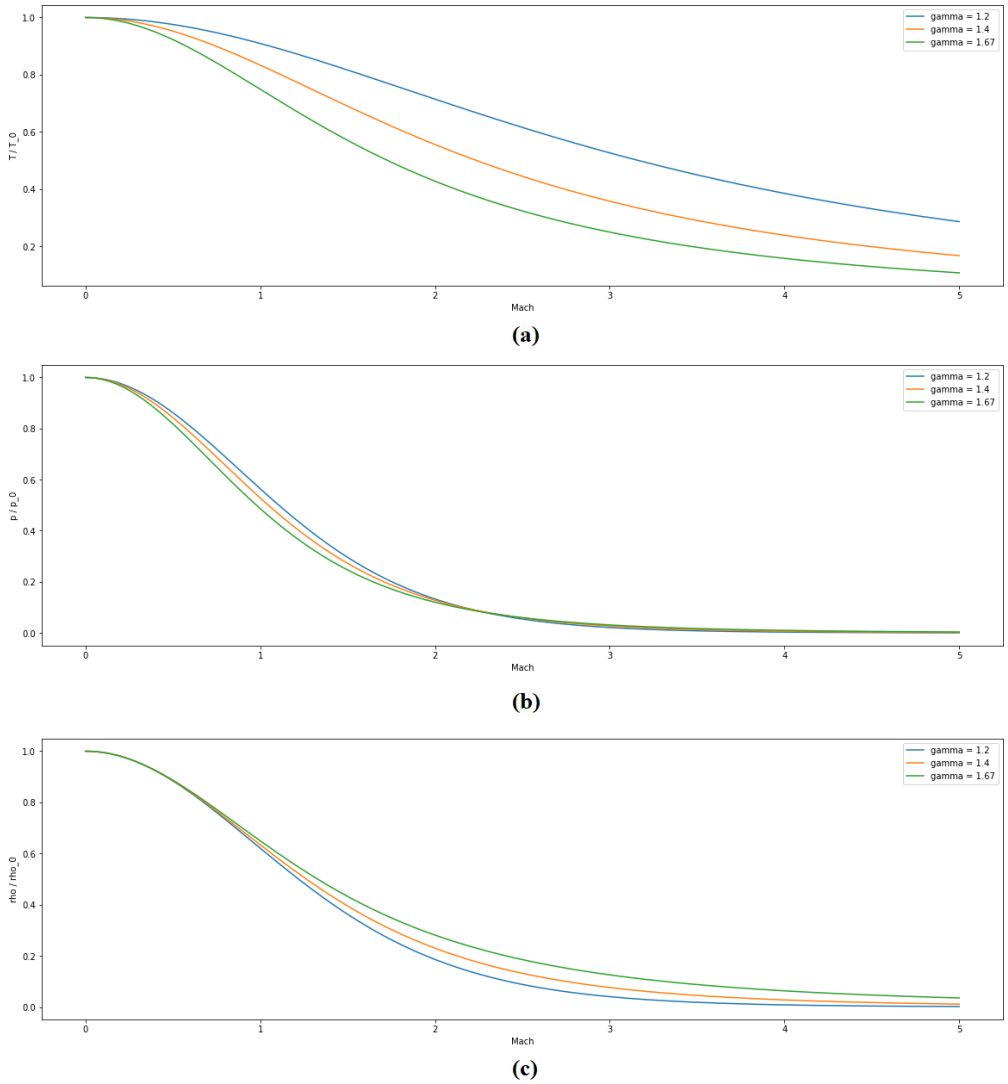

Figure 3.1: Temperature (a), pressure (b) and density (c) static to total ratio, as a function of Mach, for various γ

From a quick look at the plots in Fig. 3.1, it is possible to conclude that for all property ratios, since the total values remain constant, the static values must decrease as the Mach number increases.

If instead of being slowed to zero, the fluid element was brought to Mach 1, the ratios of total to static properties at sonic condition (*) are:

$$\frac{T^*}{T_0} = \left(\frac{2}{\gamma + 1}\right) \quad (3.8)$$

$$\frac{p^*}{p_0} = \left(\frac{2}{\gamma+1}\right)^{\gamma/(\gamma-1)} \quad (3.9)$$

$$\frac{\rho^*}{\rho_0} = \left(\frac{2}{\gamma+1}\right)^{1/(\gamma-1)} \quad (3.10)$$

For $\gamma = 1.4$, the value of these ratios is $T^*/T_0 = 0.833$, $p^*/p_0 = 0.528$ and $\rho^*/\rho_0 = 0.634$

3.3.2 Oblique Shock and Prandtl-Meyer Expansion Waves

When a supersonic flow is turned into or away from itself, shock waves and expansion waves can occur, respectively. In both cases, if the wave is infinitely weak it becomes a Mach wave, with an angle (Mach angle), μ, with respect to the flow direction:

$$\mu = \sin^{-1}\frac{1}{M} \quad (3.11)$$

Oblique shock waves generally occur when supersonic flow is turned into itself, as shown in Fig. 3.2 (a).

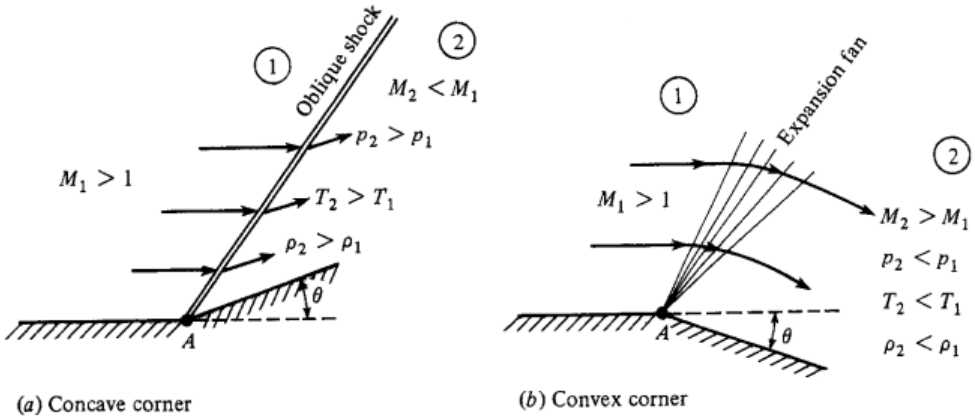

Figure 3.2: Supersonic flow behaviour over corners [4]

As the surface bounding the supersonic flow deflects upwards an angle θ, consequently the flow streamlines will also deflect upward in order to keep the flow parallel to the surface. This change in flow direction occurs across a shock wave oblique to the stream direction.

Through this type of shock, the Mach number decreases, and the pressure, temperature and density of the flow increase.

Unlike an oblique shock wave, an expansion wave (also denominated Prandtl-Meyer expansion wave) occurs when supersonic flow is turned away from itself.

Through an expansion wave the streamlines are smooth curves, and there is an increase in flow Mach number, as well as a decrease in flow pressure, density and temperature. A continuous expansion region composed of an infinite number of Mach waves is called expansion fan. Since for each Mach wave $ds = 0$, the expansion is isentropic.

The Prandtl-Meyer function allows the determination of flow properties downstream of the expansion ($M_2,\ p_2,\ T_2$) given the upstream values $M_1,\ p_1,\ T_1$ and θ_2.

The analysis begins by considering the infinitesimal changes across the weak Mach waves produced by an infinitesimal flow deflection $d\theta$.

The governing differential equation for Prandtl-Meyer flow is given by Eq. 3.12:

$$d\theta = \sqrt{M^2 - 1}\frac{dV}{V} \quad (3.12)$$

When integrated across the wave, Eq. 3.12 becomes:

$$\theta_2 = \nu(M_2) - \nu(M_1) \quad (3.13)$$

where θ_1 is assumed to be zero and the Prandtl-Meyer function ν is given by:

$$\nu(M) = \sqrt{\frac{\gamma+1}{\gamma-1}}\tan^{-1}\sqrt{\frac{\gamma-1}{\gamma+1}(M^2-1)} - \tan^{-1}\sqrt{M^2-1} \quad (3.14)$$

Thus, knowing the Mach number M and specific heat ratio γ upstream and downstream of the expansion fan allows to determine the flow turning angle θ_2.

Since the flow through the Prandtl-Meyer expansion is isentropic, all the flow properties are given by the isentropic flow relations 3.15 and 3.16, from the local Mach numbers obtained previously:

$$\frac{T_1}{T_2} = \frac{1 + \frac{\gamma-1}{2}M_2^2}{1 + \frac{\gamma-1}{2}M_1^2} \quad (3.15)$$

$$\frac{p_1}{p_2} = \left(\frac{1 + \frac{\gamma-1}{2} M_2^2}{1 + \frac{\gamma-1}{2} M_1^2} \right)^{\gamma/(\gamma-1)} \quad (3.16)$$

3.3.3 Quasi-One-Dimensional Flow

The area-velocity relation, Eq. 3.17, is very important in the study and analysis of flows bounded inside a duct, and is closely related with quasi-one-dimensional flow.

In this type of flow, properties are uniform across a given cross section and are a function of x distance along the direction of the flow ($A = A(x)$, $p = p(x)$, $\rho = \rho(x)$ and $u = u(x)$), varying due to an area change.

$$\frac{dA}{A} = (M^2 - 1)\frac{du}{u} \quad (3.17)$$

From the area-velocity relation, one can conclude that for a different Mach numbers the following phenomena occur:

1. $M \to 0$, shows that $Au = const$, and in the limit corresponds to incompressible flow.

2. $0 \leq M < 1$ (subsonic flow), a velocity increase ($du > 0$) is associated with an area decrease ($dA < 0$), thus, for a subsonic flow the velocity increase in a converging duct and decrease in a diverging duct.

3. $M > 1$ (supersonic flow), a velocity increase ($du > 0$) is associated with an area increase ($dA > 0$), thus, for a supersonic flow the velocity decrease in a converging duct and increase in a diverging duct. This is one of the main differences to subsonic flow.

4. $M = 1$ (sonic flow), yields $dA/A = 0$, which physically corresponds to the minimum local area, also called a throat.

This explains why supersonic nozzles have a diverging duct shape, in order to expand and accelerate the exhaust gases to high speeds.

Another important relation from quasi-one-dimensional isentropic flow is the area-Mach relation:

$$\left(\frac{A}{A^*}\right)^2 = \frac{1}{M^2}\left(\frac{2}{\gamma+1}\left(1+\frac{\gamma-1}{2}M^2\right)\right)^{(\gamma+1)/(\gamma-1)} \quad (3.18)$$

From this relation one can conclude that the Mach number at any location in the duct is a function of the local area ratio to the sonic throat area.

This ratio is also called Nozzle Area Ratio (NAR):

$$NAR = \frac{A}{A^*} \quad (3.19)$$

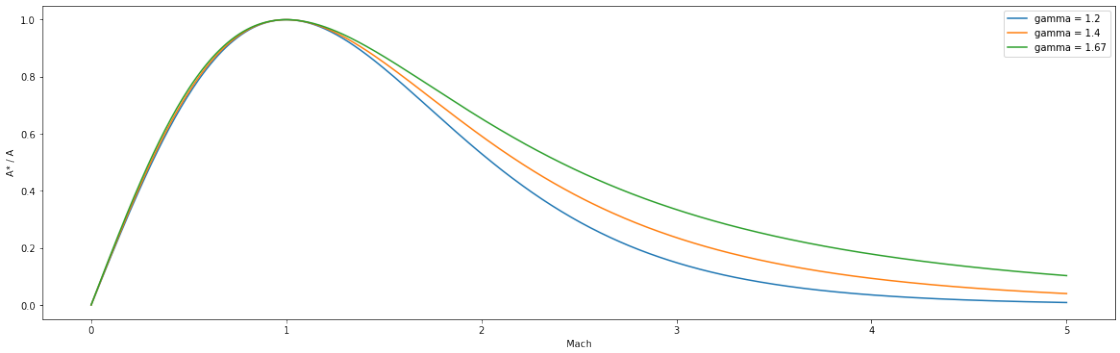

Figure 3.3: A^*/A (NAR^{-1}) as a function of Mach, for various γ

Fig. 3.3 shows the variation of the NAR inverse with respect to Mach number. As described previously, in subsonic flow a speed increase corresponds to an area decrease, until sonic conditions are achieved ($M = 1$ and $A^*/A = 1$). Then, as the Mach number increases, also does the area A with respect to the throat area A^*.

The effects of the γ variation also only become apparent for $M > 1$, and show that a flow with a lower γ requires a greater area A in order to achieve the same M, and vice-versa.

It is important to note that these quasi-one-dimensional considerations allow the analysis of cross-section averaged properties inside a nozzle of a given shape, however, they don't provide enough information on how to properly design a supersonic shockfree nozzle contour. The method to determine this proper contour will be described in detail in the following chapter.

3.3.4 Under-expanded and Over-expanded Nozzle Flow

The effect of the ambient pressure at which a nozzle operates (also called back-pressure), p_∞, is very important for a nozzle performance.

Firstly, in order to accelerate the flow through a nozzle, there must exist a pressure differential between the nozzle exit, p_e and the nozzle inlet, p_0: $p_e/p_0 < 1$.

However, depending on the difference between the nozzle exit pressure and the ambient pressure, the following types of flow downstream of the nozzle exit can occur (Fig. 3.4):

1. Perfectly expanded flow ($p_e = p_\infty$)
2. Over-expanded flow ($p_e < p_\infty$)
3. Under-expanded flow ($p_e > p_\infty$)

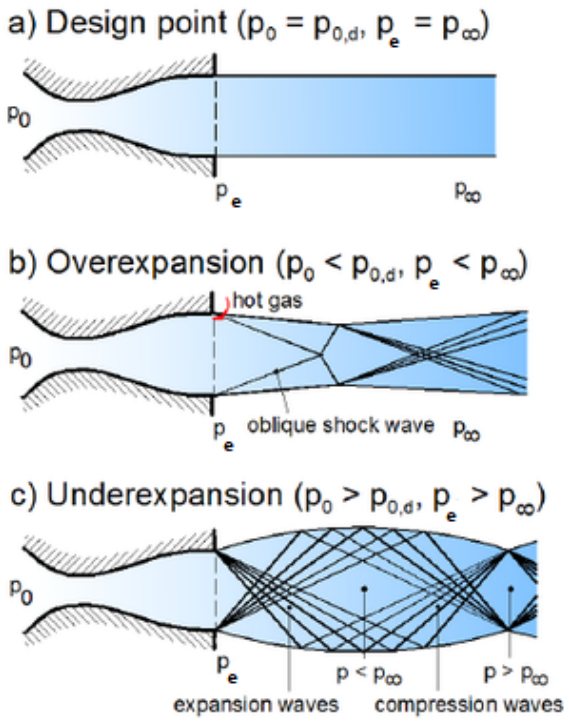

Figure 3.4: Schematic of flow regimes downstream of nozzle exit [9]

For a nozzle to operate in ideal conditions, achieving completely shock free isentropic expansion, the pressure at the exit of the nozzle must be equal to that of the surrounding ambient. This could be considered the design point of the nozzle, where efficiency is maximised (Fig. 3.4 (a)).

However, propulsive systems operating off-design at high Mach numbers feature complex aerodynamic phenomena, such as the creation of shock diamonds (Mach diamonds / disks), which are repeated shock patterns downstream of the nozzle exit (Fig. 3.4 (b), (c) and Fig. 3.5). Under these conditions the nozzle loses efficiency in generating thrust. The formation patterns result between the interaction and friction of the exhausted jet air and the free stream, resulting in a turbulent shear layer which causes a viscous damping effect, gradually dissipating the shock wave structure further downstream of the nozzle exit [21].

Therefore, in cases when the ambient pressure is not equal to the pressure at the nozzle exit, the gas stream tries to adjust itself in an attempt to match both pressures.

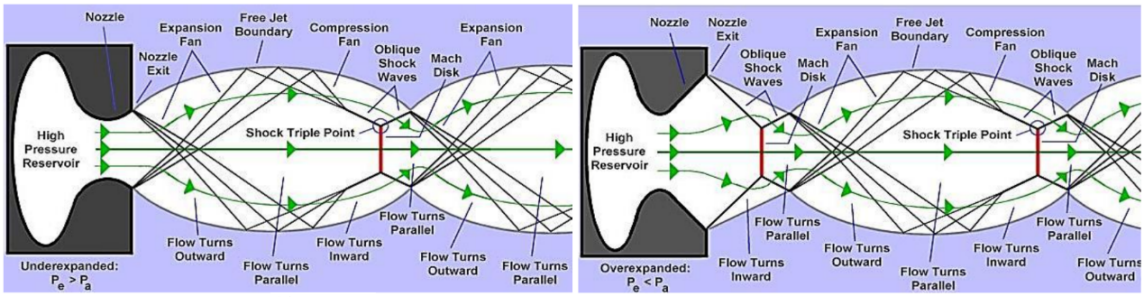

Figure 3.5: Shock diamond patterns in under-expanded (a) and over-expanded (b) flows [10]

When the ambient pressure is significantly lower than the exit pressure, the expansion continues after the nozzle exit and deviates from the nozzle axis through a Prandtl-Meyer expansion wave, as shown in Fig. 3.5 (a). This leads to a vacuum forming at the jet axis, which sucks back the momentum of the gases towards it, creating re-compression as the expansion waves are reflected from the constant pressure jet boundary as compression waves. The expansion is produced by waves, at the opposite jet boundary which, along with the radial expansion, cause a series of small returning shocks which coalesce near the axis to form diamond patterns [21]. The gases therefore return to the conditions at the nozzle exit and the process is repeated, resulting in a phenomenon known as under-expansion. Since the flow is supersonic, the expansion followed by the compression of the exhaust jet beyond the nozzle is achieved by Mach and shock waves [10].

On the other hand, if the outside pressure is higher than that of the nozzle exit, an oblique shock is generated, which raises its pressure and is compressed inwards. However, the compressed flow pressure may exceed the atmospheric pressure, in which case the flow expands back outward to reduce the pressure again. This process may be repeated several times until the exhaust pressure is matched with the ambient pressure. In other words, the flow will repeatedly compress and expand while gradually dissipating towards the equalisation of the pressure difference between the atmosphere and the exhaust. A shock diamond pattern is created, which is in this case known as over-expansion (Fig. 3.5 (b)) [21].

The ratio between the pressure at the nozzle inlet and the ambient pressure at which the nozzle operates is called Nozzle Pressure Ratio (NPR):

$$NPR = \frac{p_0}{p_\infty} \quad (3.20)$$

The NPR will be an important parameter in further chapters of this study.

After this brief theoretical review of fundamental concepts, one can conclude complex phenomena can appear when dealing with super and hypersonic nozzles, thus a more detailed analysis of the flow through a nozzle requires more advanced numerical techniques, described in the following section.

3.4 Method of Characteristics

3.4.1 Overview

The contents presented in this section were retrived from the book Modern Compressible Flow With Historical Perspective, from John D. Anderson [4].

When it comes to fluid flow, analytical solutions of the equations governing it is only possible for simple problems.

Since there is no general analytical solution for non linear partial differential equations (PDE), numerical techniques have been adopted to overcome this issue.

The method of characteristics (MOC) is a classical numerical technique for solving PDEs. Typically, it applies to first-order equations, although more generally it is valid for any hyperbolic PDE. The method is to reduce a PDE to a family of ordinary differential equations (ODE) along which the solution can be integrated from some initial data given.

The MOC technique is widely used in supersonic and hypersonic nozzle design, generating a contour for shock-free, parallel flow at the exhaust. In order to apply the MOC, flow is assumed irrotational, inviscid and isentropic throughout the nozzle.

It is based on a discretization process along a set of characteristic lines, so the accuracy of the method is proportional to the number of characteristics used to solve the problem.

Consider a two-dimensional irrotational flow, where velocity V and its components u and v are known at each point along a vertical line, $x = x_0$, as shown in Fig. 3.6

From geometry we can define the the angle μ as $\sin \mu = u/V = a/V = 1/M$. μ is the *Mach angle*.

A line with a particular angle in relation to the streamline direction exists, along which the derivatives of the flowfield properties (velocity u and v, pressure p, temperature T and density ρ) are indeterminate. Such lines are called characteristic lines and they make an angle μ with respect to the vector V. Characteristics lines are also Mach lines, which means the velocity component perpendicular to the y direction is a sonic line.

With this in mind, the flowfield can be solved in three steps:

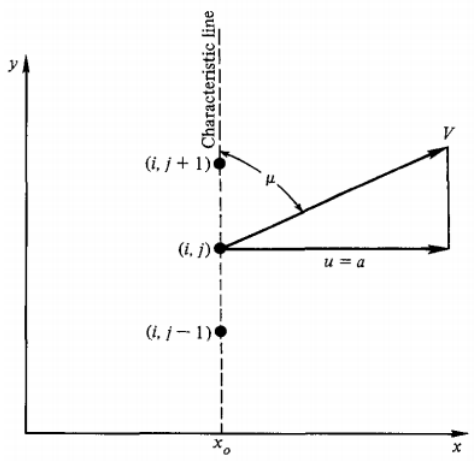

Figure 3.6: Characteristic direction illustration [4]

1. Find the lines where flow variables are continuous, but the derivatives are indeterminate. As defined previously, such lines are called characteristic lines.

2. Combine the PDEs in order to obtain ODEs that hold along the characteristic lines. Such ODEs are called compatibility equations.

3. Solve the compatibility equations step by step along the characteristic lines, starting from initial given conditions at some region in the flow. Thus the complete flowfield can be determined along the characteristic lines, referred also as characteristics net.

3.4.2 Determination of Characteristic Lines

For two-dimensional, steady, adiabatic, irrotational supersonic flow, the governing nonlinear equations are:

$$(1 - \frac{\Phi_x^2}{a^2})\Phi_{xx} + (1 - \frac{\Phi_y^2}{a^2})\Phi_{yy} - \frac{2\Phi_x\Phi_y}{a^2}\Phi_{xy} = 0 \quad (3.21)$$

where Φ is the full velocity potential: $\Phi_x = u \quad \Phi_y = v \quad V = ui + vj$

$\Phi_x = f(x, y)$, hence:

$$d\Phi_x = \frac{\partial \Phi_x}{\partial x}dx + \frac{\partial \Phi_y}{\partial y}dy = \Phi_{xx}dx + \Phi_{yy}dy \quad (3.22)$$

$$d\Phi_y = \frac{\partial \Phi_y}{\partial x}dx + \frac{\partial \Phi_y}{\partial y}dy = \Phi_{xy}dx + \Phi_{yy}dy \quad (3.23)$$

Combining these equations:

$$(1 - \frac{u^2}{a^2})\Phi_{xx} + (1 - \frac{v^2}{a^2})\Phi_{yy} - \frac{2uv}{a^2}\Phi_{xy} = 0 \quad (3.24)$$

$$(dx)\Phi_{xx} + (dy)\Phi_{xy} = du \quad (3.25)$$

$$(dx)\Phi_{xy} + (dy)\Phi_{yy} = dv \quad (3.26)$$

Using Cramer's rule, the solution for Φ_{xy} is:

$$\Phi_{xy} = \frac{\begin{vmatrix} 1 - \frac{u^2}{a^2} & 0 & 1 - \frac{v^2}{a^2} \\ dx & du & 0 \\ 0 & dv & dy \end{vmatrix}}{\begin{vmatrix} 1 - \frac{u^2}{a^2} & \frac{-2uv}{a^2} & 1 - \frac{v^2}{a^2} \\ dx & dy & 0 \\ 0 & dx & dy \end{vmatrix}} = \frac{N}{D} \quad (3.27)$$

However, if dx and dy are such that $D = 0$, Φ_{xy} becomes physically inconsistent. In order to make Φ_{xy} finite, $N = 0$. Thus, Φ_{xy} cannot be defined in this particular direction where $D = 0$.

Therefore, the lines along which the derivatives of flow variables are indeterminate are called characteristic lines.

Setting $D = 0$ and using the quadratic formula to simplify, yields:

$$(\frac{dy}{dx})_{char} = \frac{-uv/a^2 \pm \sqrt{((u^2+v^2)/a^2) - 1}}{1 - (u^2/a^2)} \quad (3.28)$$

Eq. 3.28 defines the characteristic curves in the physical space xy. The term inside the square root is:

$$\frac{u^2+v^2}{a^2} - 1 = \frac{V^2}{a^2} - 1 = M^2 - 1 \quad (3.29)$$

Hence, we can state:

1. If $M < 1$, the characteristics are imaginary, and Eq. 3.28 is an elliptic partial differential equation.

2. If $M = 1$, the is one real characteristic through each point of the flow and Eq. 3.28 is a parabolic partial differential equation.

3. If $M > 1$, there are two real characteristics through each point of the flowfield and Eq. 3.28 is a hyperbolic partial differential equation.

Thus, because two real characteristics exist through each point in a $M > 1$ flow, the MOC is a very useful technique for solving supersonic flows.

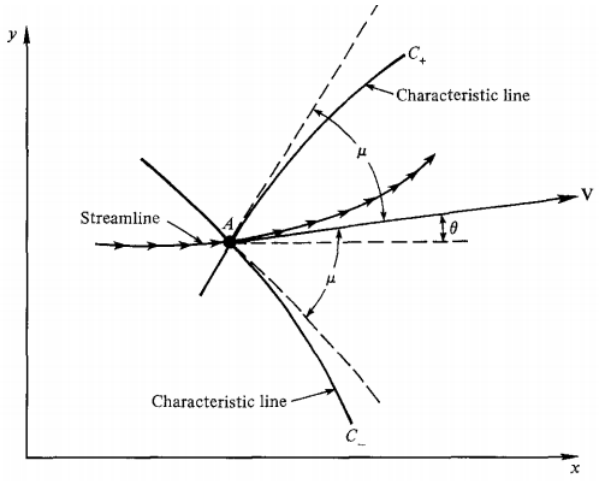

Figure 3.7: Left- and right-running characteristic lines illustration [4]

After some algebraic and trigonometric manipulation, Eq. 3.28 can be reduced to:

$$(\frac{dy}{dx})_{char} = \tan(\theta \pm \mu) \quad (3.30)$$

Fig. 3.7 provides a graphical interpretation of Eq. 3.30. At point A, the streamline makes an angle θ with the x axis. Two characteristics pass through point A: The characteristic given by the angle $\theta + \mu$ is called a C_+ characteristic (left-running characteristic). The characteristic given by the angle $\theta - \mu$ is called C_- characteristic (right-running characteristic). Characteristic lines are generally curved, hence θ and μ change between points within the flow.

3.4.3 Determination of Compatibility Equations

In order to derive the compatibility equations, one must set $N = 0$ in Eq. 3.27, which yields:

$$(1 - \frac{u^2}{a^2})dudy + (1 - \frac{v^2}{a^2})dxdv = 0 \quad (3.31)$$

$$\frac{dv}{du} = \frac{(1 - \frac{u^2}{a^2})dy}{(1 - \frac{v^2}{a^2})dx} \quad (3.32)$$

The term $\frac{dy}{dx}$ in Eq. 3.32 is valid along the characteristic line. Thus, $\frac{dy}{dx} = (\frac{dy}{dx})_{char}$

Substituting Eq. 3.28 into Eq. 3.32 simplifies to:

$$\frac{dv}{du} = \frac{\frac{uv}{a^2} \pm \sqrt{\frac{u^2+v^2}{a^2} - 1}}{a - \frac{v^2}{a^2}} \quad (3.33)$$

Since $u = V\cos\theta$ and $v = V\sin\theta$, Eq. 3.33 reduces to:

$$d\theta = \pm\sqrt{M^2 - 1}\frac{dV}{V} \quad (3.34)$$

Eq. 3.34 is the compatibility equation that describes the variation of flow properties along characteristic lines:

Eq. 3.34 can be integrated to give the Prandtl-Meyer function $\nu(M)$. Therefore, Eq. 3.34 is replaced by the algebraic compatibility equations:

$$\theta + \nu(M) = constant = K_- \quad (along\ the\ C_-\ characteristic) \quad (3.35)$$

$$\theta - \nu(M) = constant = K_+ \quad (along\ the\ C_+\ characteristic) \quad (3.36)$$

Compatibility equations 3.35 and 3.36 relate velocity magnitude and direction along the characteristic lines, and are very useful for MOC graphical solutions and are sufficient for direct numerical calculations.

3.4.4 Unit Processes

In order to apply the MOC, a series of specific computations called unit processes solve the compatibility equations point by point along the characteristics. These may vary depending on whether the points are internal to the flowfield, on a solid or free boundary, or on a shock wave.

If we know the flowfield conditions at two points in the flow, we can find the conditions at a third point, as shown in Fig. 3.8

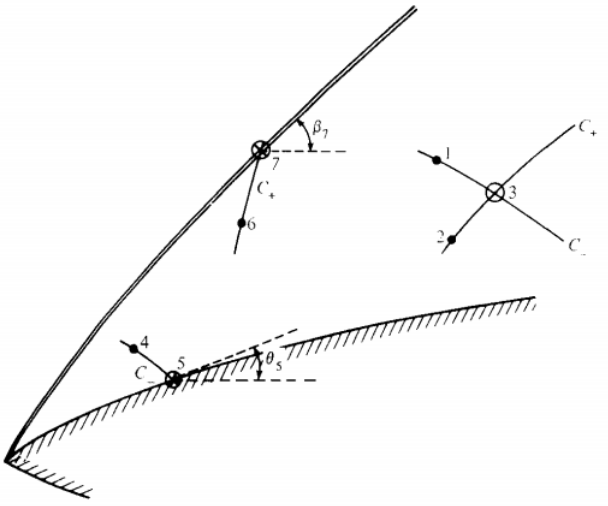

Figure 3.8: Unit processes [4]

The values ν_1, θ_1, ν_2 and θ_2 are known at points 1 and 2 respectively. Point 3 is located by the intersection of C_- characteristic through point 1 and the C_+ characteristic through point 2.

From Eq. 3.35 and 3.36:

$$\theta_1 + \nu_1 = (K_-)_1 \quad (3.37)$$

$$\theta_2 - \nu_2 = (K_+)_2 \quad (3.38)$$

$$\theta_3 + \nu_3 = (K_-)_3 = (K_-)_1 \quad (3.39)$$

$$\theta_3 - \nu_3 = (K_+)_3 = (K_+)_2 \quad (3.40)$$

Solving Eq. 3.39 and 3.40:

$$\theta_3 = \frac{1}{2}((K_-)_1 + (K_+)_2) \quad (3.41)$$

$$\nu_3 = \frac{1}{2}((K_-)_1 - (K_+)_2) \quad (3.42)$$

Thus, flow conditions at point 3 are determined from the information of the previous points. ν_3 determines M_3 through Eq. 3.14, and M_3 determines pressure, temperature and density through the isentropic flow relations, Eq. 3.6, 3.5 and 3.7. From temperature, the speed of sound and flow speed can be computed through Eq. 3.3 and 3.4.

To determine the exact location of point 3, an approximate procedure which involves the determination of the slopes of C_- and C_+ is used, assuming characteristic lines are straight-line segments between grid points.

Thus, the slope of C_- can be computed as:

$$\frac{1}{2}(\theta_1 + \theta_3) - \frac{1}{2}(\mu_1 + \mu_3) \quad (3.43)$$

and the slope of C_+:

$$\frac{1}{2}(\theta_2 + \theta_3) + \frac{1}{2}(\mu_2 + \mu_3) \quad (3.44)$$

Their intersection locates point 3, as shown in Fig. 3.9

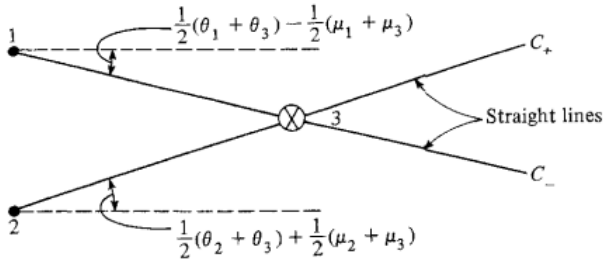

Figure 3.9: Approximation of characteristics by straight lines [4]

For a wall point, consider point 4 in Fig. 3.8, at which the flow is known. Hence, along C_- through point 4, the value K_- is known:

$$(K_-)_4 = \theta_4 + \nu_4 \quad (3.45)$$

and the C_- intersects the wall at point 5. Thus, at point 5:

$$(K_-)_4 = (K_-)_5 = \theta_5 + \nu_5 \quad (3.46)$$

Since the flow must be tangent at the wall, θ_5 is known. Thus:

$$\nu_5 = \nu_4 + \theta_4 - \theta_5 \quad (3.47)$$

Also, if the conditions at a point near a shock wave are known, we can find the flow variables immediately behind the shock.

Considering the C_+ through point 6, the value K_+ is known:

$$(K_+)_6 = \theta_6 - \nu_6 \quad (3.48)$$

The C_+ intersects the shock at point 7, hence:

$$(K_+)_6 = (K_+)_7 = \theta_7 - \nu_7 \quad (3.49)$$

These unit processes must start from an initial data line, on which the flowfield properties are known.

In the present study, the initial data line is assumed to be a slightly inclined straight line, from the sonic line in the nozzle throat.

3.5 Computational Fluid Dynamics

Computational fluid dynamics (CFD) uses numerical analysis and data structures to solve problems involving fluid flows, where computers are used to perform the calculations required to simulate the free-stream flow of the fluid and its interactions with surfaces defined by boundary conditions. Usually CFD software is validated by using experimental data for comparing results [52].

The contents presented in this section were retrived from the ANSYS FLUENT 12.0 Theory Guide [11].

3.5.1 Governing Equations

ANSYS FLUENT solves the mass and momentum conservation equations for all types of flow. In flows that involve compressibility and turbulence, additional energy conservation and transport equations are also solved.

3.5.1.1 Mass Conservation Equation

For single phase flows, the mass conservation equation states that mass cannot be created or destroyed. The contribution of a diffusive flow is also nonexistent, since in a resting fluid, any mass variation would imply movement of particles.

The general form of the mass conservation (continuity equation) valid for compressible and incompressible flows can be written as follows:

$$\frac{\partial \rho}{\partial t} + \nabla(\rho \vec{v}) = 0 \quad (3.50)$$

where ρ is the fluid density, t stands for time an $\vec{v}$ is the flow velocity vector.

3.5.1.2 Momentum Conservation Equations

Conservation of momentum in an inertial reference frame is described by:

$$\frac{\partial}{\partial t}(\rho\vec{v}) + \nabla(\rho\vec{v}\vec{v}) = -\nabla p + \nabla(\bar{\bar{\tau}}) + \rho\vec{g} + \vec{F} \quad (3.51)$$

where p is the static pressure, $\bar{\bar{\tau}}$ is the stress tensor, and $\rho\vec{g}$ and $\vec{F}$ are the gravitational body force and external body forces, respectively.

The stress tensor $\bar{\bar{\tau}}$ is given by:

$$\bar{\bar{\tau}} = \mu\left((\nabla\vec{v} + \nabla\vec{v}^T) - \frac{2}{3}\nabla\vec{v}I\right) \quad (3.52)$$

where μ is the molecular viscosity, I is the unit tensor, and the second term on the right hand side is the effect of volume dilation.

The well known Navier-Stokes equations that govern fluid flow can be established by writing the equations above in the three spatial dimensions.

3.5.1.3 Energy Conservation Equations

The energy conservation equation is based on the first law of thermodynamics, which states that a particle's total energy rate of change must be equal to the particle's received energy in the form of heat and work. Applied to a turbulent flow, the equation can be written as:

$$\frac{\partial}{\partial t}(\rho i) + \nabla(\rho i\vec{v}) = -p\nabla(\vec{v}) + \nabla(k\vec{\nabla}T) + \Phi_d \quad (3.53)$$

where i is the internal thermal energy, k is the thermal conductivity coefficient, T is the static absolute temperature and Φ_d is the viscous dissipation term.

3.5.1.4 Compressible Flow Modelling

Compressibility effects are encountered when the flow velocity approaches or exceeds the speed of sound of the gas or when the pressure change in the system ($\Delta p/p$) is large, which leads to a variation of the gas density with pressure and has a significant impact on the flow velocity, pressure, and temperature. Compressible flows create a unique set of flow physics

which must be taken into account, and ANSYS FLUENT provides a wide range of compressible flow modeling capabilities for subsonic, transonic, and supersonic flows.

Compressible flows are typically characterized by the total pressure p_0 and total temperature T_0 of the flow, which for constant C_p reduces to Eq. 3.5 and 3.6 of isentropic flow relations.

They are described by the standard continuity and momentum equations. The energy equation correctly incorporates the coupling between the flow velocity and the static temperature, and should be activated when solving a compressible flow.

There is no need to activate any special physical models, however the compressible form of the ideal gas law must be applied:

$$\rho = \frac{p_{op} + p}{\frac{R}{M_w}T} \quad (3.54)$$

where p_{op} is the operating pressure, p is the local static pressure relative to the operating pressure, R is the universal gas constant, and M_w is the molecular weight. The temperature, T, will be computed from the energy equation.

3.5.2 Turbulent Flow Modelling

Turbulent flows are characterized by fluctuating velocity fields. These fluctuations mix transported quantities such as momentum, energy, and species concentration, and cause the transported quantities to fluctuate as well. Since these fluctuations can be of small scale and high frequency, they are too computationally expensive to simulate directly in practical engineering calculations. Instead, the instantaneous governing equations can be time-averaged, ensemble-averaged, or otherwise manipulated to remove the resolution of small scales, resulting in a modified set of equations that are computationally less expensive to solve. However, the modified equations contain additional unknown variables, and turbulence models are needed to determine these variables in terms of known quantities.

No single turbulence model is universally accepted as being superior for all classes of problems. The choice of turbulence model will depend on considerations such as the physics encompassed in the flow, the established practice for a specific class of problem, the level of accuracy required, the available computational resources, and the amount of time available for the simulation.

3.5.2.1 Reynolds-Averaged Approach

The Reynolds-Averaged Navier-Stokes (RANS) equations govern the transport of the averaged flow quantities, with the whole range of the scales of turbulence being modelled. It

greatly reduces the required computational effort and resources, and is widely adopted for practical engineering applications.

In Reynolds averaging, the solution variables in the instantaneous (exact) Navier-Stokes equations are decomposed into the mean and fluctuating components. For the velocity components:

$$u_i = \bar{u}_i + u_i^{'} \quad (3.55)$$

where $\bar{u}_i$ and u_i' are the mean and fluctuating velocity components, respectively.

For pressure and other scalars quantities:

$$\Phi = \bar{\Phi} + \Phi^{'} \quad (3.56)$$

where Φ represents scalars such as pressure or energy.

Substituting expressions of this form for the flow variables into the instantaneous continuity and momentum equations, yields the ensemble-averaged momentum equations, which can be written in Cartesian tensor form as:

$$\frac{\partial \rho}{\partial t} + \frac{\partial}{\partial x_i}(\rho u_i) = 0 \quad (3.57)$$

$$\frac{\partial}{\partial t}(\rho u_i) + \frac{\partial}{\partial x_j}(\rho u_i u_j) = -\frac{\partial p}{\partial x_i} + \frac{\partial}{\partial x_j}\left(\mu\left(\frac{\partial u_i}{\partial x_j} + \frac{\partial u_j}{\partial x_i} - \frac{2}{3}\delta_{ij}\frac{\partial u_k}{\partial x_k}\right)\right) + \frac{\partial}{\partial x_j}(-\rho\overline{u_i^{'}u_j^{'}}) \quad (3.58)$$

These equations are called Reynolds-averaged Navier-Stokes (RANS) equations, which have the same form of the instantaneous Navier-Stokes equations but with some solution variables representing time-averaged values, and additional terms (Reynolds stresses, $-\rho\overline{u_i^{'}u_j^{'}}$) representing the effects of turbulence.

For variable-density flows, the velocities represent mass-averaged values and thus the equations can still be applied.

3.5.2.2 Boussinesq Approach

A common method to model the Reynolds stresses required for the Reynolds-Averaged approach is the Boussinesq hypothesis which relate the Reynolds stresses to the mean velocity gradients:

$$-\rho\overline{u_i'u_j'} = \mu_t\left(\frac{\partial u_i}{\partial x_j} + \frac{\partial u_j}{\partial x_i}\right) - \frac{2}{3}\left(\rho k + \mu_t\frac{\partial u_k}{\partial x_k}\right)\delta_{ij} \quad (3.59)$$

This hypothesis is used in the Spalart-Allmaras model, the k- ε models, and the k- ω models with the advantage of relatively low computational resources associated with the computation of the turbulent viscosity, μ_t.

In the Spalart-Allmaras model, only one additional transport equation representing turbulent viscosity is solved. In the case of the k-ε and k-ω models, two additional transport equations (for the turbulence kinetic energy, k, and either the turbulence dissipation rate, ε, or the specific dissipation rate, ω) are solved, and μ_t is computed as a function of k and ε or k and ω.

The disadvantage of the Boussinesq hypothesis is that it assumes μ_t is an isotropic scalar quantity, which is not strictly true.

3.5.2.3 RNG $k-\varepsilon$ Model

The RNG $k-\varepsilon$ model has a similar form to the standard $k-\varepsilon$ model, but was derived using a rigorous statistical technique called renormalization group theory, and includes various improvements such as:

1. An additional term in its ε equation that significantly improves the accuracy for rapidly strained flows;

2. The effect of swirl on turbulence, enhancing accuracy for swirling flows.

3. An analytical formula for turbulent Prandtl numbers, while the standard k- ε model uses user-specified, constant values;

4. While the standard k- ε model is a high-Reynolds-number model, the RNG theory provides an analytically-derived differential formula for effective viscosity that accounts for low-Reynolds-number effects.

These features make the RNG k- ε model more accurate and reliable for a wider class of flows than the standard k- ε model.

The transport equations for the RNG k- ε model are:

$$\frac{\partial}{\partial t}(\rho k) + \frac{\partial}{\partial x_i}(\rho k u_i) = \frac{\partial}{\partial x_j}\left(\alpha_k \mu_{eff} \frac{\partial k}{\partial x_j}\right) + G_k + G_b - \rho\varepsilon - Y_M + S_k \quad (3.60)$$

$$\frac{\partial}{\partial t}(\rho \varepsilon) + \frac{\partial}{\partial x_i}(\rho \varepsilon u_i) = \frac{\partial}{\partial x_j}\left(\alpha_\varepsilon \mu_{eff} \frac{\partial \varepsilon}{\partial x_j}\right) + C_{1\varepsilon}\frac{\varepsilon}{k}(G_k + C_{3\varepsilon}G_b) - C_{2\varepsilon}\rho\frac{\varepsilon^2}{k} - R_\varepsilon + S_\varepsilon \quad (3.61)$$

where G_k is the generation of turbulence kinetic energy due to the mean velocity gradients, G_b is the generation of turbulence kinetic energy due to buoyancy, Y_M represents the contribution of the fluctuating dilatation in compressible turbulence to the overall dissipation rate, α_k and α_ε are the inverse effective Prandtl numbers for k and ε, respectively, and S_k and S_ε are user-defined source terms.

The scale elimination procedure in RNG theory results in a differential equation for turbulent viscosity, which in the high-Reynolds-number limit yields:

$$\mu_t = \rho C_\mu \frac{k^2}{\varepsilon} \quad (3.62)$$

with $C_\mu = 0.0845$ derived using RNG theory. The main difference between the RNG and standard k- ε models lies in the additional term in the ε equation given by:

$$R_\varepsilon = \frac{C_\mu \rho \eta^3 (1 - \eta/\eta_0)}{1 + \beta\eta^3}\frac{\varepsilon^2}{k} \quad (3.63)$$

where $\eta \equiv Sk/\varepsilon$, $\eta_0 = 4.38$ and $\beta = 0.012$.

The model constants have values derived analytically by the RNG theory, and by default FLUENT uses $C_\mu = 0.0845$, $\alpha_k = \alpha_\varepsilon = 1.39$, $C_{1\varepsilon} = 1.42$ and $C_{2\varepsilon} = 1.68$.

More information on this model can be found in [11].

3.5.2.4 Near-Wall Treatment

The no-slip condition must be applied to any wall bounding a flow, thus affecting the mean velocity field near it, and consequently turbulent flows are also significantly affected by the

presence of walls.

Very close to the wall, viscous damping reduces the tangential velocity fluctuations, while kinematic blocking reduces the normal fluctuations. Toward the outer part of the near-wall region, however, the turbulence is rapidly augmented by the production of turbulence kinetic energy due to the large gradients in mean velocity.

The near-wall modeling significantly impacts the fidelity of numerical solutions, since walls are one of the main sources of mean vorticity and turbulence. Therefore, accurate representation of the flow in the near-wall region determines successful predictions of wall-bounded turbulent flows.

The near-wall region can be subdivided into three layers:

1. Viscous sublayer: the innermost layer where the flow is almost laminar, and the molecular viscosity plays a dominant role;

2. Fully-turbulent layer: the outer layer, where turbulence plays a major role;

3. Buffer layer, a transition region between the viscous sublayer and the fully turbulent layer where the effects of molecular viscosity and turbulence are equally important.

Illustrated in Fig. 3.10 as semi-log coordinates U^+ vs. $\ln(y^+)$, where $U^+ = U/U_\tau\, y$ represents the normal distance to the wall, $y^+ \equiv \rho u_\tau y/\mu$ and $u_T = \sqrt{\tau_w/\rho}$.

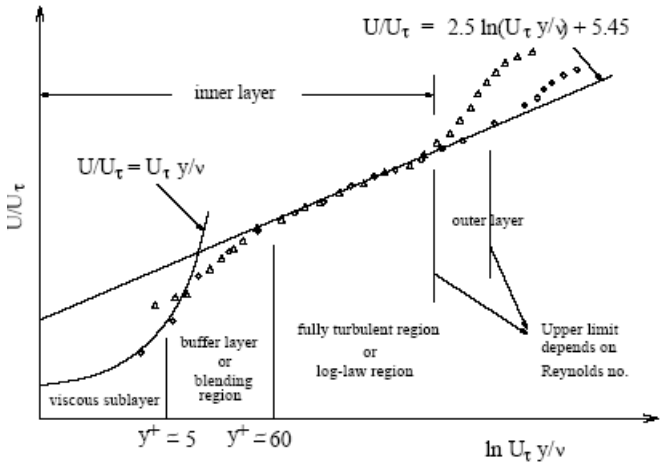

Figure 3.10: Subdivisions of the Near-Wall Region [11]

Generally there are two approaches to model the near wall region, schematised in Fig. 3.11:

1. Not solving the viscosity-affected inner region, and ”bridge” the viscosity-affected region between the wall and the fully-turbulent region with semi-empirical formulas called wall functions;

2. Modifying turbulence models in order to resolve the viscosity-affected region with a mesh all the way to the wall.

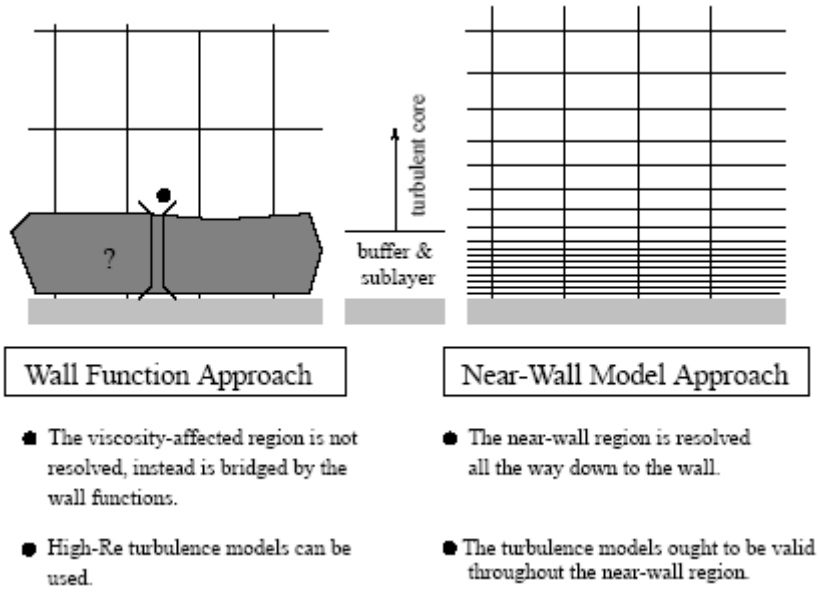

Figure 3.11: Near-Wall treatments [11]

For the standard wall functions provided as the default option in FLUENT, the law-of-the-wall for mean velocity yields:

$$U^* = \frac{1}{k} \ln (Ey^*) \quad (3.64)$$

$$U^* \equiv \frac{U_P C_\mu^{1/4} k_P^{1/2}}{\tau_w / \rho} \quad (3.65)$$

$$y^* \equiv \frac{\rho C_\mu^{1/4} k_P^{1/2} y_P}{\mu} \quad (3.66)$$

where U^* is the dimensionless velocity, y^* is the dimensionless distance from the wall, k the Von Kármán constant equal to 0.4187, E the empirical constant equal to 9.793, U_P and k_P the mean velocity of the fluid and the turbulence kinetic energy at the near-wall node P, y_P the distance from point P to the wall and μ the dynamic viscosity of the fluid.

The logarithmic law for mean velocity is known to be valid for $30 < y^* < 300$ and is employed in FLUENT when $y^* > 11.2250$.

If the mesh is such that $y^* < 11.225$ at the wall-adjacent cells, FLUENT applies the laminar stress-strain relationship $U^* = y^*$.

Therefore, each wall-adjacent cell's centroid should be located within the log-law layer, $30 < y^+ < 300$. A y^+ value close to the lower bound ($y^+ \approx 30$) is most desirable. Although the conventional wall functions can be used with fine near-wall meshes of $y+ < 11.2$, ideally their use should be avoided. As much as possible, the mesh should be made either coarse or fine enough to prevent the wall-adjacent cells from being placed in the buffer layer ($y^+ = 5 \sim 30$), and the use of high-expansion ratios in the direction normal to the wall should also be avoided.

Reynolds' analogy between momentum and energy transport gives a similar logarithmic law for mean temperature.

In highly compressible flows, the temperature distribution in the near-wall region can be significantly different from that of low subsonic flows, due to the heating by viscous dissipation. Thus FLUENT includes the contribution from the viscous heating in the temperature wall functions.

In the k- ε models the k equation is solved in the whole domain including the wall-adjacent cells, with $\partial k/\partial n = 0$ the boundary condition for k imposed at the wall, where n is the local coordinate normal to the wall.

Thus, the production of k is based on the logarithmic law and is computed from:

$$G_k \approx \tau_w \frac{\partial U}{\partial y} = \tau_w \frac{\tau_w}{k\rho k_P^{1/2} y_P} \quad (3.67)$$

and ε is computed from:

$$\varepsilon_P = \frac{C_\mu^{3/4} k_P^{3/2}}{k y_P} \quad (3.68)$$

The wall-function approach is popular because it is economical, robust, and can be reasonably accurate, which make it the best option for near-wall treatments in most flow simulations. It can however be inadequate in situations where the low-Reynolds-number effects are pervasive and the assumptions underlying the wall functions cease to be valid.

More information on near-wall treatment can be found in [11].

3.5.3 Flow Solvers

Two numerical methods can be chosen in FLUENT: the pressure-based solver and the density-based solver.

Historically speaking, the pressure-based approach was developed for low-speed incompressible flows, while the density-based approach was mainly used for high-speed compressible flows. More recently both methods have been extended and reformulated to solve and operate for a wide range of flow conditions, however, for high-speed compressible flows such as the ones tackled in this study, the density-based solver is superior.

In both methods the velocity field is obtained from the momentum equations. In the density-based approach, the continuity equation is used to obtain the density field.

FLUENT solves the governing integral equations for the conservation of mass, momentum, energy and other scalars such as turbulence with a control-volume-based technique that consists of:

1. Division of the domain into discrete control volumes using a computational grid;

2. Integration of the governing equations on the individual control volumes to construct algebraic equations for the discrete dependent variables such as velocities, pressure, temperature, and conserved scalars;

3. Linearization of the discretized equations and solution of the resultant linear equation system to yield updated values of the dependent variables.

Because the governing equations are non-linear and coupled, several iterations of the solution loop must be performed before a converged solution is obtained. Each iteration goes through the steps in Fig's. 3.12 flowchart:

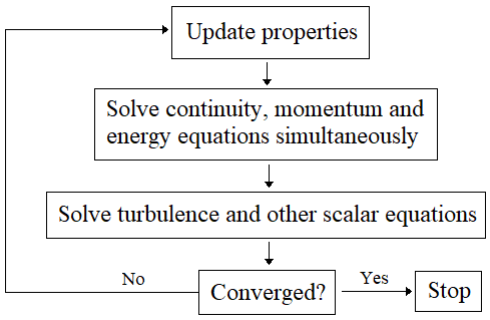

Figure 3.12: Density-based solution method [11]

When solving the coupled system of equations either the coupled-explicit formulation or the coupled-implicit formulation can be used.

In the implicit formulation, which will be the one employed for the simulations present in this study, for a given variable, the unknown value in each cell is computed using a relation that includes both existing and unknown values from neighbouring cells. Therefore each unknown will appear in more than one equation in the system, and these equations must be solved simultaneously to give the unknown quantities.

Chapter 4

Methodology

4.1 Nozzle Design

In order for a supersonic nozzle to work properly and maximise efficiency, the ideal contour must be found in to prevent shock waves from occurring inside the duct. The MOC described in Chapter 3 provides the technique for designing such a nozzle to be shockfree, considering isentropic two-dimensional flow.

In order to minimize weight and drag, the nozzles designed for rocket or hypersonic vehicle applications are required to be as short as possible in length. Such nozzle type is usually referred to as Minimum Length Nozzle (MLN), where the expansion takes place through a centered Prandtl-Meyer wave starting from a sharp corner at the nozzle inlet (throat) with an angle θ^*, as shown in Fig. 4.1.

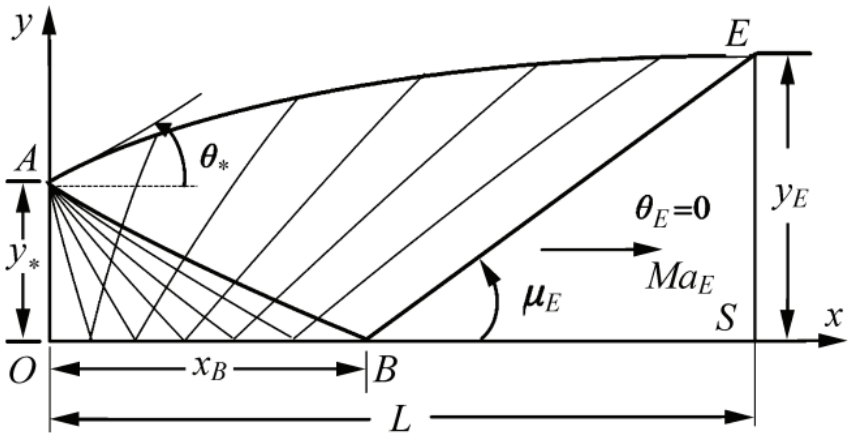

Figure 4.1: Flowfield illustration of a Minimum Length Nozzle [12]

The flow between the nozzle throat OA and the nozzle exit SE can be divided into three regions:

1. Region OAB, the kernel zone. This is considered a non-simple waves region, where two types of waves intersect each other, the ones from the initial expansion and the ones reflected from the centerline x_B.

2. Region ABE, the transition zone. A simple wave region, where the reflected waves are cancelled by the nozzle upper wall contour.

3. Region BSE, the uniform zone. In this zone the flow is uniform and parallel to the nozzle axis, with the desired exit Mach number M_E

Thus, at points B and E the Mach number is the design exit Mach M_E and the flow direction is $\theta = 0°$.

As can be observed, the characteristics emanating from the sharp corner at point A are reflected within the known distance x_B, thus, an asymmetric nozzle (SERN) composed by the upper expansion ramp (AE) and a lower flap (OB) with a minimum length of x_B can be designed by this method.

Hence, along the C_+ characteristic BE, the Prandtl-Meyer function $\nu(M) = \nu(M_B) = \nu(M_E)$. Considering the C_- characteristic through points A and B, at point B:

$$\theta_B + \nu_B = (K_-)_B \quad (4.1)$$

$$(K_-)_B = \nu(M_E) \quad (4.2)$$

At point A:

$$\theta^* + \nu(M_A) = (K_-)_A \quad (4.3)$$

And we know that at point A, because of the Prandtl-Meyer expansion $\nu(M_A) = \theta^*$. Thus:

$$\theta^* = \frac{1}{2}(K_-)_A \quad (4.4)$$

$$\theta^* = \frac{1}{2}(K_-)_B \quad (4.5)$$

Combining Eq. 4.4 and 4.5:

$$\theta^* = \frac{\nu(M_E)}{2} \quad (4.6)$$

Which demonstrates that for a MLN, the expansion angle of the wall downstream of the throat (maximum flow turning angle, θ^*) is uniquely defined by the design exit Mach number and the specific heat ratio γ.

It is now possible to proceed with the nozzle design, by computing the entire initial expansion fan as a finite number of n lines, or characteristics. The greater the number n of characteristics used to calculate the nozzle contour, the more accurate the results will be.

In order to generate the two-dimensional MLN nozzle contours required in this study, a Python code was implemented, and its results verified.

The code takes as input:

1. the desired exit Mach number M_E of the nozzle;

2. the specific heat ratio γ at which the nozzle operates;

3. the desired number of characteristic lines n.

The first characteristic is chosen to be slightly inclined from the vertical axis, $\Delta\theta = \theta^*/n$. The remainder of the expansion fan is divided into equally spaced increments from the initial line $\Delta\theta$ to θ^*.

Given the values of θ^*, $\Delta\theta$ and n, the MOC will then calculate K_-, K_+, θ and ν at each discrete point within the nozzle flowfield and at its walls.

These discrete points correspond to the points of intersection of the initial expansion waves with the centerline, the points where the reflected waves meet the upper nozzle wall, and the points in the kernel zone where the waves intersect each other.

After applying the MOC, a numerical inversion of the Prandtl-Meyer relation [1] (in Appendix A) is used in order to obtain the Mach number M of each point (with an error of less than 0.05%) from the values of ν and γ.

After discovering the value of the Mach number M at each point throughout the nozzle, pressure, temperature and density can be calculated through isentropic relations, and its contours plotted.

Finally, point by point, through geometric and trigonometric relations, the characteristic lines connecting all the points (characteristics web) and the nozzle contour are drawn. This result can be seen in Fig. 4.3.

The code also allows the user to export the wall points x and y coordinates to an Excel .csv file, which can then be imported into a Computer Aided Design (CAD) software, like CATIA

V5 or SOLIDWORKS.

4.2 Python Algorithm Results and Validation

As previously explained, the code will then compute discrete points of the whole flowfield inside the nozzle as well as its wall contour.

Before proceeding further, the results were firstly compared to those of the example in [4] for the graphical construction (Fig. 4.2) of a two-dimensional MLN nozzle for the expansion of air ($\gamma = 1.4$) to a design $M_E = 2.4$, using $n = 7$ characteristic lines.

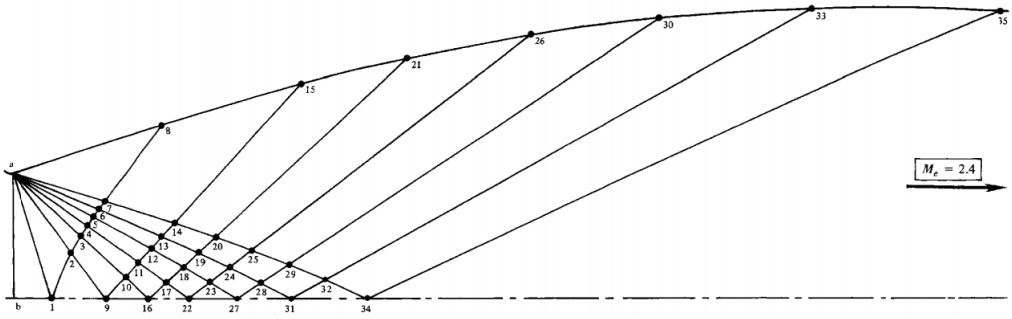

Figure 4.2: Graphical construction for [4] example

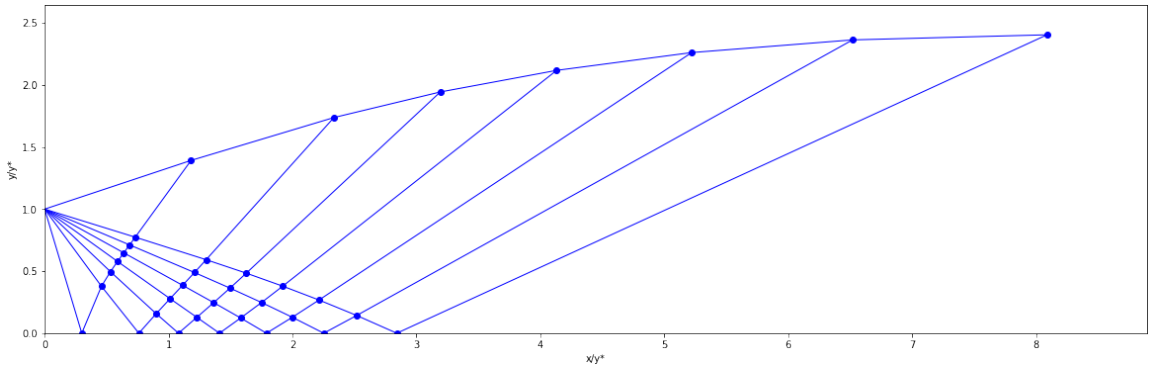

Figure 4.3: Nozzle contour and characteristics web generated by the Python algorithm

Table 4.1: Wall points values [4]

Point	K_-	K_+	θ	ν	M	μ
8	36.75	0	18.375	18.375	1.72	35.6
15	36.75	-6.75	15	21.75	1.84	32.9
21	36.75	-12.75	12	24.75	1.94	31.0
26	36.75	-18.75	9	27.75	2.05	29.2
30	36.75	-24.75	6	30.75	2.16	27.6
33	36.75	-30.75	3	33.75	2.28	26.0
35	36.75	-36.75	0	36.75	2.4	24.6

Comparing the values of Tab. 4.1 and Tab. 4.2, which are the properties calculated by the MOC for the points that lie on the upper wall of the nozzle, the code results show a good level of accuracy. The slight difference between some values might be due to rounding errors propagating throughout the algorithm. Also, by comparing Fig. 4.2 and Fig. 4.3 it can be

Table 4.2: Wall points values calculated by Python algorithm

Point	K_-	K_+	θ	ν	M	μ
8	36.747	0	18.373	18.373	1.719	35.565
15	36.747	-6.749	14.999	21.748	1.836	33.009
21	36.747	-12.749	11.999	24.748	1.941	31.003
26	36.747	-18.748	8.999	27.747	2.050	29.194
30	36.747	-24.748	5.999	30.747	2.162	27.544
33	36.747	-30.747	2.999	33.747	2.279	26.027
35	36.747	-36.747	0	36.747	2.400	24.621

noted that the spatial position of the points is also being calculated correctly. The nozzle dimensions are in terms of the nozzle throat height y^*, which takes the value of 1.

4.2.1 Characteristic Lines Associated Error

The percentage error ε associated with the nozzle contour design was measured by comparing the Nozzle Area Ratio (NAR) of the nozzle obtained by the algorithm, with the theoretical NAR isentropic relation (Eq. 3.19) for the same M_E and γ.

$$\% \, \varepsilon = \frac{|NAR_{code} - NAR_{isentropic}|}{NAR_{isentropic}} * 100 \quad (4.7)$$

The number of characteristic lines n chosen is inversely proportional to the NAR error, and thus a greater number of characteristics generates a more accurate nozzle contour.

The larger the number of characteristics used, the smaller the angle increment between the lines of the expansion fan will be, resulting in a more closely spaced characteristics web throughout the nozzle, as can be seen in Figs 4.4, 4.5, 4.6 and 4.7, where the same nozzle contour ($M_E = 2.4$, $\gamma = 1.4$) is generated with 25, 50, 100 and 200 characteristic lines. The smoothness of the wall contour will also increase, since it is created by connecting the wall points with line segments.

It can also be observed that, due to the numerical discrete approach of dividing the expansion fan and its reflection as a finite number of characteristic lines, there is a discontinuity zone between the nozzle throat and the first reflected characteristic, where there are no data points and the nozzle wall contour is assumed to be a straight line. For the purposes of this study, the effects of this discontinuity are negligible.

The plot in Fig. 4.8 shows the NAR error as a function of the number of characteristics used to generate the nozzle contour ($5 > n > 100$). For $n > 10$, the error is below 1%, and for $n > 80$, the error is close to 0 (0.045%) and the variation by adding characteristic lines is negligible.

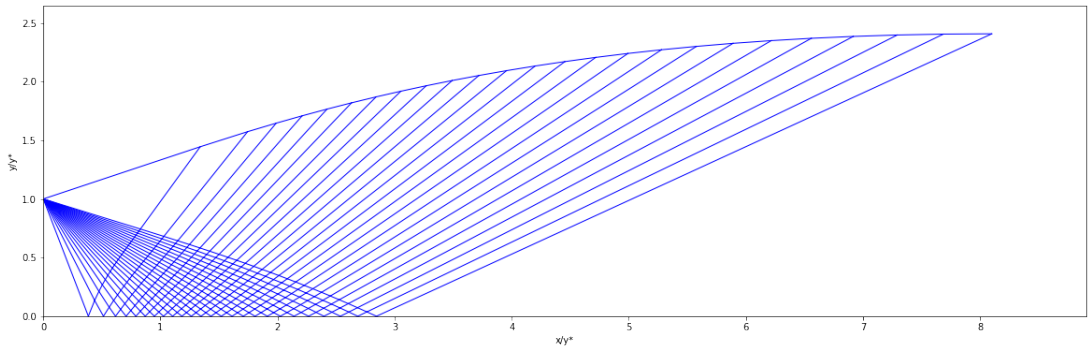

Figure 4.4: Characteristics web density comparison: $n = 25$

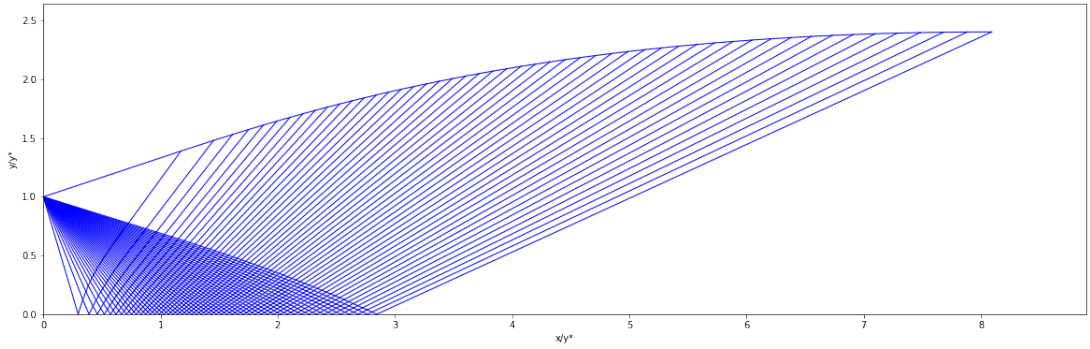

Figure 4.5: Characteristics web density comparison: $n = 50$

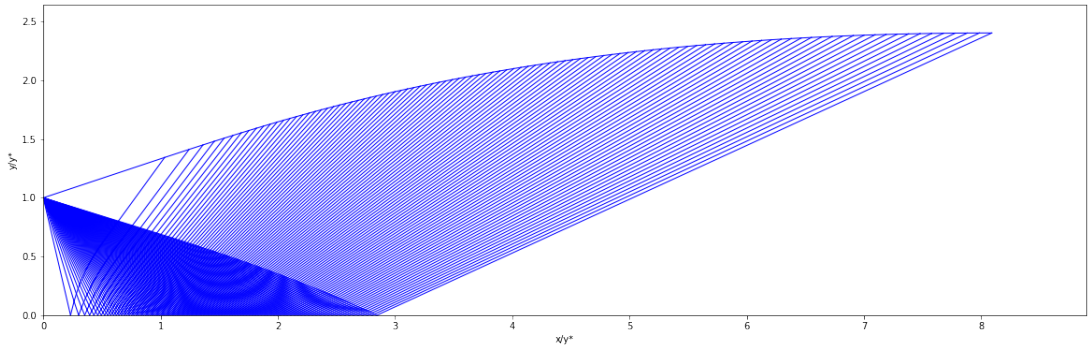

Figure 4.6: Characteristics web density comparison: $n = 100$

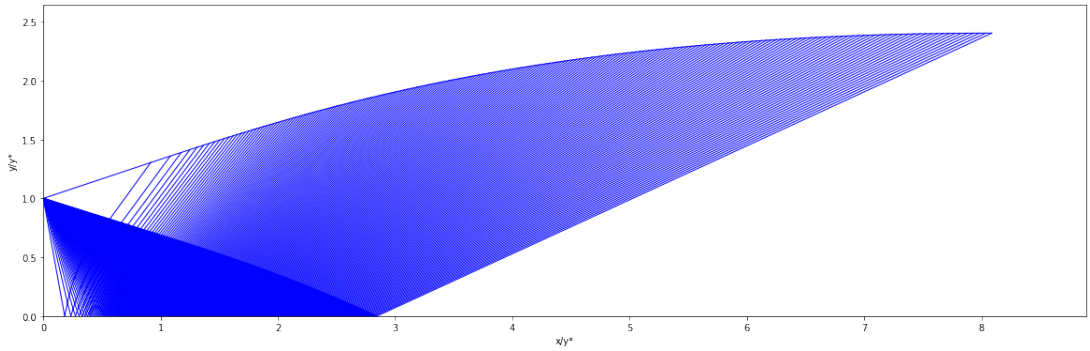

Figure 4.7: Characteristics web density comparison: $n = 200$

In order to save computational resources while maintaining a good level of accuracy, the nozzle contours used in the following part of this study will be generated with a number of

characteristic lines equal to 100.

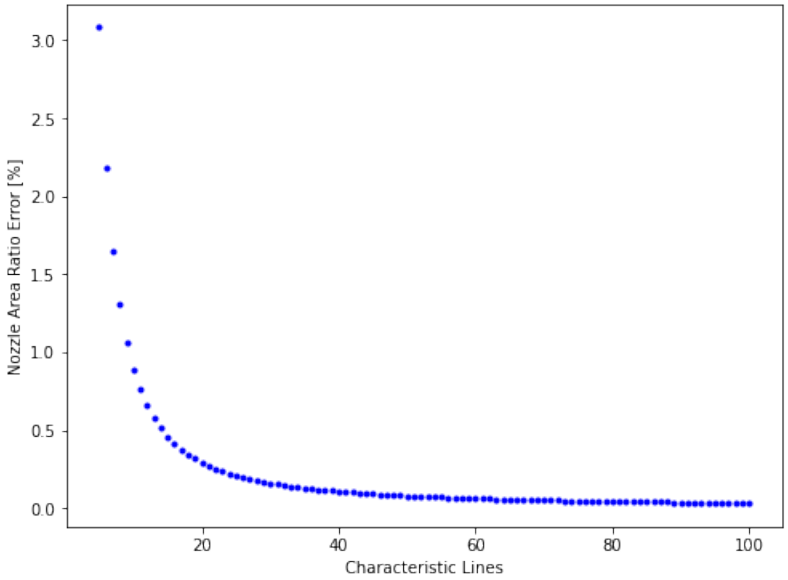

Figure 4.8: NAR error as a function of the number of characteristics used to generate the nozzle contour ($5 > n > 100$)

4.2.2 Nozzle Flowfield Properties

As described previously, since the properties of the flow within the nozzle are known at each discrete point, this allows the algorithm to plot its contours.

Plus, the code stores the values of the points along the lower nozzle flap and along the nozzle upper wall, thus it is possible to plot the variations of these properties along the nozzle walls:

1. Mach number, M (Fig. 4.9 and Fig. 4.10);
2. Temperature static to total ratio, T/T_0 (Fig. 4.11 and Fig. 4.12);
3. Pressure static to total ratio, p/p_0 (Fig. 4.13 and Fig. 4.14);
4. Density static to total ratio, ρ/ρ_0 (Fig. 4.15 and Fig. 4.16).

By performing a quick analysis of the contours and plots produced by the algorithm for a nozzle with $M_E = 2.4$ and $\gamma = 1.4$, it is possible to conclude they show good agreement with the theoretical notions presented earlier.

The Mach number, which is equal to 1 at the nozzle inlet $x/y^* = 0$ (throat), gradually increases throughout the nozzle as the flow accelerates due to the area expansion (increase in NAR (A/A^*)). At the nozzle exit, the Mach number M_E is equal to 2.4, which was the desired M_E in this example.

Fig. 4.10 also show this increase in Mach number along both the upper wall and the lower

flap of the nozzle.

Note that the initial spikes in the upper wall plots are due to the discontinuity of data points immediately downstream of the nozzle throat.

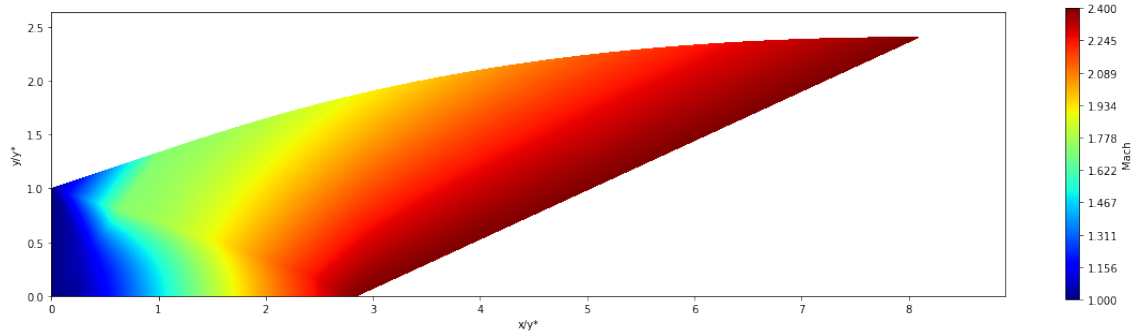

Figure 4.9: Algorithm Mach number contours ($M_E = 2.4, \gamma = 1.4$)

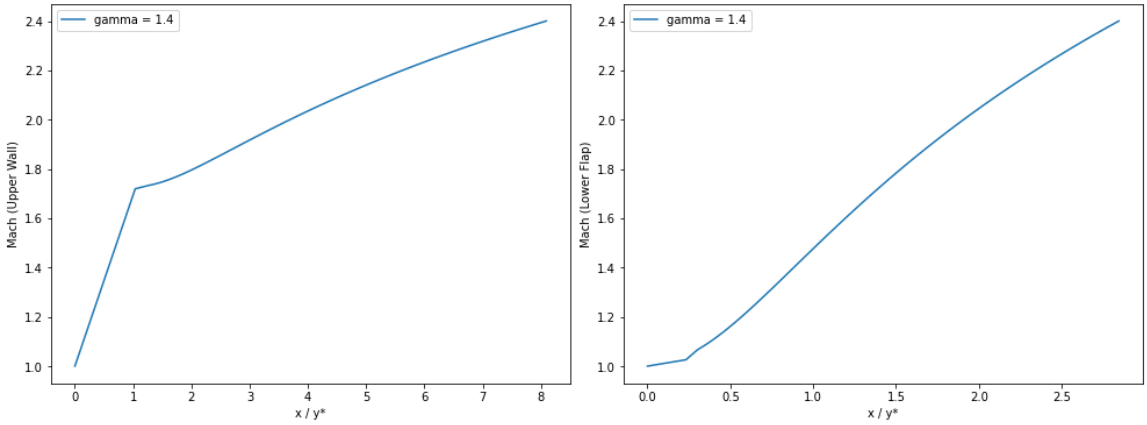

Figure 4.10: Mach number variation along nozzle upper wall and lower flap ($M_E = 2.4, \gamma = 1.4$)

The static to total ratios of temperature T/T_0, pressure p/p_0 and density ρ/ρ_0 throughout the nozzle also show good agreement with the isentropic flow relations presented earlier.

At the throat ($M = 1$), $T^*/T_0 = 0.833$, $p^*/p_0 = 0.528$ and $\rho^*/\rho_0 = 0.634$, which are the correct values for isentropic flow at sonic conditions.

As the flow expands and accelerates through the nozzle, a decrease in static temperature, pressure and density is noticeable. At the nozzle exit, the ratio values are $T/T_0 = 0.465$, $p/p_0 = 0.068$ and $\rho/\rho_0 = 0.147$, which are the correct values for isentropic flow at $M = 2.4$.

4.2.3 Boundary Layer Correction

The nozzle contours generated directly from the MOC algorithm are based on the assumption of inviscid flow. However, in reality, due to the flow viscosity and wall friction, there will be a viscous boundary layer formation along the nozzle walls. The increasing thickness of boundary layers of the nozzle walls leads to a reduction of the effective cross-section area of the flow zone, thus affecting nozzle performance.

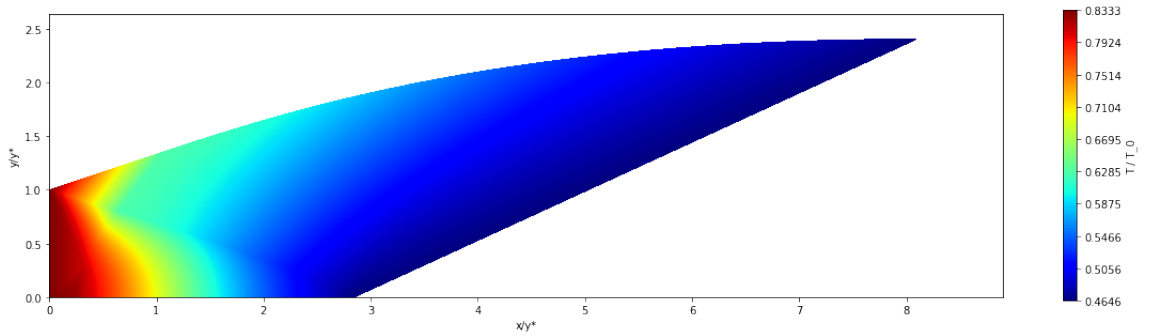

Figure 4.11: Algorithm T/T_0 contours ($M_E = 2.4$, $\gamma = 1.4$)

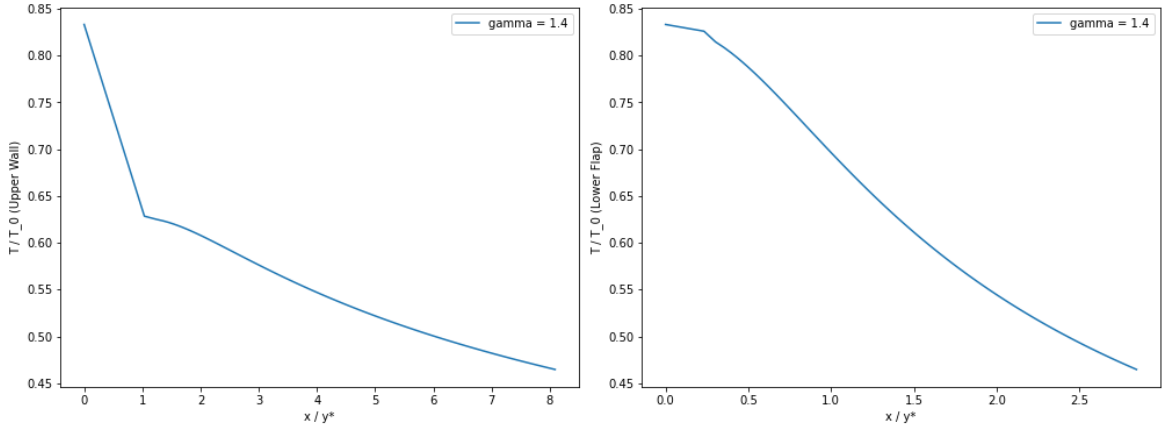

Figure 4.12: T/T_0 variation along nozzle upper wall and lower flap ($M_E = 2.4$, $\gamma = 1.4$)

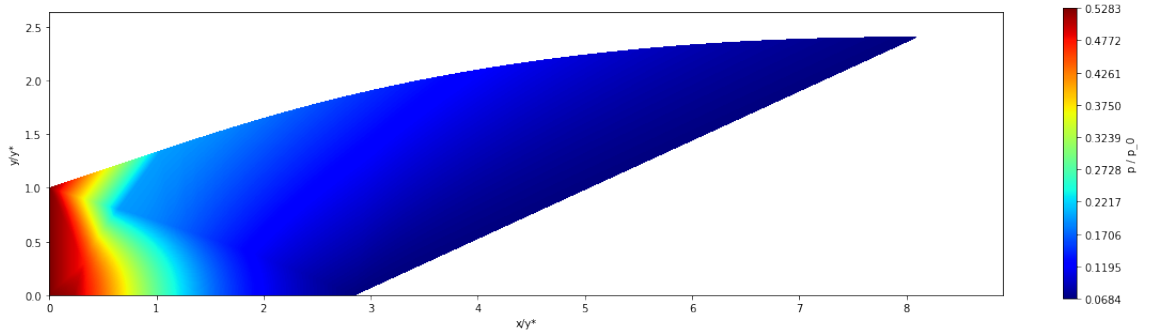

Figure 4.13: Algorithm p/p_0 contours ($M_E = 2.4$, $\gamma = 1.4$)

In order to prevent this reduction in the flow's effective cross-sectional area, an optional subroutine which applies a boundary layer correction was added to the main code, where the nozzle walls are moved a distance of δ along the outward normal direction. This value of δ can be calculated theoretically or through empirical evaluation.

Due to its simplicity and accuracy, the following empirical evaluation [14] dependant mainly on the nozzle's exit Mach number M_E (valid for $M_E < 10$) will be employed in this study:

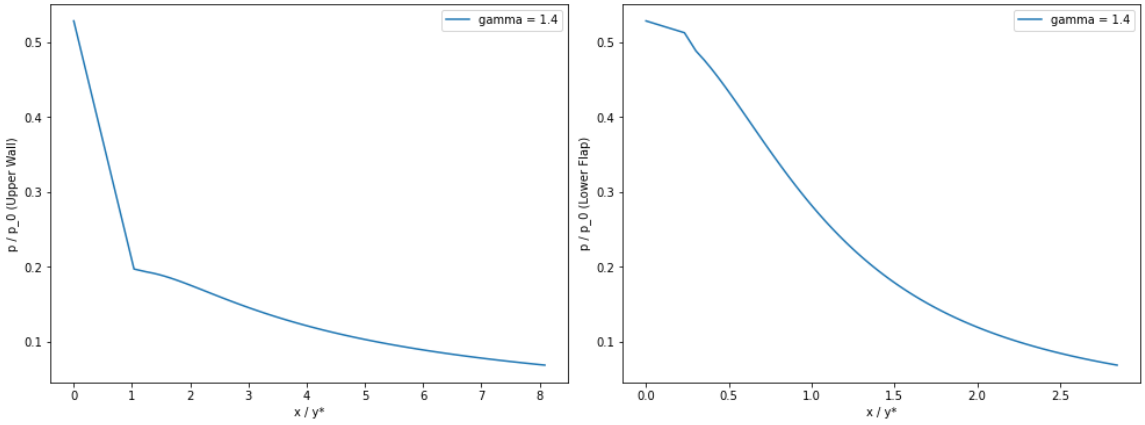

Figure 4.14: p/p_0 variation along nozzle upper wall and lower flap ($M_E = 2.4, \gamma = 1.4$)

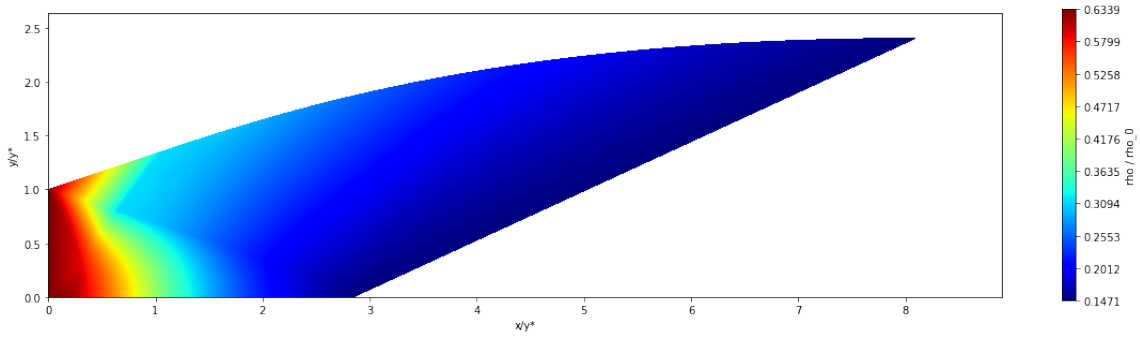

Figure 4.15: Algorithm ρ/ρ_0 contours ($M_E = 2.4, \gamma = 1.4$)

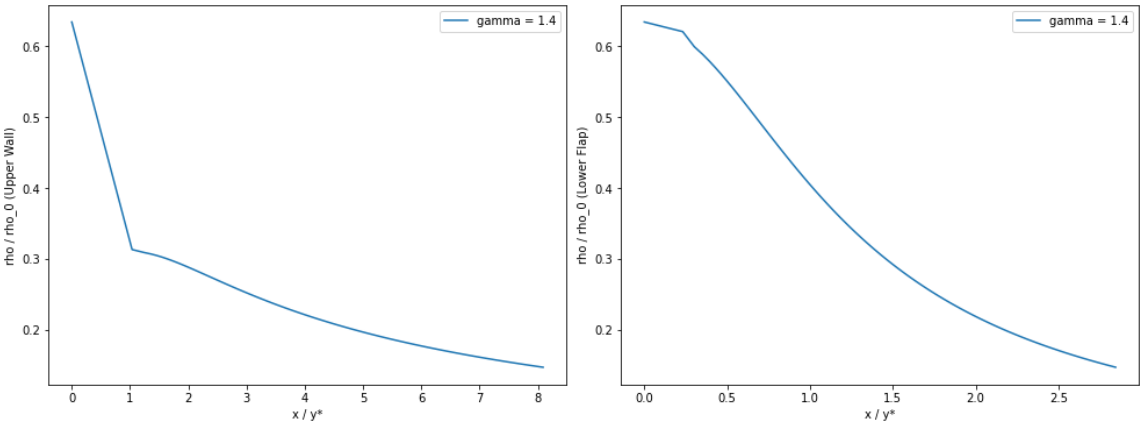

Figure 4.16: ρ/ρ_0 variation along nozzle upper wall and lower flap ($M_E = 2.4, \gamma = 1.4$)

$$\delta = 0, \; x = 0 \quad (4.8)$$

$$\frac{d\delta}{dx} = \tan(\varepsilon) \quad (4.9)$$

where ε is the correction angle of the boundary layer, and its relation with the exit Mach

number M_E is shown in Tab. 4.3:

Table 4.3: Discrete values for ε with respect to M_E [14]

M_E	2	4	6	8	10
ε (°)	0.5	0.5	0.7	1.5	2.0

For ε and M_E values besides the ones in Tab. 4.3, the following approximation was adopted:

1. $\varepsilon = 0.5$ for $M_E \leq 4$ values;

2. for $4 < M_E \leq 8$ values, the 2$^{\text{nd}}$ degree polynomial approximation $\varepsilon = 0.075M_E^2 - 0.65M_E + 1.9$ was employed ;

3. for $8 < M_E \leq 10$ values, the linear approximation $\varepsilon = 0.25M_E - 0.5$ was used.

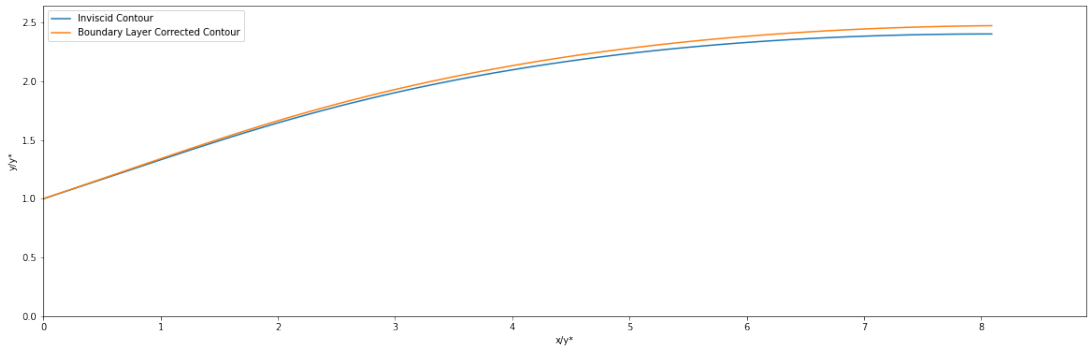

Figure 4.17: Comparison between inviscid and boundary layer corrected nozzle geometry ($M_E = 2.4, \gamma = 1.4$)

Fig. 4.17 shows the regular inviscid nozzle contour generated by the MOC algorithm (in blue) and the same contour with the boundary layer correction applied (in orange). The wall displacement δ to account for viscous effects is clearly visible, and increases towards the nozzle exit, were it reaches its maximum value.

It is important to state that there are more precise methods for calculating the thickness of the boundary layer, however they are also more complex. Therefore, for the purposes of this preliminary study, the boundary layer correction provided by this method is considered sufficient.

4.2.4 Input Values Influence on Nozzle Geometry

By testing various input values of M_E and γ, the algorithm allows the visualisation of the effect of these parameters on the nozzle geometry and other associated properties. This allows one to see some theoretical fundamentals described earlier applied to a practical case.

Fig. 4.18 shows the effect of the specific heat ratio γ on the geometry and size of the nozzle, for a constant exit Mach number $M_E = 2.4$.

The green contour is the shape for a nozzle operating with a flow of $\gamma = 1.4$. However, if

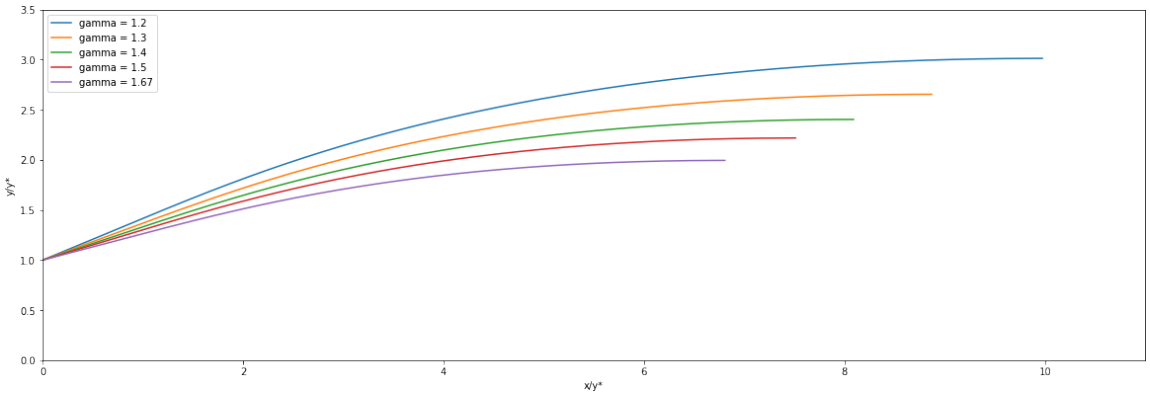

Figure 4.18: Nozzle geometry for various γ values and constant $M_E = 2.4$

the γ of the flow takes other values, in order to correctly expand the exhaust gases the nozzle geometry must change accordingly. A nozzle operating at a lower γ requires a greater NAR and overall length. On the contrary, a higher γ flow requires a smaller nozzle shape.

Fig. 4.19 shows the variation of the maximum flow turning angle θ^*, in degrees, immediately downstream of the throat sharp corner. Since it is mainly dependant upon M_E, we can see the θ^* increases with an increase in M_E. The influence of γ can also be visualised, and its influence becomes more noticeable at higher M_E.

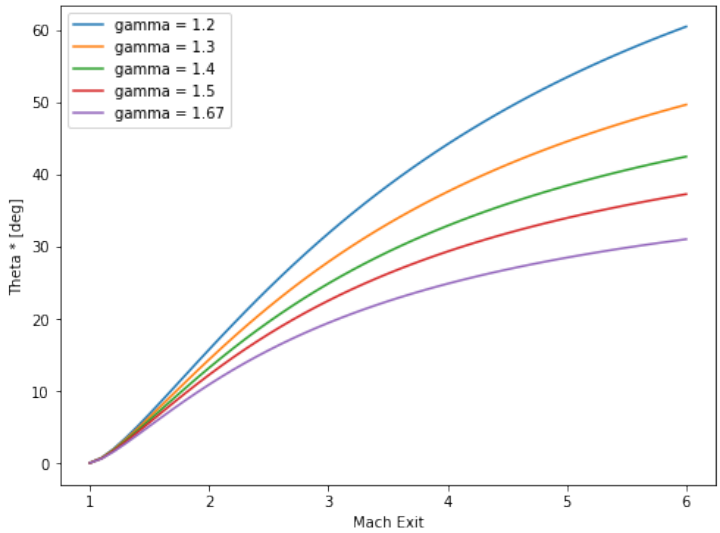

Figure 4.19: θ^* as a function of M_E, for various γ values

The nozzle geometry changes more drastically in terms of the exit Mach number M_E, and can increase exponentially for very high M_E.

Fig. 4.20 shows the nozzle contours required for a perfect shockfree expansion, for M_E ranging from 2 to 5, with constant $\gamma = 1.4$. As can be noted, the NAR and overall nozzle size quickly increase with higher M_E. For a desired exit Mach number of 5, the nozzle length is almost 150 times the height of the throat.

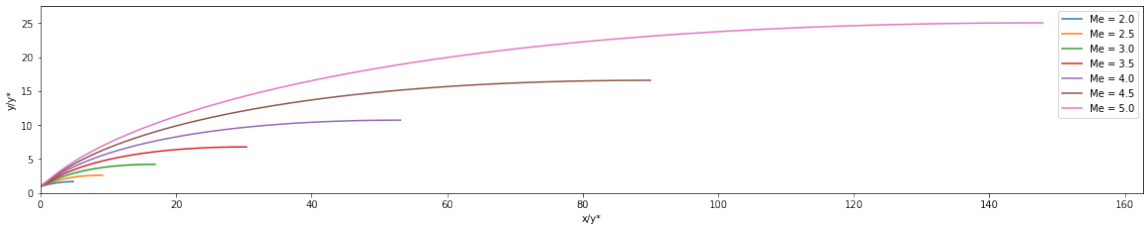

Figure 4.20: Nozzle geometry for various M_E values and constant $\gamma = 1.4$

In the plots of Fig. 4.21 this size dependence upon M_E is also very noticeable. Fig. 4.21 shows the nozzle length as a function of M_E, and Fig. 4.21 shows the NAR also as a function of M_E. In both cases, we can see an exponential behaviour of overall size as the M_E increases. The γ influence can also be visualised, with smaller γ values requiring larger nozzle dimensions, and vice-versa.

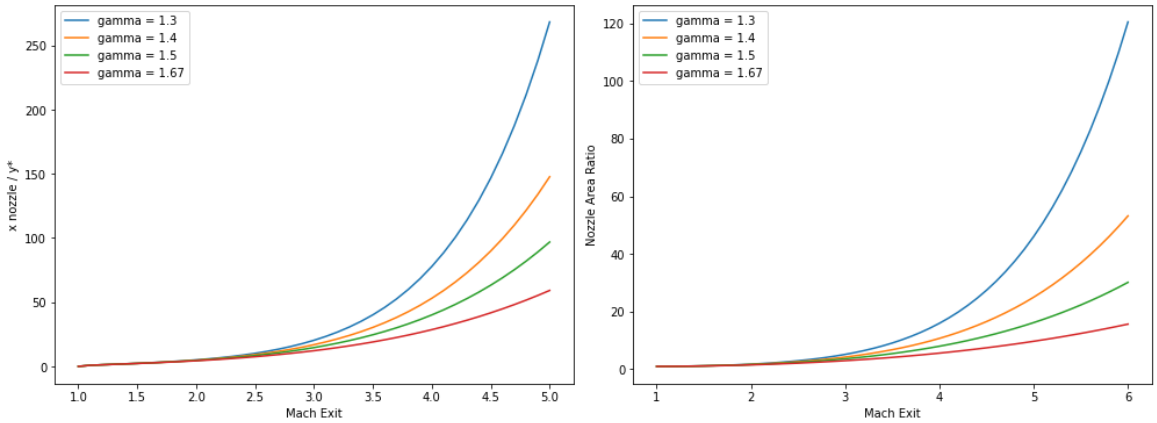

Figure 4.21: Nozzle dimensions (length and height) as a function of exit Mach number M_E, for various γ values

This exponential size increase can lead, in some cases, to the nozzle geometry being simply to large to viability integrate into a hypersonic vehicle. Also, the increase in weight and aerodynamic drag would decrease the overall efficiency of the vehicle. However, according to [13], who studied the variation of stream thrust (a parameter which determines the mass flow rate specific thrust, often used in performance evaluation) along the length of nozzles, most of the thrust is generated by the early expansion process within the nozzle. Their studies also showed that the nozzle could be truncated at approximately 40% of the initial length without significant loss of thrust. Therefore, in high mach supersonic and hypersonic nozzles it is common to apply this truncation as a fair trade off between size and overall nozzle efficiency.

4.2.5 CFD Verification of Nozzle Flow

To further verify the nozzle contours generated by the algorithm, a Computational Fluid Dynamics (CFD) simulation and analysis was carried out, using the commercial software ANSYS FLUENT 16.2.

The nozzle geometry designed for $M_E = 2.4$ operating at $\gamma = 1.4$ was chosen for this first

simulation.

4.2.5.1 Inviscid Case

Firstly, the wall points coordinates that compose the nozzle contour were imported into the CAD commercial software CATIA V5.

The CAD file was then imported to FLUENT, and a sized structured mesh was generated using FLUENT meshing tools. The mesh elements presented an average element quality of 0.929, a minimum orthogonal quality of 0.951 and a maximum orthogonal skewness of 0.0049.

Firstly, an inviscid simulation was carried out in order to directly compare it to the MOC results.

The density-based solver was used, the energy equation was enabled and the air was set to ideal gas. The implicit formulation and the Roe-FDS flux type were used, with a spatial discretization of Least Squares Cell Based gradient and Second Order Upwind flow.

As for the boundary conditions, the nozzle inlet was set as pressure inlet ($p_0 = 1481381$ Pa, $M = 1$, $T_0 = 300$ K), the upper nozzle contour as a wall, the nozzle centerline as symmetry, and the nozzle exit as pressure outlet ($p_\infty = 101325$ Pa, $T_\infty = 300$ K).

A mesh independence study was carried out with the following grids:

1. Coarse, 2000 elements (20 x 100);
2. Medium, 8000 elements (40 x 200);
3. Fine, 32000 elements (80 x 400).

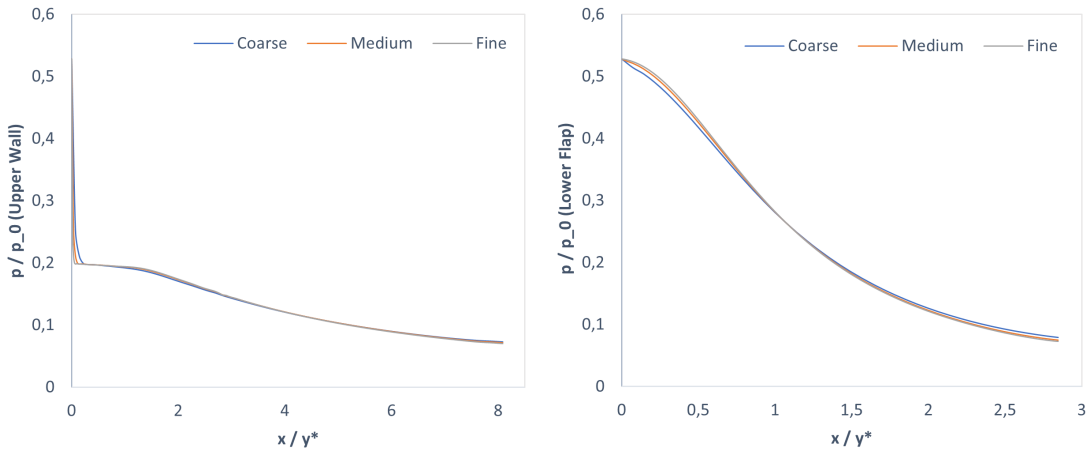

Figure 4.22: Mesh independence study ($M_E = 2.4$, $\gamma = 1.4$)

Fig. 4.22 shows the variation of the static to total pressure ratio, p/p_0 along the nozzle upper wall and lower flap for the three grids tested. From the comparison of the results obtained by the three grid types it can be concluded that there is a slight difference between the coarse grid and the medium and fines grids, but the variation between these last two is negligible. Also, these results show good agreement with the ones obtained by the algorithm (Fig. 4.14), with the exception of the initial upper wall values (approximately $x/y^* < 1$) poorly predicted by the algorithm for reasons explained previously.

Thus, the medium refined mesh was employed in order to save computational resources.

Fig. 4.23 and Fig. 4.24 show the contour of the Mach number and static pressure throughout the nozzle. As predicted by the algorithm, the flow expands and accelerates smoothly from the nozzle inlet ($M = 1$) to the nozzle exit ($M_E = 2.4$) without the presence of shock-waves, accompanied by a decrease in static pressure. Both these contours show good similarity with the ones predicted by the algorithm in Figs. 4.9 and 4.13.

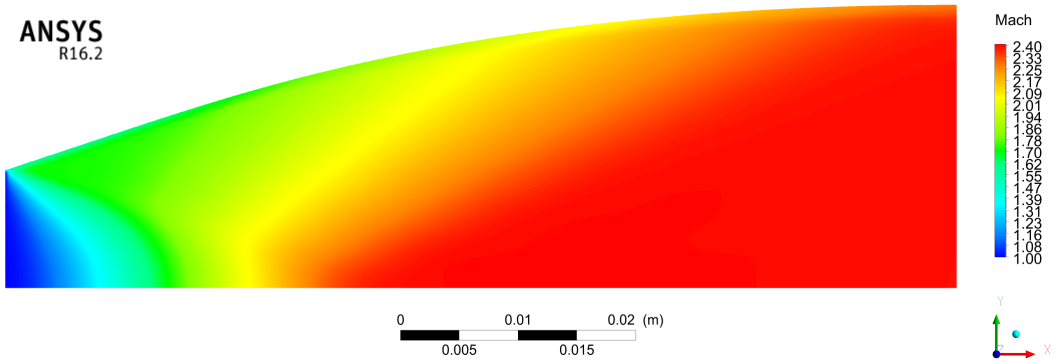

Figure 4.23: FLUENT Mach number contours ($M_E = 2.4$, $\gamma = 1.4$)

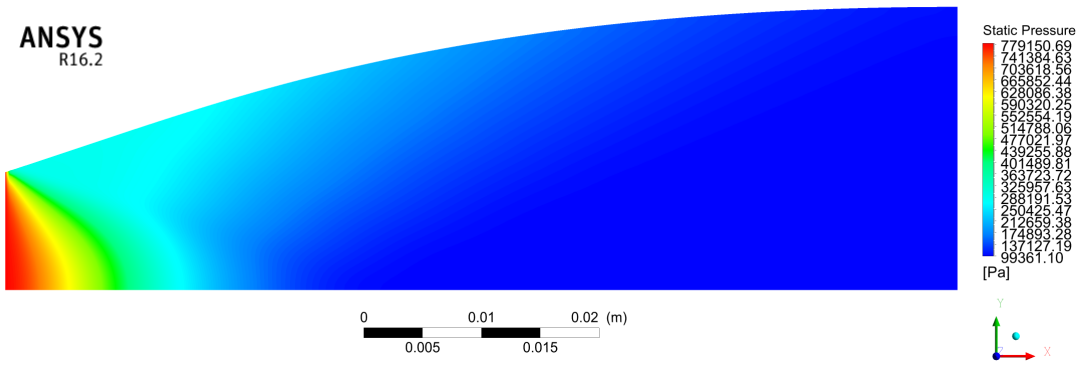

Figure 4.24: FLUENT static pressure contours ($M_E = 2.4$, $\gamma = 1.4$)

In Fig. 4.25 it is possible to observe the flow velocity vectors, which turn upwards immediately downstream of the throat due to the Prandtl-Meyer expansion fan, and become parallel with the nozzle axis at the exit.

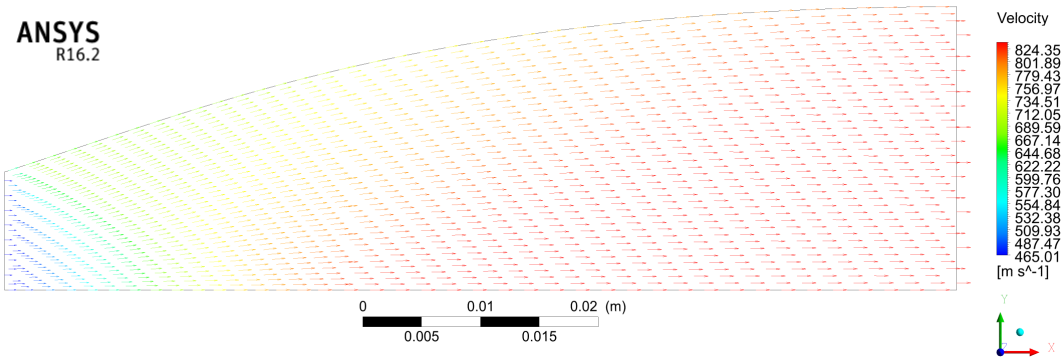

Figure 4.25: FLUENT velocity vectors ($M_E = 2.4, \gamma = 1.4$)

4.2.5.2 Viscous Case

Then, a similar analysis was conducted with the same operating conditions, but this time the effects of viscosity and boundary layer formation along the nozzle wall were taken into account.

The methodology was also similar to the inviscid case, however the wall points were displaced with the boundary layer correcting method described previously, and then imported into FLUENT.

A mesh with the same level of refinement was created, however the refinement level increased towards the wall in order to fully capture the boundary layer formation. In order to evaluate the mesh quality near the wall, the y^+ parameter was analysed, with values varying from around 40 to 60, which are in the $30 < y^+ < 300$ range recommended by FLUENT for near wall treatment.

The $k - \varepsilon$ RNG turbulence model was used, with the default model constants and standard wall functions.

The remaining solver option as well as the boundary conditions were the same as the inviscid case.

In Fig. 4.26 shows the Mach contours throughout the nozzle. Due to the no-slip condition, the flow velocity at the wall is 0, and fluid viscosity leads to the formation of a boundary layer along the nozzle upper wall, as well as its increase in thickness towards the nozzle exit.

Despite the reduction of the nozzle effective cross-sectional area as a result of the boundary layer, the correction applied to the wall geometry allows the M_E to be very close to the design value of 2.4.

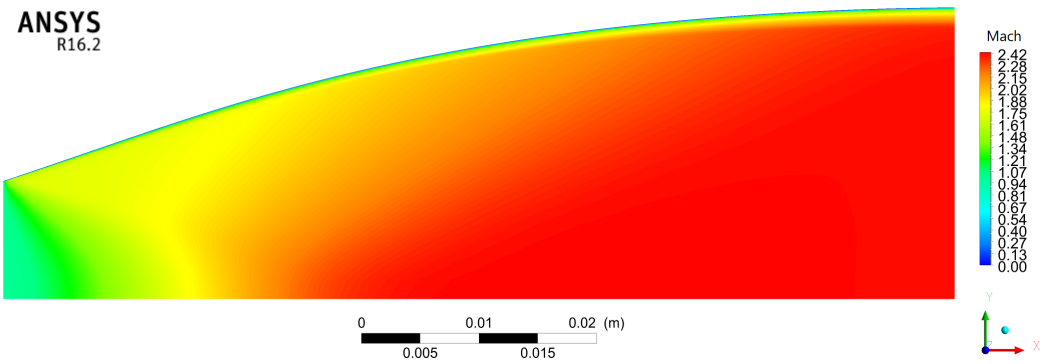

Figure 4.26: FLUENT Mach number contours, with boundary layer formation ($M_E = 2.4$, $\gamma = 1.4$)

4.3 Experimental Validation of Numerical Method

In order to validate the numerical simulation methodology implemented in further cases, a SERN numerical model was created replicating the geometry and conditions of those in the experimental investigation conducted by Yu et al. [8]. By comparing the results of the the experimental test with those of the CFD simulation, one can evaluate the accuracy of the numerical method being used, and validate its capacity for providing results similar to reality, thus enabling it to be used in simulations with similar conditions.

4.3.1 Experimental Setup

The experiment was conducted at the Internal Flow Research Center of Nanjing University of Aeronautics and Astronautics (NUAA), in a cold blow down wind tunnel with a maximum stagnation pressure ranging from 0.8 to 0.9 MPa, and a minimum back pressure ranging from 3 to 5 kPa.

The SERN model tested was a straight expansion ramp with an angle θ^* of 25°, a design NPR of 20 and an expansion area ratio A/A^* of 2.896, with the height of the throat being 20 mm. The schematics of the experimental model can be seen in Fig. 4.27.

During the experiment, schlieren videos were recorded and pressure measurements were taken along the expansion ramp and the flap.

4.3.2 Numerical Simulation Framework

Since the experimental SERN model is a planar nozzle, the flow field at the symmetry plane can be simulated in 2D.

The SERN's geometry was firstly drawn in CATIA V5 and then imported into FLUENT.

A sized structured mesh was then generated in FLUENT, with an average element quality of 0.76, a minimum orthogonal quality of 0.68 and a maximum orthogonal skewness of 0.32. In order to fully capture the flow phenomena inside and downstream of the SERN, the mesh

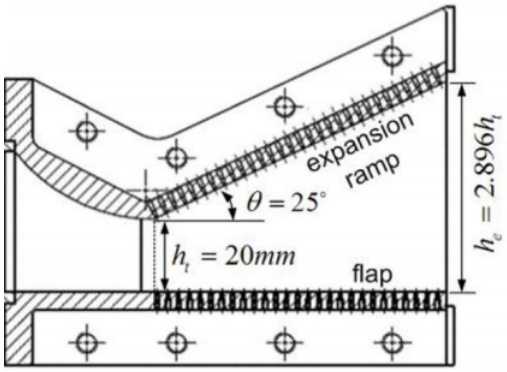

Figure 4.27: Geometry of SERN in experimental test [8]

was refined in these regions, and was coarsened towards the domain's boundaries to save computational resources and simulation time, as shown in Fig. 4.28. The total number of elements was 84885. The y^+ values vary to a large degree due to complex separation phenomena, and the mesh along the ramp and flap was adjusted as required in order to keep it within the range recommended by FLUENT.

The boundary conditions are represented in Fig. 4.28: the nozzle inlet was set as pressure inlet ($p_0 = 93243.66$ Pa, $T_0 = 300$ K), the SERN's geometry as a wall, and the outside domain as pressure outlet and pressure far-field ($p_\infty = 31073.02$ Pa, $T_\infty = 300$ K, $M_\infty = 0$).

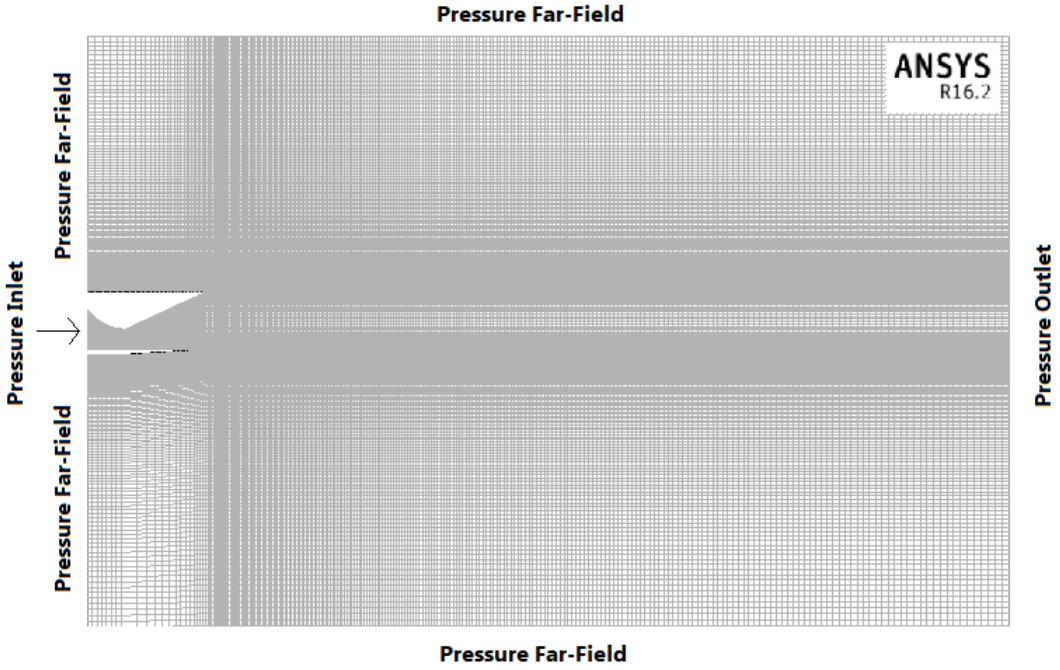

Figure 4.28: Mesh and boundary conditions applied to the numerical simulation domain of the SERN experimental model

The $k - \varepsilon$ RNG turbulence model was used, with the default model constants and standard wall functions. The turbulence intensity and viscosity ratio were kept at their default values, of 5% and 10 respectively.

The density-based solver was used, the energy equation was enabled and the air was set to ideal gas. The implicit formulation and the Roe-FDS flux type were used, with a spatial discretization of Least Squares Cell Based gradient.

In the beginning of the calculation the First Order Upwind scheme was used until a converged initial solution was achieved, and then the Second Order Upwind scheme was applied to the obtained initial solution in order to get more accurate results.

In regard to the solution controls, due to divergence issues, the Courant number and the under-relaxation factor had to be altered in order to achieve a stable convergence during the simulation. This was a very time consuming process, due to it's trial and error nature until suitable values were found.

The standard solution initialization was chosen, starting from the inlet.

During the calculations, the residuals of continuity, velocity in the x and y direction, energy, k and ε were monitored, as well as the surface integral of the static pressure along the SERN's ramp.

The simulations were assumed to be fully converged when the following criteria were met:

1. A drop in residuals of at least 10^{-3};

2. The interest variable being monitored remained constant throughout the iterations;

3. The mass-flow imbalance entering and exiting the domain was below 0.5%.

4.3.3 Comparison Between Experimental and Numerical Results

Fig. 4.29 shows the comparison between the pressure distribution obtained along the SERN's ramp and flap, in the experiment and from the CFD simulation conducted. The pressure values are non-dimensionalised by the ambient pressure and the distances by the height of the throat (ht). The numerical results are in good agreement with the experimental ones, validating the used numerical method. It is also possible to identify the flow's separation points both in the ramp and in the flap, where there is a sudden increase in static pressure.

In Fig. 4.30 it is possible to visually compare the flow fields obtained in CFD with the ones obtained experimentally. The RSS, at NPR = 3, is clearly visible, as well as the separation points and λ shocks (triple points), further proving the validity and accuracy of the numerical simulation. The position of the separation points was measured in the experiment as well as in the CFD simulation, and the values compared. In the experiment separation occurred at a distance of 2.24ht on the ramp, and 1.78ht on the flap. In the CFD simulation separation occurred at a distance of 2.35ht on the ramp, and 1.9ht on the flap. Therefore the is a slight error of 4.91% for the ramp and 6.74% for the flap, which is acceptable. It is also possible

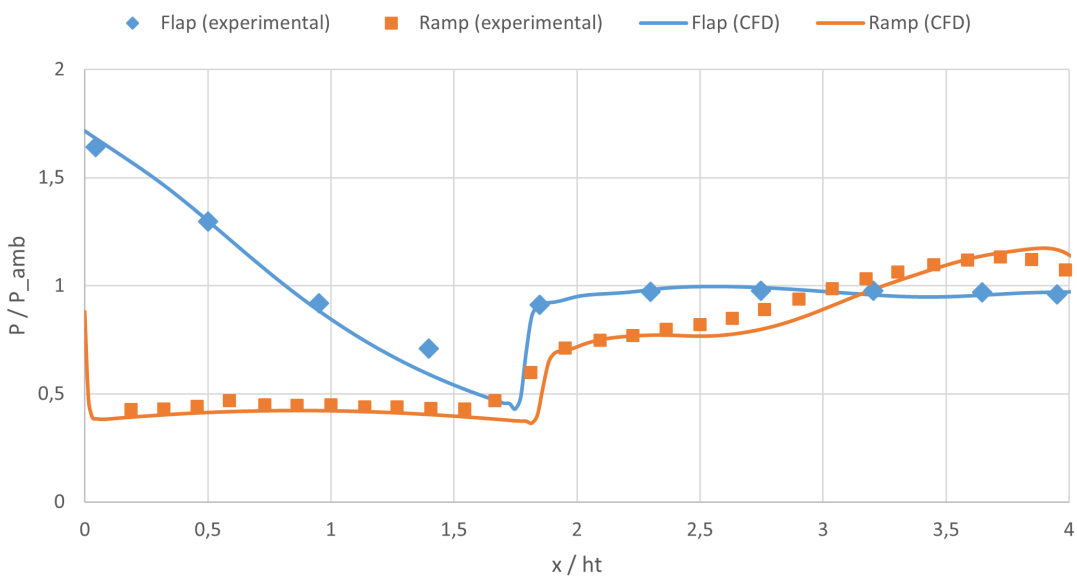

Figure 4.29: Static pressure distribution along the SERN's ramp and flap, obtained experimentally and through CFD

to see the formation of a separation bubble on the ramp, followed by a reattachment of the shock-train, as well as a re-circulation zone towards the end of the flap.

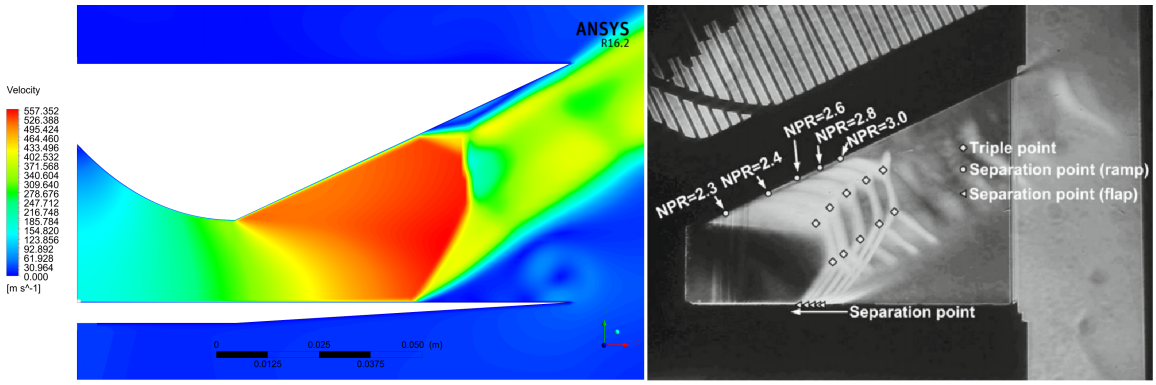

Figure 4.30: Comparison between CFD velocity field and schlieren images, NPR = 3 [8]

4.4 Final SERN Design

4.4.1 Selection of Design / Off-Design Conditions and Study Cases

Finally, using the developed optimisation algorithm, a SERN was designed for possible integration into an hypersonic vehicle.

The design of a hypersonic vehicle is a very complex multidisciplinary task, and this study is focused mainly on the nozzle design aspect. However, in order to design the nozzle, an operating design point must be estimated so the respective flight and atmospheric conditions are known. Thus, the constant dynamic pressure trajectory approach was chosen for the estimation of said design point conditions. It's simplicity and relatively good accuracy provides a

solid starting point for the purposes of this study.

As the vehicle moves through the atmosphere, it creates a dynamic pressure, q_∞, which can be written in terms of Mach number as:

$$q_\infty = \frac{\gamma_\infty p_\infty M_\infty^2}{2} \quad (4.10)$$

where γ_∞, p_∞ and M_∞ are the free-stream specific heat ratio, pressure and Mach number, respectively.

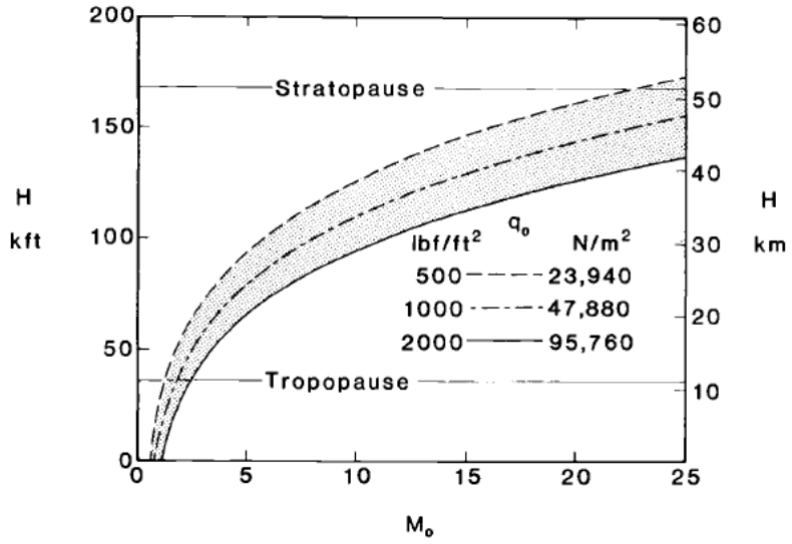

Figure 4.31: Hypersonic operational envelope as a function of flight altitude and Mach number [13]

The dynamic pressure is important in hypersonic vehicle design because the lift and drag of the vehicle are usually a function of q_∞, and it is also closely related to the vehicle's structural limits. If q_∞ is too small, a very large wingspan would be required to generate the lift to sustain the aircraft, and if it is too high the structural forces and drag of the vehicle will also increase. Therefore, hypersonic vehicles must operate within a certain range of dynamic pressure. According to [13], the dynamic pressure values must be approximately between 23940 and 95760 N/m^2. By plotting this interval with the variation of the flight altitude and Mach number, it is possible to visualise the range of operation, as shown in Fig. 4.31.

Taking this into account, the operational design point was chosen to be Mach 4 at an altitude of 22 km, which corresponds to a dynamic pressure of $q_\infty = 45244.16\ N/m^2$.

Furthermore, in order to capture the flow separation and shock-wave patterns that occur when SERN operates in severe over-expanded conditions, a subsonic (Mach 0.4) off-design conditions was chosen at an altitude of 8 km, which simulates part of the process of startup and acceleration.

The operational environments selected for the study are summarised in Tab. 4.4.

Table 4.4: Selected design and off-design ambient conditions

	Free-stream Mach	Altitude (km)	Pressure (Pa)	Temperature (K)
Design (A)	4	22	4039.66	216.69
Off-Design (B)	0.4	8	35687.66	236.27

In both design and off-design environments, the effect of various operating NPR's on the SERN's performance and exhaust flow-fields was investigated.

A total of 13 distinct simulations were conducted:

1. Case A: 5 simulations at the design (A) ambient conditions, with NPR's:
   (a) NPR = 133.65
   (b) NPR = 100
   (c) NPR = 75
   (d) NPR = 50
   (e) NPR = 25
2. Case B: 8 simulations at the off-design (B) ambient conditions, with NPR's:
   (a) NPR = 4
   (b) NPR = 5
   (c) NPR = 6
   (d) NPR = 8
   (e) NPR = 10
   (f) NPR = 12
   (g) NPR = 15
   (h) NPR = 20

4.4.2 SERN Geometry

Fig. 4.32 shows the geometry and characteristics web of the SERN generated by the algorithm, for a design $M_E = 4$ and $\gamma = 1.4$.

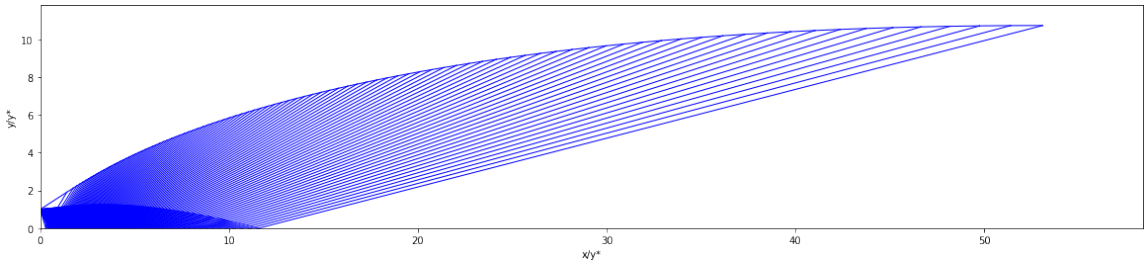

Figure 4.32: SERN contour and characteristics web generated by the algorithm for $M_E = 4$ and $\gamma = 1.4$

The SERN's dimensions are in relation to the throat's height, y^*. The SERN's overall length and height is around $x/y^* = 53.1$ and $y/y^* = 10.7$, respectively, with a flap length of $x/y^* = 11.5$. These large dimensions are justifiable because the algorithm computes the geometry for the complete shock-free expansion of the nozzle flow.

However, this geometry is too large to integrate into the vehicle, for reasons mentioned previously. Therefore, a truncation will be applied to the nozzle ramp, at approximately 40% of its length, reducing it from $x/y^* = 53.1$ to $x/y^* = 31.9$. The nozzle height will also decrease from $y/y^* = 10.7$ to $y/y^* = 9.8$. The length of the flap will not be altered.

The stream thrust function allows to determine the thrust loss by truncating the nozzle, and is given by:

$$\frac{Sa_x - Sa_i}{Sa_E - Sa_i} = \frac{\frac{1+\gamma M_x^2}{M_x\sqrt{1+\frac{\gamma-1}{2}M_x^2}} - \frac{1+\gamma M_i^2}{M_i\sqrt{1+\frac{\gamma-1}{2}M_i^2}}}{\frac{1+\gamma M_E^2}{M_E\sqrt{1+\frac{\gamma-1}{2}M_E^2}} - \frac{1+\gamma M_i^2}{M_i\sqrt{1+\frac{\gamma-1}{2}M_i^2}}} \tag{4.11}$$

where M_i is the Mach number at the nozzle inlet, considered 1 in this study, M_E is the design nozzle exit Mach number, which is 4 in this case, and M_x is the predicted exit Mach number after the truncation, which can be obtained through the nozzle area ratio A/A^* after the truncation.

The thrust loss predicted is about 1.69% for this case. The thrust loss is negligible because the majority of the thrust is generated by the early expansion in the region closer to the nozzle throat.

Then, a boundary layer correction was applied to the geometry, offsetting all the points of the nozzle wall a certain distance δ outward.

After the truncation and the viscous effects correction, the SERN's final length and height are $x/y^* = 31.9$ and $y/y^* = 10.12$, respectively, with a flap length of $x/y* = 11.5$, and a design $NPR = 133.65$. This geometry can be seen in Fig. 4.33.

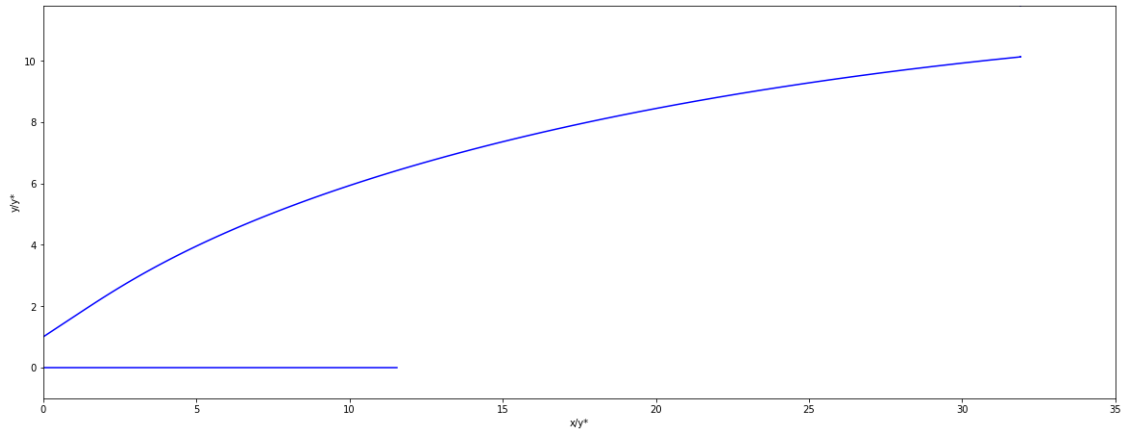

Figure 4.33: Final SERN geometry

4.4.3 Numerical Simulation Framework

The final SERN geometry was then imported into CATIA V5, were the geometry of the domain to be used in the numerical simulations was created. The height of the throat was chosen to be 100 mm. Then the CAD file was imported to FLUENT, where a sized structured mesh was generated.

The mesh has a minimum orthogonal quality of 0.83 and a maximum orthogonal skewness of 0.16, which is quite good. In order to fully capture the flow phenomena inside and downstream of the SERN, the mesh was refined in these regions, and was coarsened towards the domain's boundaries to save computational resources and simulation time.

The mesh and the boundary conditions applied to the domain can be seen in Fig. 4.34. The total domain's height and length are about 6 and 15 times the SERN's exit height, respectively, which minimise the influence of the far-field boundaries. The boundaries of the SERN's geometry were set as walls. In each of the various simulations conducted, both in the design and off-design ambient conditions, the values at the far-field and pressure outlet boundaries were kept constant, while the nozzle inlet pressure was changed.

The numerical models, solution methods, controls and initialization, as well as the convergence criteria used were the same as in the numerical simulation of the experiment.

4.4.3.1 Mesh Independence Study

In order to verify the results obtained were not dependent of the mesh resolution being used, a mesh independence study was conducted for the Case B, NPR = 4. This case presented fairly complex flow phenomena, and thus it was assumed that if the mesh used provided good results for this case, it could also be applied to the remaining cases.

The following grids were tested:

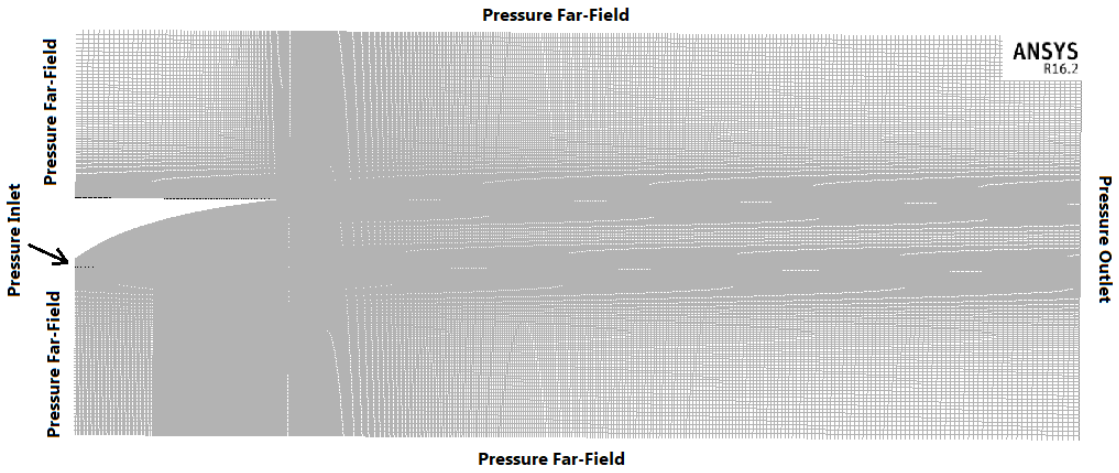

Figure 4.34: Mesh and boundary conditions applied to the numerical simulation domain

1. Coarse (47440 elements);

2. Medium (115360 elements);

3. Fine (426960 elements).

Firstly the coarse grid was generated, then a medium grid with twice number of edge divisions was created. Finally, a fine grid with 1.5 times the number of edge divisions of the medium was generated. Simulations with the each of the 3 grids were then conducted, and the static pressure along the SERN's ramp and flap was measured and compared, as shown in the plots of Fig. 4.35. The pressure values are non-dimensionalised by the ambient pressure and the distances by the height of the throat.

From the comparison of the results obtained by the three grids tested, it can be observed that there is a noticeable difference between the coarse grid with respect to the medium and fine grids. However, between these two, the variation of static pressure values is a lot less significant. Despite the slight difference, the mesh resolution of the medium grid was assumed to be sufficient, and selected for the remaining tests, since it provided good enough results, with almost half of the computational time required to run simulations on the fine grid.

4.4.3.2 y^+ Values

When using wall functions to solve the near-wall regions, it is important to ensure the y^+ values are within the 30-300 range recommended by FLUENT, thus guarantying these regions are being correctly modelled and the solution is accurate. After each simulation, the y^+ values along the ramp and flap of the SERN where checked, and the mesh was adapted accordingly if required.

Fig. 4.36 show the distribution of the y^+ values along the SERN's walls for Case B, NPR = 4, which vary to a large degree due to the complex flow phenomena but are within the

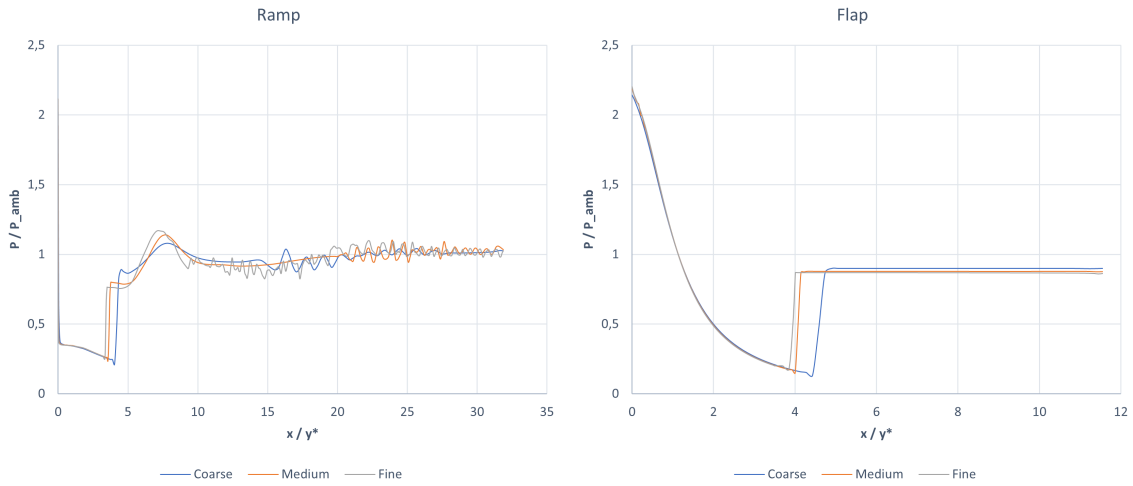

Figure 4.35: Static pressure distribution along the SERN's ramp and flap for coarse, medium and fine grids

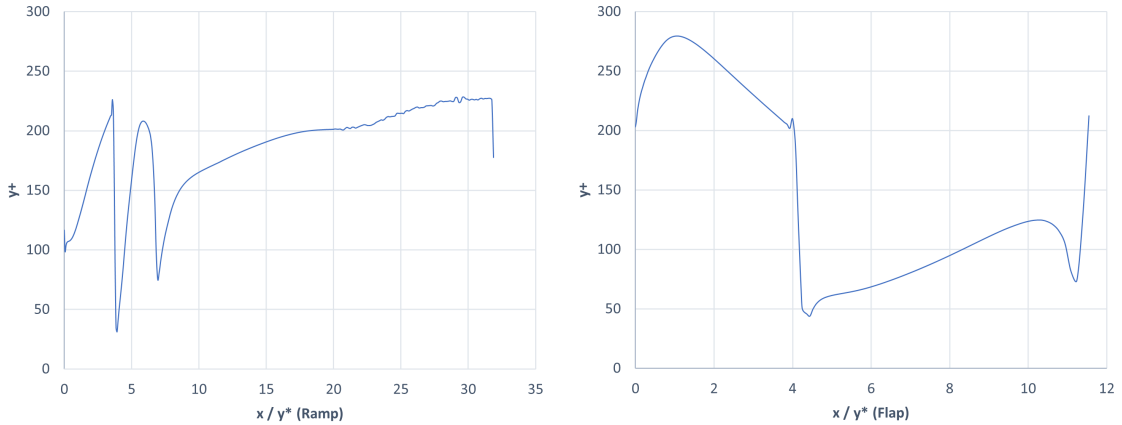

Figure 4.36: y^+ values distribution along the SERN's ramp and flap for Case B, NPR = 4

recommended range of values required for the use of wall functions.

Chapter 5

Results

5.1 Case A

In this case study, the domain's boundary condition were set to simulate the SERN operation at cruise conditions. While the ambient conditions were kept constant at an altitude of 22 km and a free-stream of Mach 4, the nozzle inlet pressure was decreased from the design NPR = 133.65 to 100, 75, 50 and 25.

5.1.1 Mach Number Contours

Fig. 5.1 show the Mach number contour of the SERN operating at the design conditions and NPR = 133.654. At these conditions, the SERN achieve near perfect expansion of the gases to the ambient pressure, and the absence of strong oblique shock-waves or expansion waves in the exhaust plume can be observed. Due to the interaction between the exhaust plume and the free-stream the is a formation of a viscous shear layer emanating from the trailing edge of the SERN's ramp and flap, which is also visible.

In Fig. 5.2 the ambient conditions remained the same, but the NPR was reduced to 100. Now, the SERN is operating at an off-design condition, and since the pressure at the SERN's exit is lower than the ambient pressure, the flow is over-expanded.

From the interaction between the exhaust and the external flow, there is a formation of incident shock-waves at the nozzle exit, reflected shock-waves further downstream as well as the formation of a viscous shear layer, which are all revealed in the Mach number contours.

Reducing the NPR even further will lead to an intensification of the state of over-expansion, with the formation of stronger incident and reflected shock-waves which lead to a reduction of the flow speed, as well as a contraction of the whole exhaust plume due to the pressure difference. These phenomena can be observed in Figs. 5.3 - 5.5, where the NPR is decreased to 75, 50 and 25.

5.1.2 Static Pressure Distribution

In Fig. 5.6 the static pressure distribution along the SERN's ramp and flap for all the NPR's tested in Case A are shown, with the pressure values non-dimensionalised by the ambient pressure and the length by the height of the throat.

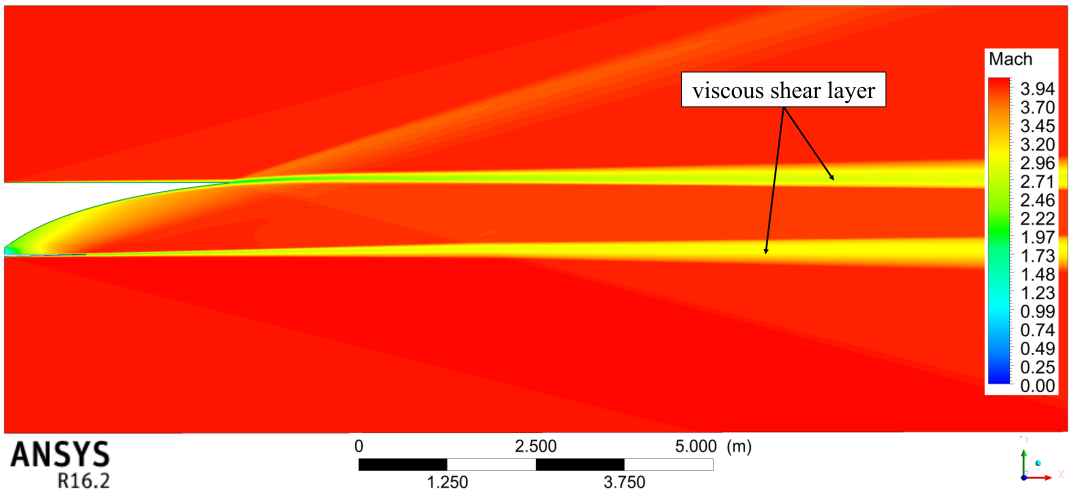

Figure 5.1: Mach number contour for Case A, NPR = 133.654

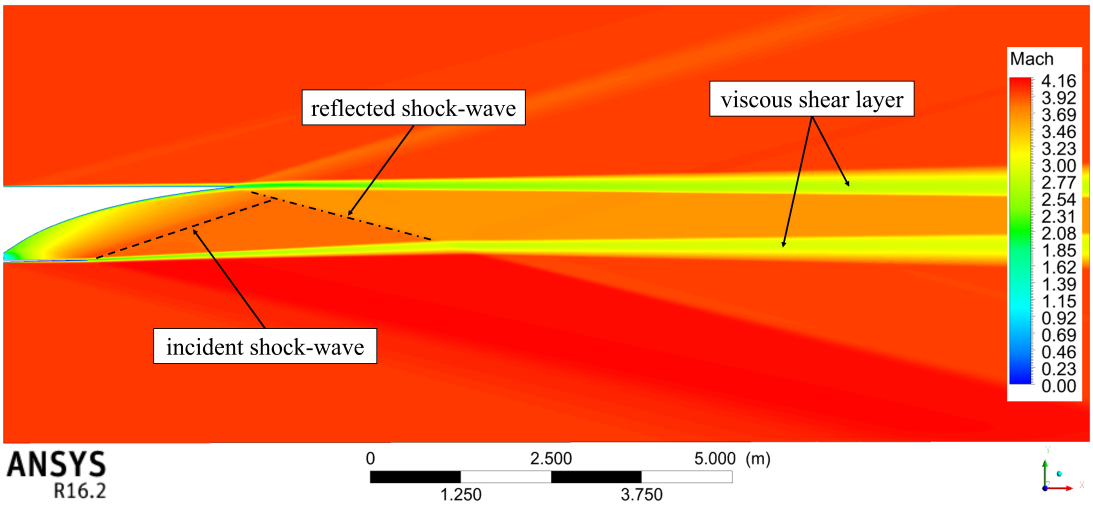

Figure 5.2: Mach number contour for Case A, NPR = 100

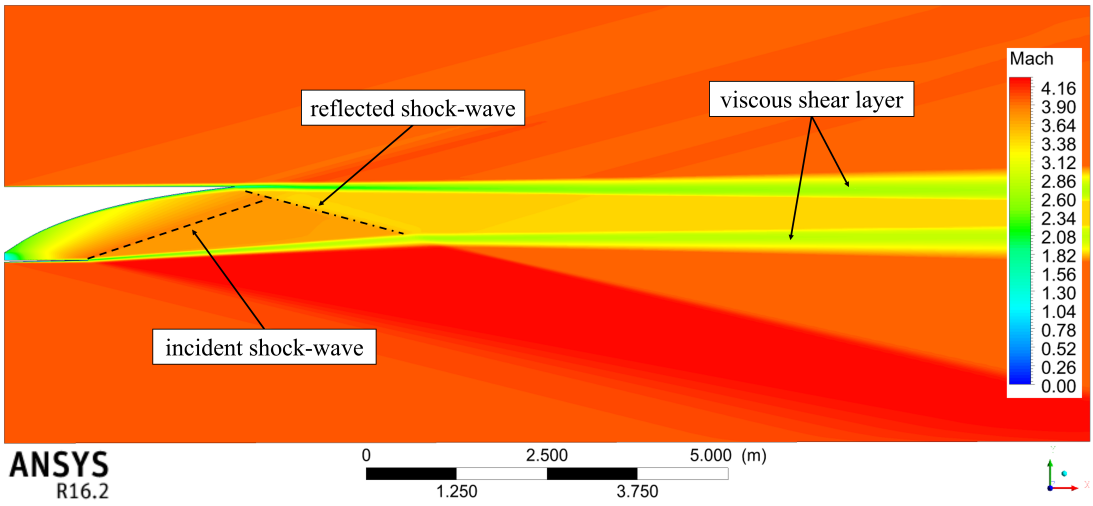

Figure 5.3: Mach number contour for Case A, NPR = 75

Since in the simulations in this case there is no flow separation or complex shock-wave phenomena occurring inside the nozzle, the pressure drop along its walls is quite smooth, in

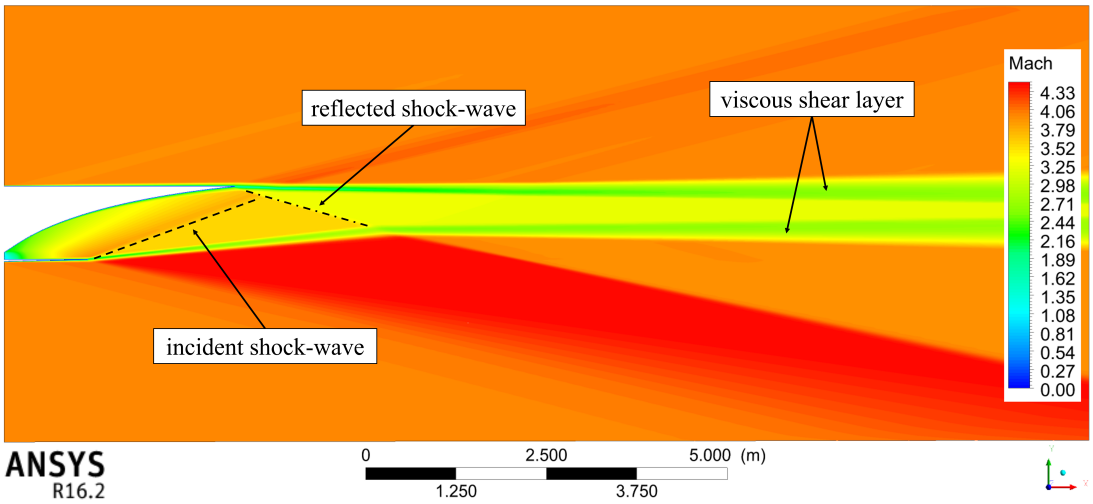

Figure 5.4: Mach number contour for Case A, NPR = 50

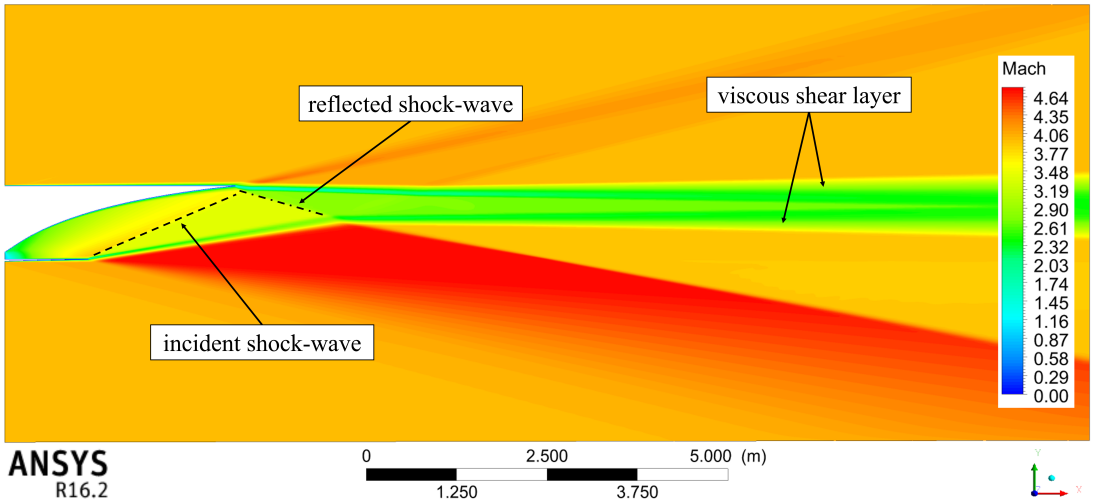

Figure 5.5: Mach number contour for Case A, NPR = 25

accordance with isentropic flow expansion.

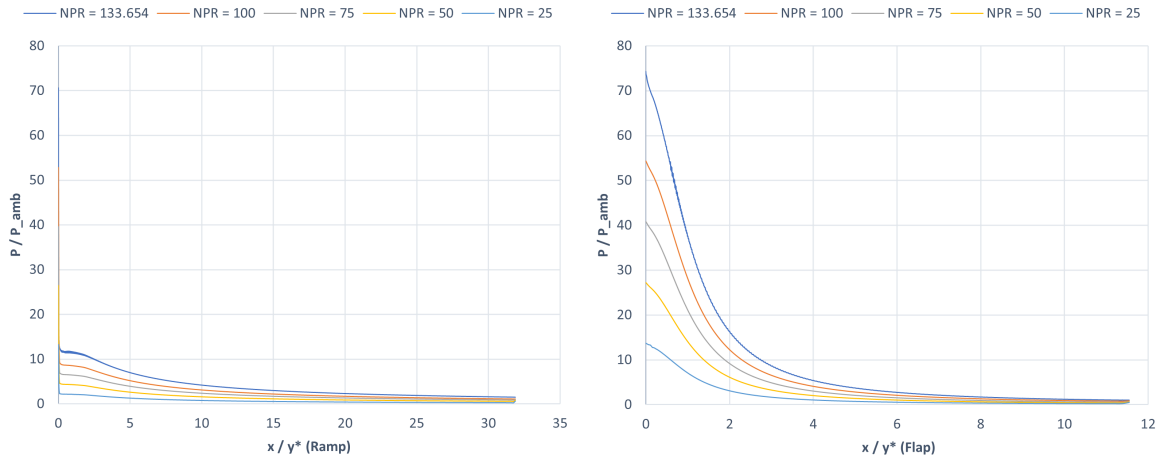

Figure 5.6: Static pressure distribution along SERN's ramp and flap for Case A

5.1.3 SERN's Performance

In order to evaluate the SERN's performance through the various NPR's three main parameters were selected: the thrust, the lift and the moments generated by the SERN. The thrust is calculated by the ramp and flap wall pressure and shear stress integration, projected on the x axis. The lift is calculated in a similar manner, but by projecting them on the y axis. The moment caused by these forces is calculated on the intersection point of the throat and the flap.

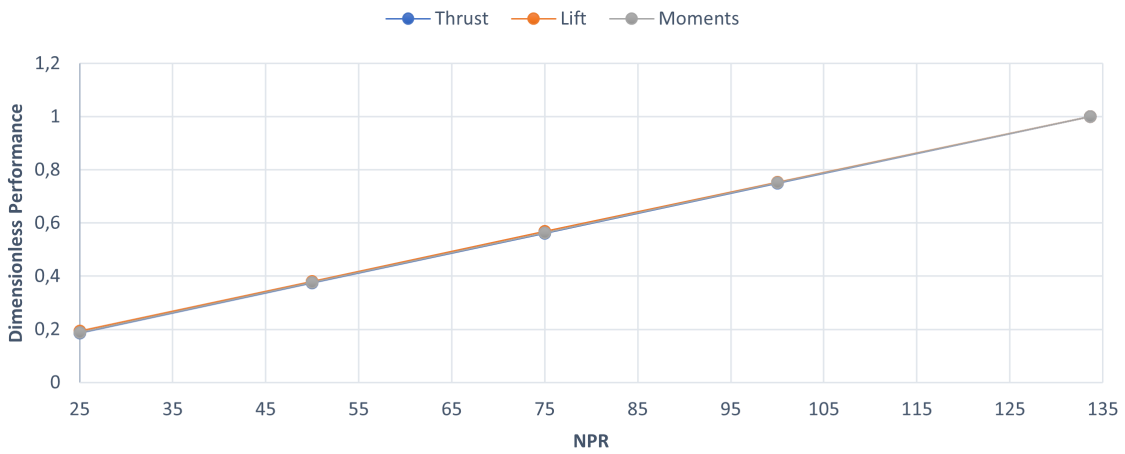

Figure 5.7: SERN's dimensionless performance for Case A

Fig. 5.7 shows the change in dimensionless performance parameters for the various NPR's tested. Thrust, lift and moment are non-dimensionalised by the values of the design point NPR = 133.654. All the three parameters follow a linear variation of roughly the same magnitude, with a reduction of 81.33% of thrust, 80.7% of lift and 81.17% of moments from NPR's 133.654 to 25.

5.2 Case B

In this case study, the domain's boundary conditions were set to simulate the SERN operation during an off-design phase, such as startup and acceleration. Thus, while the ambient conditions were kept constant at an altitude of 8 km at a subsonic free-stream of 0.4 Mach, the nozzle inlet pressure was increased from NPR = 4, 5, 6, 8, 10, 12, 15 to 20.

It is also during this low speed off-design operation that the most complex flow phenomena and shock-wave patterns occur within the SERN. Under these severe over-expanded conditions, subsonic regions such as subsonic boundary layers, re-circulation zones and separation bubbles can appear in the SERN, and the external flow has some influence on these phenomena and the overall shock-wave structure that form.

5.2.1 Velocity Streamlines and Shock-Wave Patterns

Figs. 5.8 through 5.15 show a closeup of the velocity streamlines near the SERN for the various NPR's simulated in Case B, and are very useful to understand and visualise the flow phenomena occurring in this region.

The ramp RSS pattern mentioned in a previous chapter is clearly visible in various NPR's simulated in this case.

In this separation pattern there is separation of the main jet flow both on the SERN's ramp and flap, followed by a reattachment to the ramp further downstream of the separation point. Between the ramp's separation and reattachment points there is a formation of an separation bubble of recirculating trapped air. Furthermore, since there is no flow reattachment on the flap downstream of the separation point, a large re-circulation zone appears, where the pressure almost matches the ambient pressure.

The shock-wave structures caused by the severe over-expansion are also clearly visible, with the formation of a normal shock-wave (Mach disk) between two λ shock structures (also known as triple points), which result from the interaction of the two separation shock-waves from the ramp and flap, as well as the respective reflected shocks. Downstream of these shock structures the waves intersect and reflect, interacting with the shearing layer, which results in a shock train formed by compression and expansion waves.

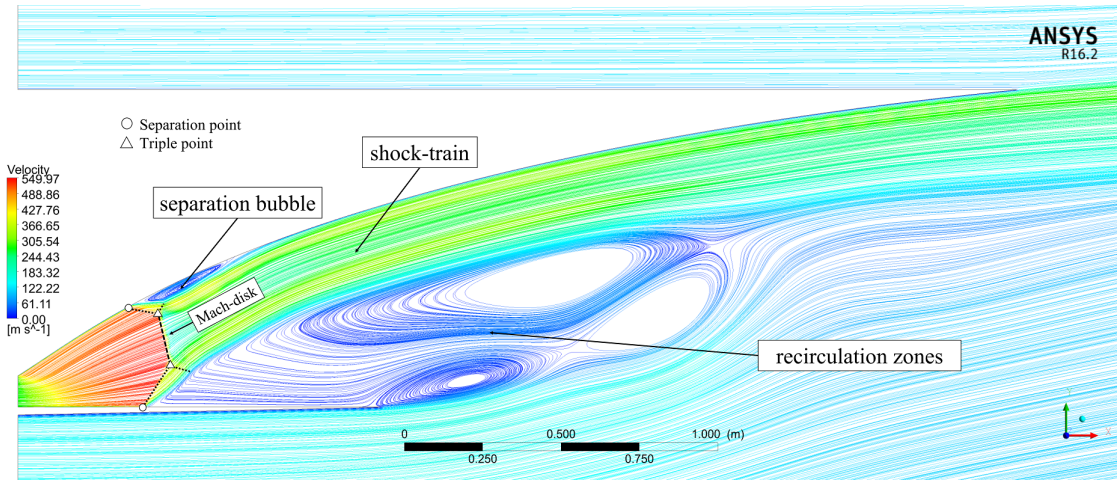

Figure 5.8: Velocity streamlines for Case B, NPR = 4

As the NPR increases, the separation points both on ramp and flap move further downstream, and with them the separation bubble on the ramp. Accordingly, the re-circulation region on the flap also becomes increasingly smaller as the main jet takes up more space inside the SERN. For NPR = 10 this re-circulation zone still appears, however a lot smaller compared to the lower initial NPR's. NPR = 12 the separation bubble on the ramp is still present, but the separation point on the flap and the re-circulation zone cease to exit.

Moreover, with the increase in NPR the separation shock waves become weaker and the Mach

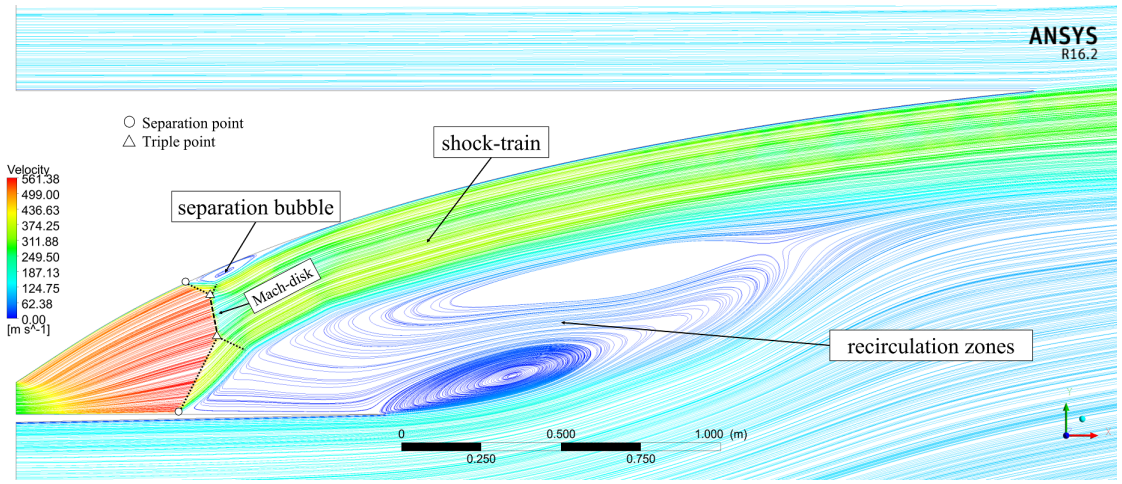

Figure 5.9: Velocity streamlines for Case B, NPR = 5

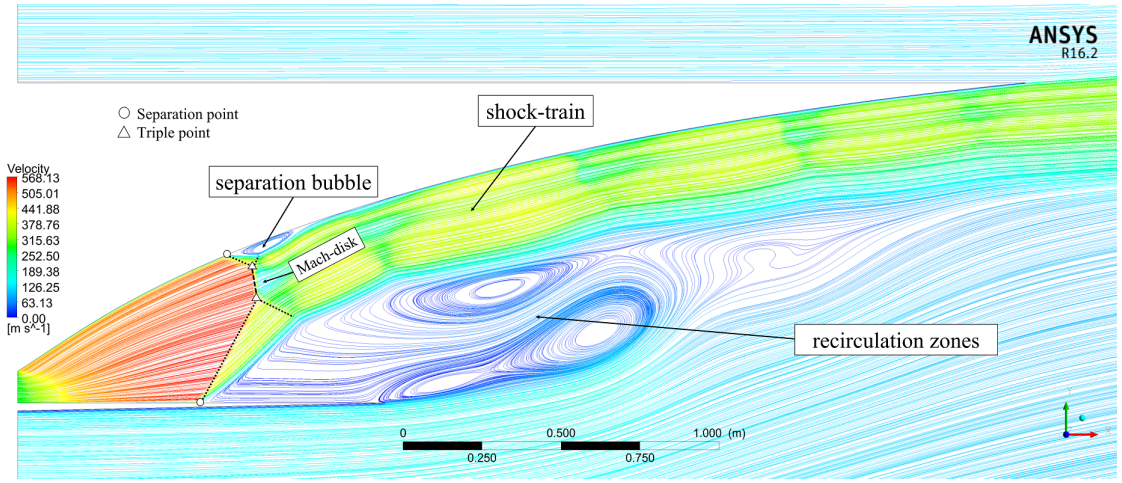

Figure 5.10: Velocity streamlines for Case B, NPR = 6

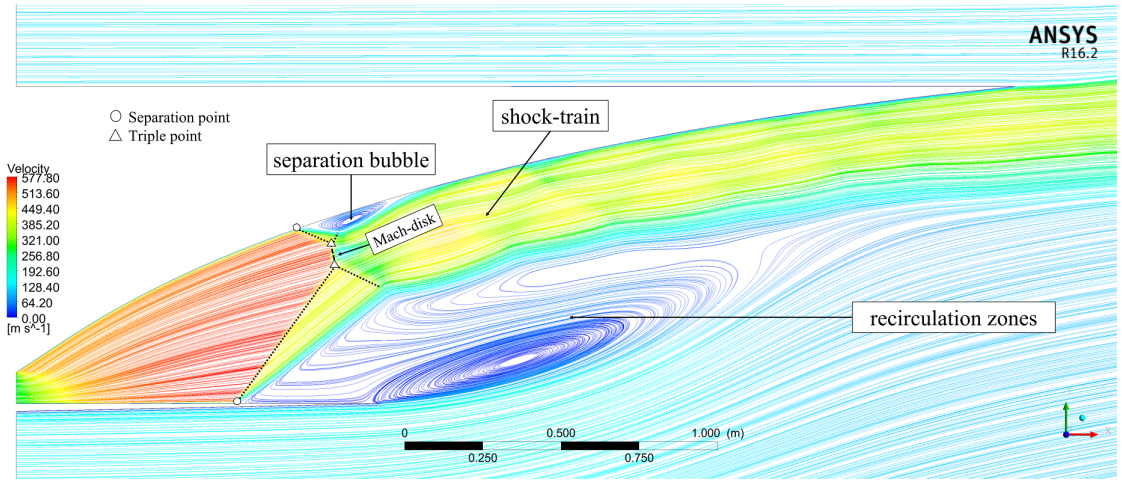

Figure 5.11: Velocity streamlines for Case B, NPR = 8

disk begins to get smaller until almost disappears. In NPR's 4, 5 and 6 the Mach disk is clearly visible, but starts to shrink as the NPR increases and is no longer visible in NPR's 15 and 20. It is also visible that the shock train intensity also increases with the NPR.

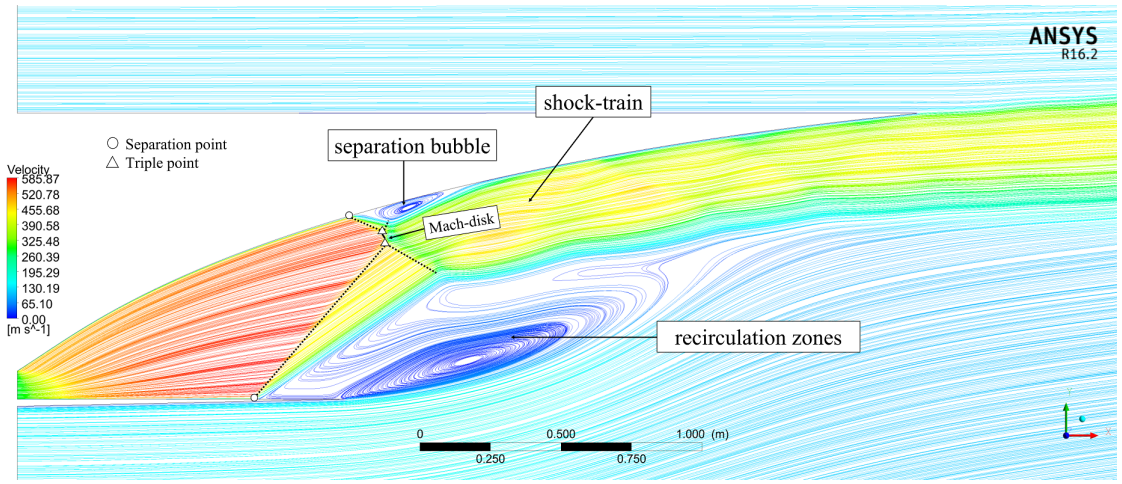

Figure 5.12: Velocity streamlines for Case B, NPR = 10

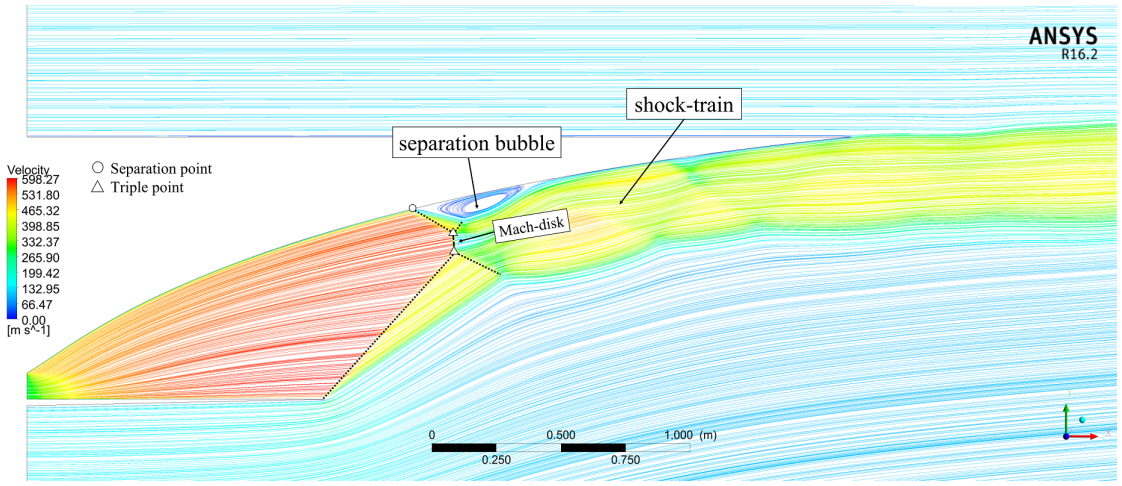

Figure 5.13: Velocity streamlines for Case B, NPR = 12

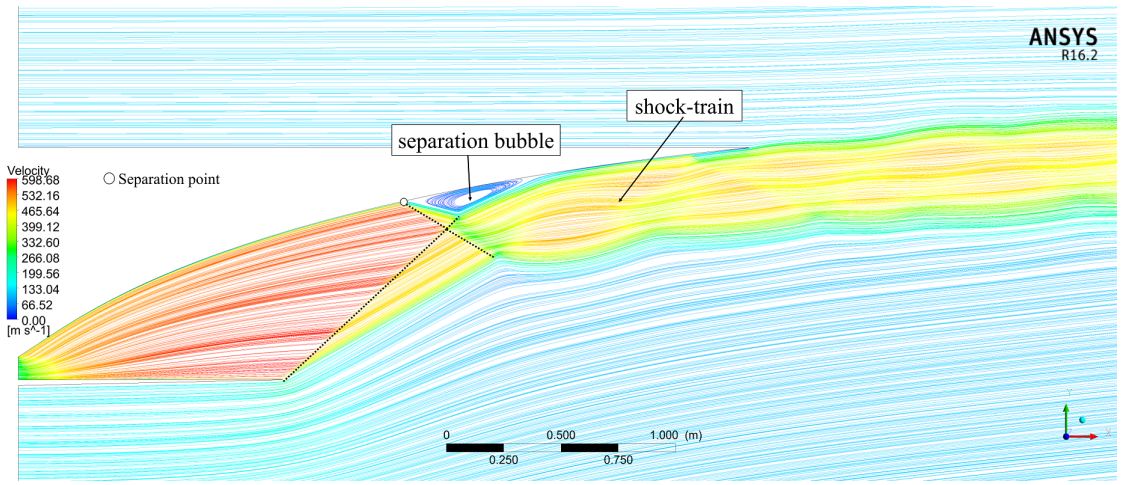

Figure 5.14: Velocity streamlines for Case B, NPR = 15

5.2.2 Static Pressure Contours and Distribution

Figs. 5.16 through 5.23 show the pressure contours for the various NPR's simulated in Case B. Just as in the velocity streamlines, it is possible to visualise the flow separation points, as

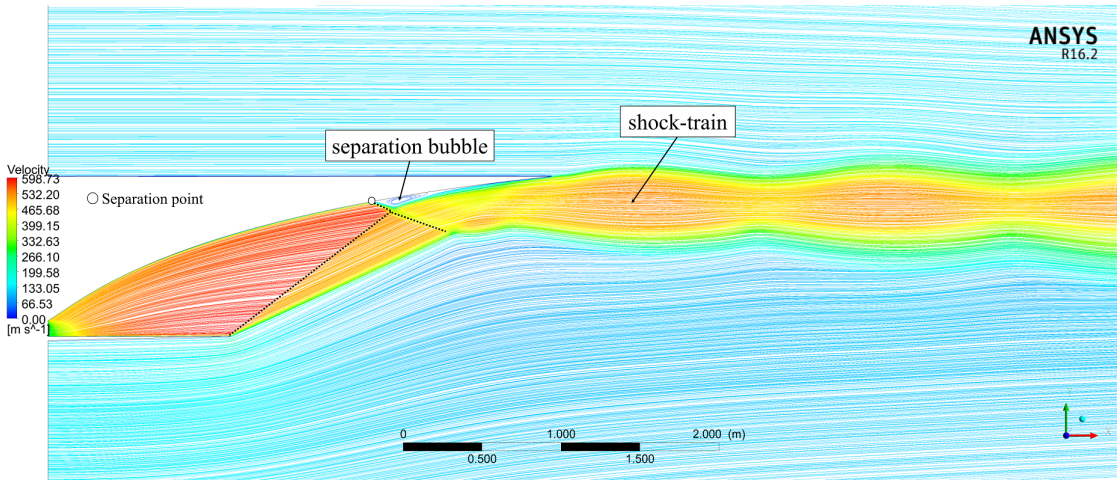

Figure 5.15: Velocity streamlines for Case B, NPR = 20

well as the formation of the Mach disk in lower NPR's. It is also noticeable that the shock-train progressively intensifies with higher NPR's.

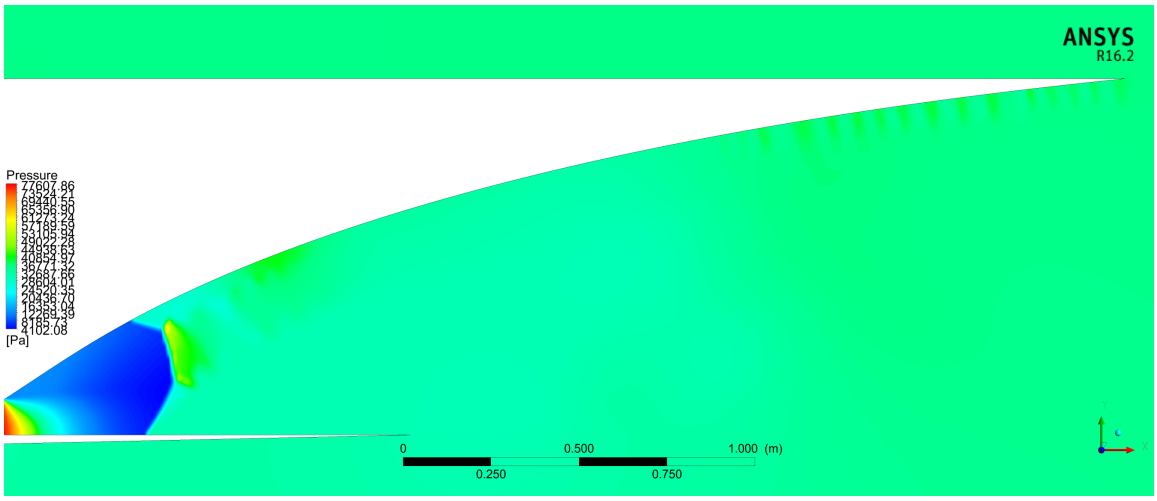

Figure 5.16: Pressure contours for Case B, NPR = 4

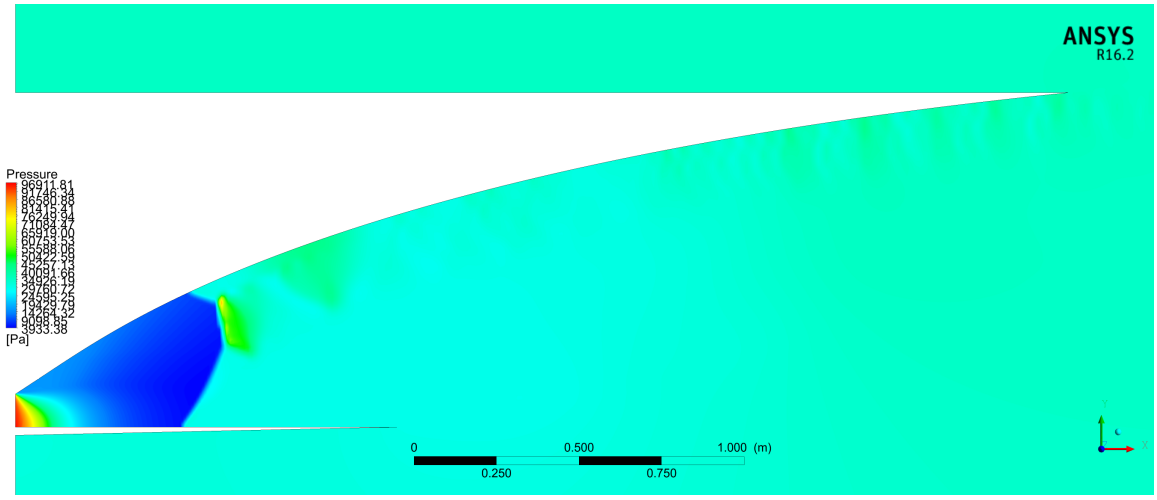

Figure 5.17: Pressure contours for Case B, NPR = 5

The plots in Fig. 5.24 and 5.25 show the distribution of static pressure along the SERN's

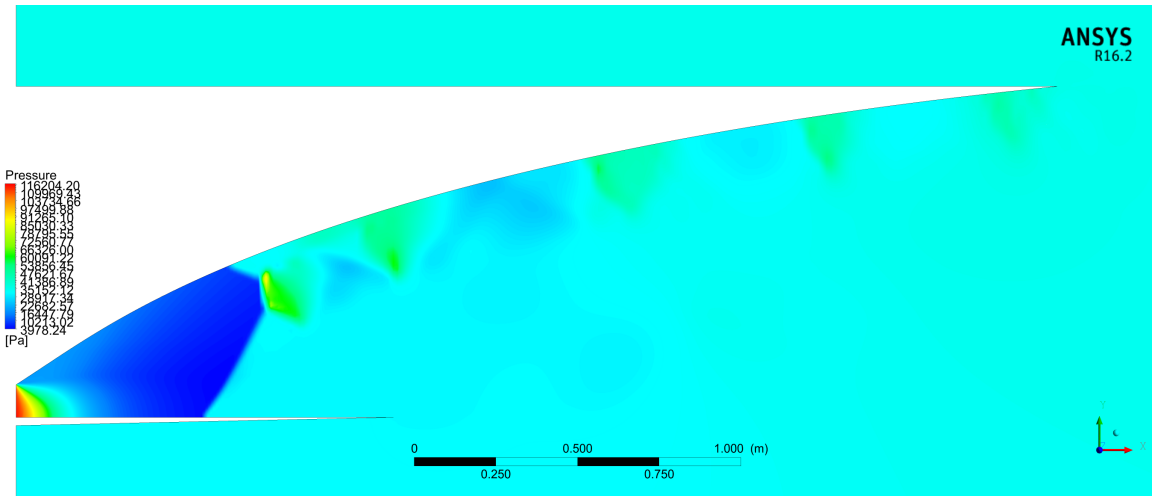

Figure 5.18: Pressure contours for Case B, NPR = 6

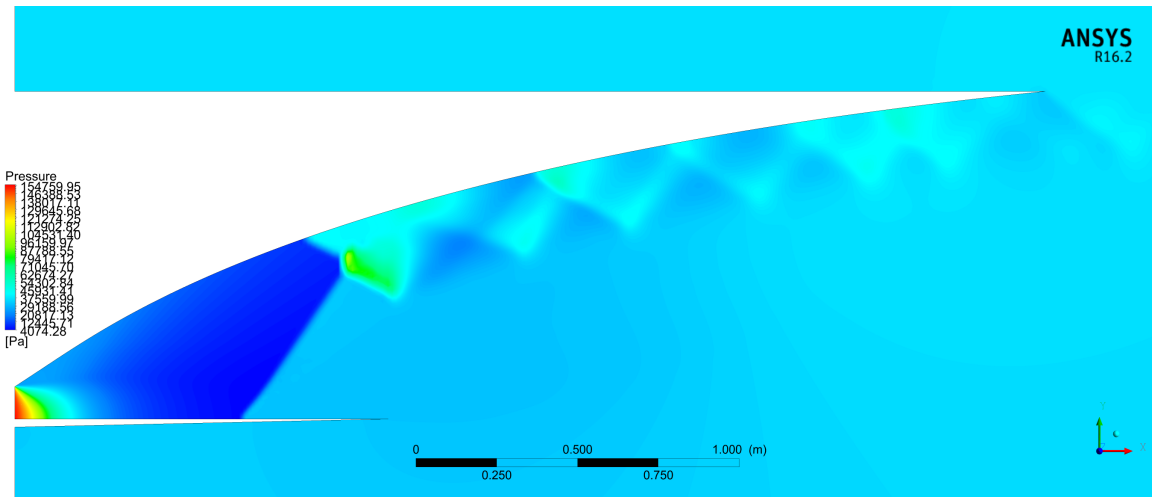

Figure 5.19: Pressure contours for Case B, NPR = 8

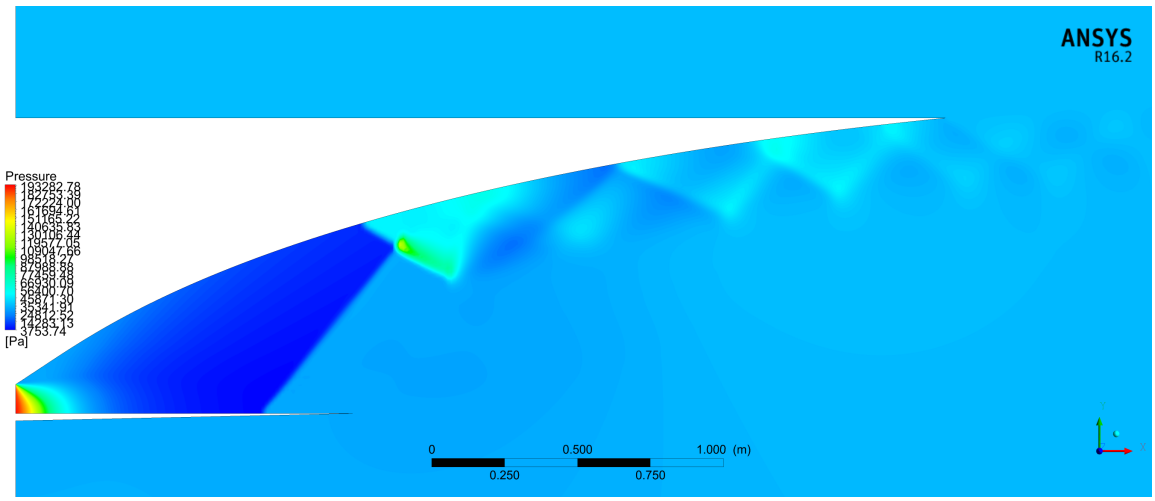

Figure 5.20: Pressure contours for Case B, NPR = 10

ramp and flap, respectively, for all the NPR's tested in Case B. The pressure values are non-dimensionalised by the ambient pressure, and the length by the height of the throat.

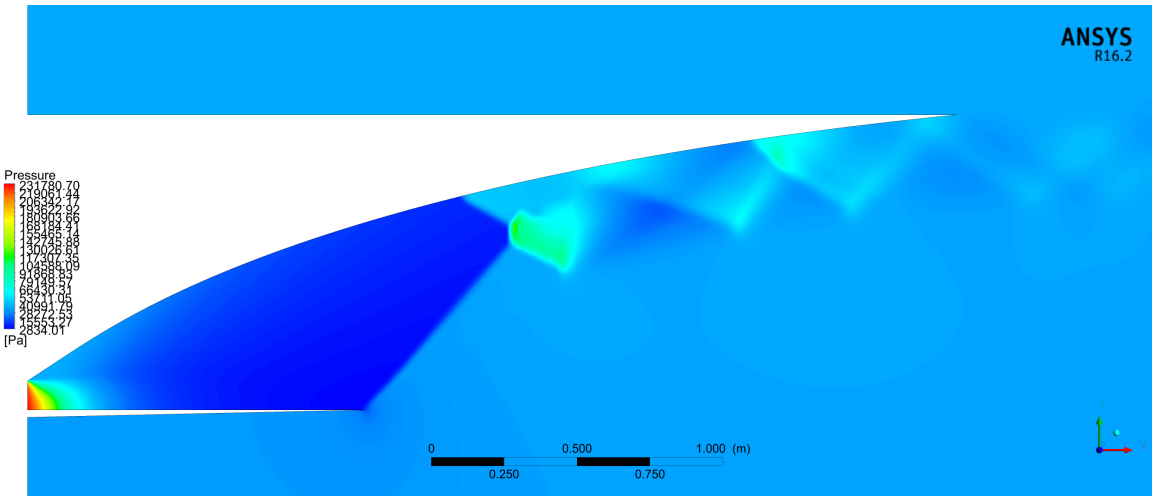

Figure 5.21: Pressure contours for Case B, NPR = 12

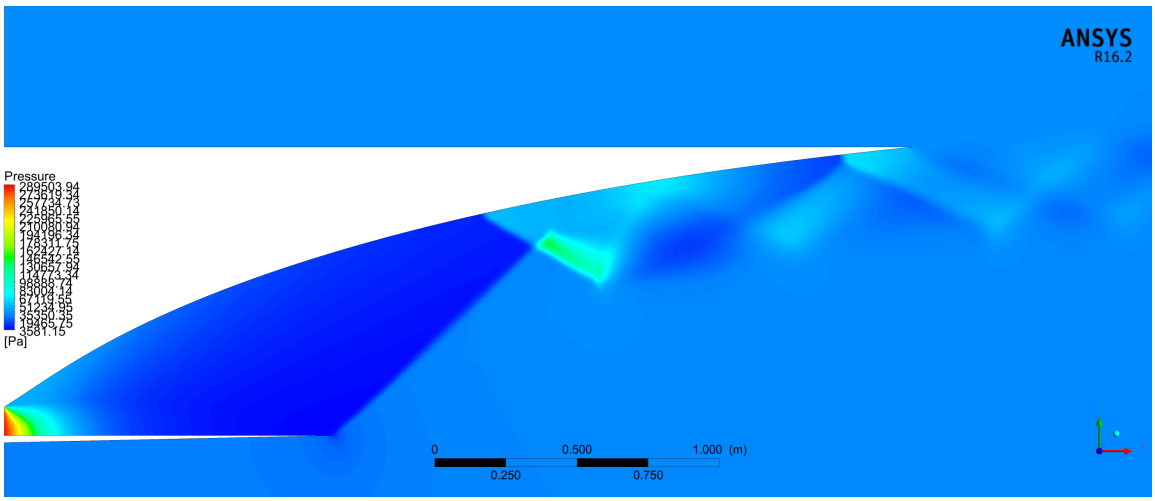

Figure 5.22: Pressure contours for Case B, NPR = 15

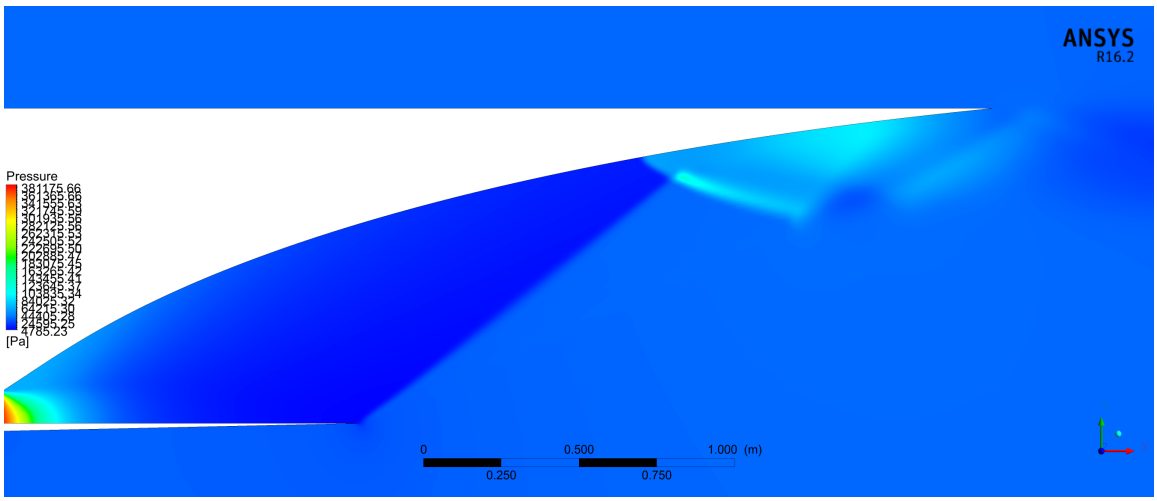

Figure 5.23: Pressure contours for Case B, NPR = 20

From their analysis, it is possible to identify the flow separation points, which correspond to the first sudden increase in static pressure. It is also noticeable that the higher the NPR, the

further downstream the separation occurs, in accordance with the velocity streamlines and pressure contours.

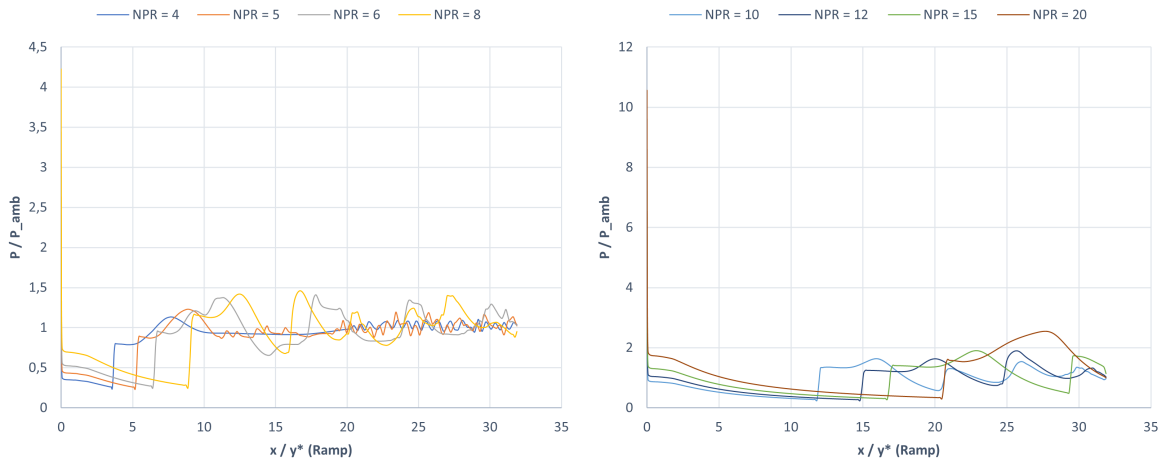

Figure 5.24: Static pressure distribution along SERN's ramp for Case B

In the SERN's ramp, downstream of the separation point and bubble, the static pressure varies to some degree due to the presence and reattachment of the shock-train to the ramp's surface. This pressure variation can also be visualised in the pressure contours.

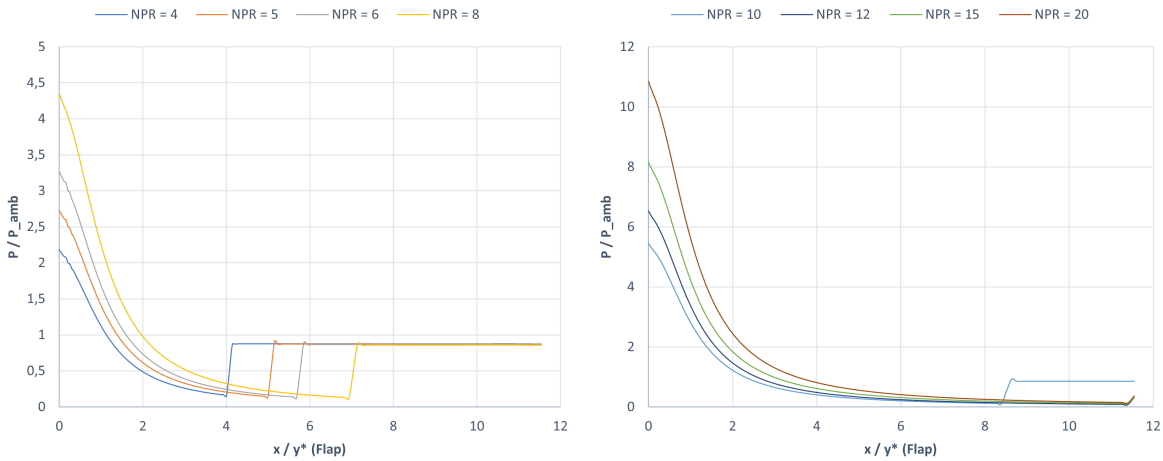

Figure 5.25: Static pressure distribution along SERN's flap for Case B

Meanwhile, in the SERN's flap downstream of the separation point, the static pressure remains fairly constant and slightly lower than the ambient pressure in this re-circulation region. Furthermore, since there is no flow separation on the flap for NPR's 12, 15 and 20, there is no sudden increase in static pressure visible.

5.2.3 SERN's Performance

Fig. 5.26 shows the evolution of the SERN's dimensionless performance for the various NPR's tested in Case B. Thrust, lift and moments are non-dimensionalised by the values of NPR = 4.

As the NPR increases from 4 to 5, there is a slight decrease in thrust, followed by an continu-

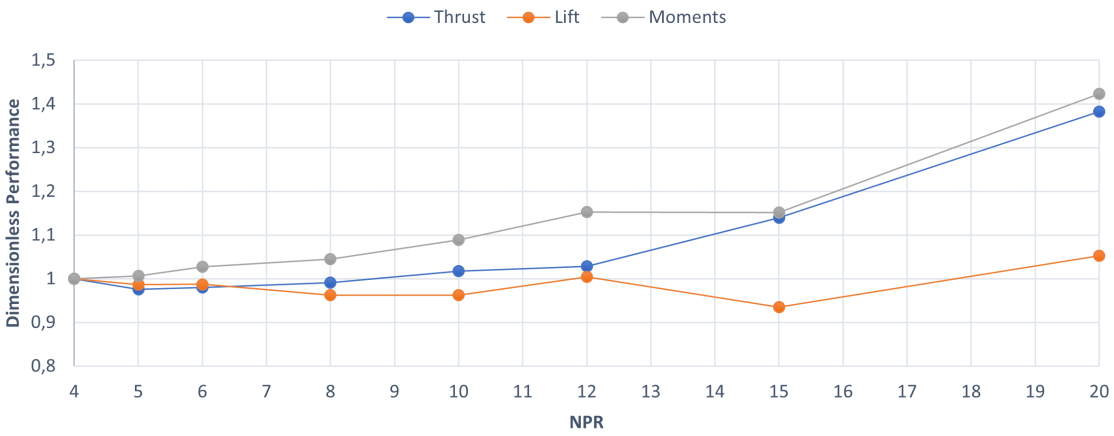

Figure 5.26: SERN's dimensionless performance for Case B

ous increase up to NPR = 20. The lift decrases up to NPR = 10, with a slight increase in NPR = 12 before reaching its lowest point at NPR = 15, where it begins increasing again up to NPR = 20. The moments increase through all the NPR range, remaining almost constant between NPR's 12 and 15. Overall, from NPR = 4 to 20, there is a 38.2% increase in thrust, a 5.27% increase in lift and a 42.3% increase in moments.

Chapter 6

Conclusion

A Single Expansion Ramp Nozzle (SERN) was designed and investigated.

Firstly a Python algorithm based on the method of characteristics (MOC) was developed, which computes the optimised ideal contour for a two-dimensional supersonic shock-free nozzle, more specifically a minimum length nozzle (MLN). Based on the input values of the desired Mach number at the nozzle exit M_E, the specific heat ratio γ at which the nozzle operates and the desired number of characteristic lines n to be used in the computation, the algorithm calculates various flow-field properties (such as Mach number, pressure, temperature and density) at a series of data points within the nozzle and traces the nozzle wall contour required for ideal shock-free isentropic expansion of the gases. The flow-field properties calculated showed good agreement with the theoretical notions reviewed previously regarding compressible flow.

Various nozzle contours were generated and compared, with different combinations of input values to evaluate their influence on the nozzle geometry, which revealed to be highly influenced by the exit Mach number and specific heat ratio chosen. Moreover, the geometry remained practically unchanged when the number of characteristics used in the calculations was higher than 100. Furthermore, since the MOC assumes the flow to be inviscid, a simple boundary layer correction subroutine was added to the algorithm, which offsets the generated inviscid contour a certain distance to account for the viscous effects. Comparison of the algorithm results with theoretical notions, previous literature and simple CFD simulations proved the validity of the code, as well as its robustness in generating optimised MLN contours.

The developed algorithm was then employed to design the optimised geometry of a SERN, which is a particular type of asymmetric nozzle with several advantages for high Mach and hypersonic applications. The chosen operating exit Mach number and specific heat ratio were $M_E = 4$ and $\gamma = 1.4$. The optimal geometry generated by the algorithm for these values is too large for viable integration into a vehicle, thus was truncated at 40% of its length, without significant loss in generated thrust.

A numerical framework was created in ANSYS FLUENT 16.2, replicating and simulating the conditions of an experimental investigation conducted on a SERN by other authors. The CFD results showed good agreement with the experimental ones, validating the numerical model employed. Then, a similar numerical framework was applied to the designed SERN,

where several case studies were conducted simulating design and off-design operating conditions. All the numerical simulations were solved in a steady-state 2D environment, using the density-based solver and the $k - \varepsilon$ RNG turbulence model.

Case A simulates the SERN operating at the design altitude (22 km) and speed (Mach 4). The NPR was decreased from the design value of 133.65 to 100, 75, 50 and 25. At the design condition, it was observed that the SERN achieved near perfect expansion of the gases, with the absence of strong oblique shock-waves or expansion waves in the exhaust plume. The formation of a viscous shear layer between the exhaust plume and the free-stream was observed. When the NPR was reduced, the SERN began operating in an over-expanded condition, leading to the formation of incident shock-waves at the nozzle exit and reflected shock-waves further downstream, a reduction of exhaust flow speed, contraction of the exhaust plume, and formation the viscous shear layer observed previously. Pressure drop along the walls occurred smoothly since no flow separation or complex shock-wave phenomena occur within the SERN. From NPR = 133.65 to NPR = 25, the SERN's thrust, lift and moments suffered a linear reduction of 81.33%, 80.7% and 81.17% respectively.

Case B simulates the SERN operating at low speed (Mach 0.4) and low altitude (8 km) off-design conditions, such as the process of startup and acceleration, which leads to severe over-expanded flow and complex shock-wave patterns. The NPR was increased from 4 to 5, 6, 8, 10, 12, 15 and 20. The ramp RSS pattern is clearly visible, with the separation and reattachment of the main jet to the SERN's ramp, and the formation of a separation bubble for the whole NPR range tested. For NPR's 4 through 10, a large re-circulation region appears downstream of the flap separation point, which disappears as the NPR increases further. The separation points both on the ramp and flap moved downstream as the NPR increased. Mach disks, λ shock structures and downstream shock-trains composed of compression and expansion waves were also observed, as well as the formation of a viscous shear layer between the main jet and free-stream. As the NPR increased, the λ shocks and Mach disks became progressively weaker until no longer visible, opposed to the downstream shock-train which became stronger. The pressure distribution along the SERN's ramp and flap also reveals the location of the separation points, as well as the presence and reattachment of the shock-train. Between NPR = 4 to NPR = 20, the SERN's thrust, lift and moments varied to some degree, with an overall increase of 38.2%, 5.27% and 42.3% respectively.

6.1 Limitations and Future Work

During the present research thesis, some assumptions and simplifications were employed, and thus there is still room for improvement.

Regarding the algorithm developed, the nozzle flow is assumed to be calorically perfect, which means the specific heat capacity, γ, is a constant value. However in reality, at high enough temperatures the γ may begin to vary to some degree, an the gas is said to be calori-

cally imperfect. Thus, including a variable temperature dependant γ in the algorithm would be a great improvement to the code, making it more accurate.

Moreover, the flow at the nozzle inlet is assumed to be at sonic conditions (choked flow) which is valid for the present study. However, for some hypersonic vehicles operating at higher speeds, it may be required that the flow remains supersonic through the combustion and $M > 1$ when entering the nozzle inlet. Thus, employing a variable inlet Mach number input would greatly complement the code.

Regarding the numerical framework used, similarly to previous works, the flow through the nozzle was assumed to be cold air with no reacting chemical species, with the nozzle inlet temperature being the same as the ambient temperature. In reality, the flow coming from the combustor section has an elevated temperature and chemical reactions from the combustion can still be taking place. Thus, simulations could be conducted taking into account these flow conditions at the end of the combustor section.

Moreover, varying other parameters other than the operating NPR and investigate their effect on the exhaust flow-field and overall SERN performance, or even conduct a transient simulation would greatly complement the work. Such parameters could be the free-stream Mach number, or the pressure and temperature of the ambient conditions.

Furthermore, it would be interesting to investigate the effect of a variable the geometry in the SERN, by changing the angle of the lower flap with respect to the y axis.

Bibliography

[1] I. M. Hall, "Inversion of the prandtl-meyer relation," *The Aeronautical Journal (1968)*, vol. 79, no. 777, p. 417–418, 1975. xii, 49, 95

[2] R. Fry, "A century of ramjet propulsion technology evolution," *Journal of Propulsion and Power*, vol. 20, pp. 27–58, 2004. xiii, 7

[3] Y. Yu, J. Xu, J. Mo, and M. Wang, "Numerical investigation of separation pattern and separation pattern transition in overexpanded single expansion ramp nozzle," *Aeronautical Journal*, vol. 118, pp. 399–424, 04 2014. xiii, 8, 12, 14, 15

[4] J. Anderson, *Modern Compressible Flow: With Historical Perspective*, ser. Aeronautical and Aerospace Engineering Series. McGraw-Hill Education, 2003. [Online]. Available: https://books.google.pt/books?id=woeqa4-a5EgC xiii, xvii, 9, 16, 18, 19, 21, 27, 28, 30, 32, 34, 50

[5] T. Croteau, "Micro-nozzle simulation and test for an electrothermal plasma thruster," 12 2018. xiii, 10

[6] M. Frey, K. Makowka, and T. Aichner, "The tictop nozzle — a new nozzle contouring concept," 05 2016. xiii, 11

[7] N. P. on Technology Enhanced Learning. (2011) Application of method of characteristics. [Online]. Available: https://nptel.ac.in/courses/112/103/112103021/ xiii, 12

[8] Y. Yu, J. Xu, K. Yu, and J. Mo, "Unsteady transitions of separation patterns in single expansion ramp nozzle," *Shock Waves*, vol. 25, no. 6, pp. 623–633, Nov. 2015. xiii, xiv, 14, 15, 63, 64, 66

[9] H.-J. Odenthal, P. Grygorov, M. Reifferscheid, and J. Schlüter, "Advanced blowing and stirring conditions in the bof process," 05 2013. xiii, 25

[10] (2018) Shock diamonds and mach disks. [Online]. Available: http://www.aerospaceweb.org/question/propulsion/q0224.shtml xiii, 26

[11] A. Inc., "Ansys fluent 12.0 theory guide," Available at https://www.afs.enea.it/project/neptunius/docs/fluent/html/th/main_pre.htm (2009/01/23). xiii, 35, 40, 41, 42, 43, 44

[12] Z. Toufik and Y. ZineEddine, "Supersonic two-dimensional minimum length nozzle

design at high temperature. application for air," *Chinese Journal of Aeronautics*, vol. 20, no. 1, pp. 29–39, 2007. [Online]. Available: https://www.sciencedirect.com/science/article/pii/S1000936107600041 xiii, 47

[13] W. Heiser, D. Pratt, U. Mehta, and D. Daley, *Hypersonic Airbreathing Propulsion*, ser. AIAA Textbooks Series. American Institute of Aeronautics and Astronautics, 1994. [Online]. Available: https://books.google.pt/books?id=d1sQvT2_kMsC xiv, 59, 67

[14] L. Fu, S. Zhang, and Y. Zheng, "Performances analysis of asymmetric minimum length nozzles," *International Journal of Modeling, Simulation, and Scientific Computing*, vol. 07, no. 02, p. 1650021, 2016. [Online]. Available: https://doi.org/10.1142/S1793962316500215 xvii, 55, 57

[15] E. Britannica. Supersonic flight. [Online]. Available: https://www.britannica.com/technology/supersonic-flight 1

[16] (2021) Lockheed sr-71 blackbird. [Online]. Available: https://en.wikipedia.org/wiki/Lockheed_SR-71_Blackbird#Records 1

[17] A. Ridgway, A. A. Sam, and A. Pesyridis, "Modelling a hypersonic single expansion ramp nozzle of a hypersonic aircraft through parametric studies," *Energies*, vol. 11, no. 12, 2018. [Online]. Available: https://www.mdpi.com/1996-1073/11/12/3449 5, 6, 13

[18] (2020) Lockheed martin corporation. creating the blackbird. [Online]. Available: http://www.lockheedmartin.co.uk/us/100years/stories/blackbird.html 5

[19] D. Jenkins, *X-15: Extending the Frontiers of Flight*, ser. NASA SP. NASA, 2007. [Online]. Available: https://books.google.pt/books?id=fOU4cGDWDjkC 5

[20] B. Calvert, *Flying Concorde: The Full Story*. Crowood Press UK, 2002. [Online]. Available: https://books.google.pt/books?id=tNDtNwAACAAJ 6

[21] R. Baidya, A. Pesyridis, and M. Cooper, "Ramjet nozzle analysis for transport aircraft configuration for sustained hypersonic flight," *Applied Sciences*, vol. 8, no. 4, 2018. [Online]. Available: https://www.mdpi.com/2076-3417/8/4/574 6, 8, 10, 25, 26

[22] Boom - supersonic passenger airplanes. [Online]. Available: https://boomsupersonic.com/ 6

[23] Aerion supersonic: The new sustainable supersonic aircraft. [Online]. Available: https://aerionsupersonic.com/ 6

[24] Hermeus | mach 5 aircraft | georgia. [Online]. Available: https://www.hermeus.com/ 6

[25] S. M. Neill and A. Pesyridis, "Modeling of supersonic combustion systems for sustained hypersonic flight," *Energies*, vol. 10, no. 11, 2017. [Online]. Available: https://www.mdpi.com/1996-1073/10/11/1900 6

[26] J. Borgon, "Limitations in the operational range of turbojet engines," *Technica Lotnicza Astronautyczna*, vol. 32, 1977. 6

[27] K. Roberts and D. Wilson, "Analysis and design of a hypersonic scramjet engine with a transition mach number of 4.00," *47th AIAA Aerospace Sciences Meeting including the New Horizons Forum and Aerospace Exposition*, 01 2009. 7

[28] E. Curran and S. Murthy, *Scramjet Propulsion*, ser. Progress in astronautics and aeronautics. American Institute of Aeronautics & Astronautics, 2001. [Online]. Available: https://books.google.lk/books?id=bzhwWw7eAr0C 7, 13

[29] T. Kanda, K. Tani, and K. Kudo, "Conceptual study of a rocket-ramjet combined-cycle engine for an aerospace plane," *Journal of Propulsion and Power - J PROPUL POWER*, vol. 23, pp. 301–309, 03 2007. 8

[30] E. Ekanayake, J. Gear, and Y. Ding, "Flow simulation of a two dimensional rectangular supersonic convergent divergent nozzle," *ANZIAM Journal*, vol. 51, 01 2009. 10

[31] M. Kirk, D.R.; Archambault. (2017) Mae 4262: Rockets and mission analysis. 10

[32] K. Foelsch, "The analytical design of an axially symmetric laval nozzle for a parallel and uniform jet," *Journal of the Aeronautical Sciences*, vol. 16, pp. 161–166, 1949. 11

[33] K. Davis, E. Fortner, M. Heard, H. McCallum, and H. Putzke, *Experimental and Computational Investigation of a Dual-Bell Nozzle*. [Online]. Available: https: //arc.aiaa.org/doi/abs/10.2514/6.2015-0377 11

[34] G. V. R. RAO, "Exhaust nozzle contour for optimum thrust," *Journal of Jet Propulsion*, vol. 28, no. 6, pp. 377–382, 1958. [Online]. Available: https://doi.org/10.2514/8.7324 11

[35] G. Hagemann, H. Immich, T. Van Nguyen, and G. E. Dumnov, "Advanced rocket nozzles," *Journal of Propulsion and Power*, vol. 14, no. 5, pp. 620–634, 1998. [Online]. Available: https://doi.org/10.2514/2.5354 11

[36] P. K and D. S. Khandai, "Experimental studyof single expansion ramp nozzle flows

(sern) at low supersonic speeds," *International Journal of Mechanical & Mechatronics Engineering*, vol. 14, p. 84, 10 2014. 12

[37] N. News. (2007) Faster than a speeding bullet: Guinness recognizes nasa scramjet. [Online]. Available: https://www.nasa.gov/home/hqnews/2005/jun/HQ_05_156_X43A_Guinness.html 13

[38] J. Bowers, D.; Laughrey, "Survey on techniques used in aerodynamic nozzle airframe integration," *Advisory Group for Aerospace Research and Development: Neuilly sur Seine, France*, 1992. 13

[39] P. Perrier, M. Rapuc, P. Rostand, R. Hallard, D. Regard, A. Dufour, and O. Penanhoat, *Nozzle and afterbody design for hypersonic airbreathing vehicles*. [Online]. Available: https://arc.aiaa.org/doi/abs/10.2514/6.1996-4548 13

[40] B. Zellner, W. Sterr, and O. Herrmann, "Integration of Turbo-Expander and Turbo-Ramjet Engines in Hypersonic Vehicles," *Journal of Engineering for Gas Turbines and Power*, vol. 116, no. 1, pp. 90–97, 01 1994. [Online]. Available: https://doi.org/10.1115/1.2906815 13

[41] F. Nasuti and M. Onofri, "Shock structure in separated nozzle flows," *Shock Waves*, vol. 19, pp. 229–237, 07 2009. 14

[42] A. Hadjadj and M. Onofri, "Nozzle flow separation," *Shock Waves*, vol. 19, pp. 163–169, 07 2009. 14

[43] J. Xu, J. Sha, Z. Shi, and K. Zhang, *PIV Experimental Study and Numerical Simulation of the Over-Expanded SERN Exit Jet*. [Online]. Available: https://arc.aiaa.org/doi/abs/10.2514/6.2008-99 14

[44] E. Gamble and D. Haid, *Improving Off-Design Nozzle Performance Using Fluidic Injection*. [Online]. Available: https://arc.aiaa.org/doi/abs/10.2514/6.2004-1206 14

[45] R. Schmucker, "Flow processes in overexpanded chemical rocket nozzles. part 1: Flow separation," 1984. 15

[46] Y. Yu, J. Xu, J. Mo, and M. Wang, "Principal parameters in flow separation patterns of over-expanded single expansion ramp nozzle," *Engineering Applications of Computational Fluid Mechanics*, vol. 8, no. 2, pp. 274–288, 2014. [Online]. Available: https://doi.org/10.1080/19942060.2014.11015513 15

[47] Y. Yu, "Over-expanded separation transitions of single expansion ramp nozzle in the accelerating and decelerating processes," *Aerospace Science and Technology*, vol. 98,

p. 105674, 2020. [Online]. Available: https://www.sciencedirect.com/science/article/pii/S1270963819327543 15

[48] T. Benson. (2014) Nasa, specific heat capacity: Calorically imperfect gas. [Online]. Available: https://www.grc.nasa.gov/www/BGH/realspec.html 17

[49] (2021) Heat capacity ratio. [Online]. Available: https://en.wikipedia.org/wiki/Heat_capacity_ratio 17

[50] (2020) Compressible flow. [Online]. Available: https://en.wikipedia.org/wiki/Compressible_flow 18

[51] N. Hall. (2019) Nasa, mach number. [Online]. Available: https://www.grc.nasa.gov/www/k-12/airplane/mach.html 19

[52] Computational fluid dynamics. [Online]. Available: https://en.wikipedia.org/wiki/Computational_fluid_dynamics 35

Appendix A

Numerical Inversion of the Prandtl-Meyer Relation [1]

$$\lambda = \sqrt{\frac{\gamma - 1}{\gamma + 1}} \quad \text{(A.1)}$$

$$\nu_\infty = \frac{\pi}{2}\left(\frac{1}{\lambda} - 1\right) \quad \text{(A.2)}$$

$$y = \left(\frac{\nu}{\nu_\infty}\right)^{2/3} \quad \text{(A.3)}$$

$$K = \frac{4}{3\pi}\left(1 + \frac{1}{\lambda}\right) \quad \text{(A.4)}$$

$$\eta_\infty = \left(\frac{3\pi}{2\lambda(1+\lambda)}\right)^{2/3} \quad \text{(A.5)}$$

$$a_1 = \frac{1}{2}\eta_\infty \quad \text{(A.6)}$$

$$a_2 = \frac{3 + 8\lambda^2}{40}\eta_\infty^2 \quad \text{(A.7)}$$

$$a_3 = \frac{-1 + 328\lambda^2 + 104\lambda^4}{2800}\eta_\infty^3 \quad \text{(A.8)}$$

$$d_1 = a_1 - 1 - \frac{a_3 - K}{a_2 - K} \quad \text{(A.9)}$$

$$d_2 = a_2 - a_1 - \frac{(a_1 - 1)(a_3 - K)}{a_2 - K} \quad \text{(A.10)}$$

$$d_3 = \frac{(a_3 - K)(a_1 - K)}{a_2 - K} - a_2 + K \quad \text{(A.11)}$$

$$e_1 = -1 - \frac{a_3 - K}{a_2 - K} = -1 - e_2 \quad \text{(A.12)}$$

$$M = \frac{1 + d_1 y + d_2 y^2 - d_3 y^3}{1 - e_1 y - e_2 y^2} \quad \text{(A.13)}$$

Appendix B

Python Algorithm

```
import math
import numpy as np
import matplotlib.pyplot as plt
from matplotlib import pylab
import pandas as pd
from google.colab import files

'FUNCTIONS'

def atm(h):
  if h > 25000:
    T = -131.21 + 0.00299 * h
    p = 1000*(2.488*((T+273.1)/216.6)**-11.388)
    rho = p / (0.2869 * (T+273.1))
  elif h > 11000 and h <= 25000:
    T = -56.46
    p = 1000*(22.65*math.exp(1.73-0.000157*h))
    rho = p / (0.2869 * (T+273.1))
  else:
    T = 15.04 - 0.00649 * h
    p = 1000*(101.29 * ((T + 273.1)/288.08)**5.256)
    rho = p / (0.2869 * (T+273.1))
  return T, p, rho

def InvPM(v):
  v = v*math.pi/180
  A = 1.3604
  B = 0.0962
  C = -0.5127
  D = -0.6722
  E = -0.3278
  v_0 = 0.5*math.pi*(math.sqrt(6)-1)
  y = (v/v_0)**(2/3)
  return (1+A*y+B*y**2+C*y**3)/(1+D*y+E*y**2)
```

```
def InvPM_(v, gamma):
  v = v*math.pi/180
  lbd = math.sqrt((gamma-1)/(gamma+1))
  v_0 = 0.5*math.pi*(1/lbd -1)
  y = (v/v_0)**(2/3)
  K = (4/(3*math.pi)) * (1 + 1/lbd)
  eta_0 = ((3*math.pi) / (2*lbd*(1+lbd)))**(2/3)
  a1 = 0.5*eta_0
  a2 = ((3 + 8*lbd**2)/40) * eta_0**2
  a3 = ((-1 + 328*lbd**2 + 104*lbd**4) / 2800 ) * eta_0**3
  d1 = a1 - 1 - ((a3 - K)/(a2 - K))
  d2 = a2 - a1 - (((a1-1)*(a3-K))/(a2-K))
  d3 = (((a3-K)*(a1-K)) / (a2-K) ) - a2 + K
  e1 = -1 - ((a3-K) / (a2-K))
  e2 = ((a3-K) / (a2-K))
  return (1 + d1*y + d2*y**2 + d3*y**3) / (1 + e1*y + e2*y**2)

def Mu(M):
  return math.asin(1/M) * (180/math.pi)

def PM(M,gamma):
  return math.sqrt((gamma+1)/(gamma-1))*math.atan(math.sqrt((gamma-1)/(gamma
      +1)*(M**2-1)))-math.atan(math.sqrt(M**2-1))

def PM_(Me, Mi, gamma):
  return math.sqrt((gamma+1)/(gamma-1)) * (math.atan(math.sqrt((gamma-1)/(
      gamma+1)*(Me**2-1))) - math.atan(math.sqrt((gamma-1)/(gamma+1)*(Mi
      **2-1)))) - (math.atan(math.sqrt(Me**2-1)) - math.atan(math.sqrt(Mi
      **2-1)))

def npr(gamma, Me): # NPR = Pt / P
  return (1+((gamma-1)/2)*Me**2)**(gamma/(gamma-1))

def nar(gamma, mach): # NAR = Ae / At
  return ((gamma + 1)/2)**(-(gamma+1)/(2*(gamma-1))) * ((1+((gamma-1)/2)*mach
      **2)**((gamma+1)/(2*(gamma-1)))) / mach

def M_e(gamma, npr):
  return (2/(gamma-1))**0.5 * (npr**((gamma-1)/gamma) - 1)**0.5

def moc2d(theta_max, theta_0, n):
  dtheta = (theta_max - theta_0) / (n-1)
```

```
node = int(0.5*n*(4+n-1))
theta = np.zeros(node)
v = np.zeros(node)
KL = np.zeros(node)
KR = np.zeros(node)
for i in range(0,n):
  theta[i] = theta_0 + i*dtheta
  v[i] = theta[i]
  KL[i] = theta[i]-v[i]
  KR[i] = theta[i]+v[i]
theta[n] = theta[n-1]
v[n] = v[n-1]
KL[n] = KL[n-1]
KR[n] = KR[n-1]
p = 1
q = n+1
for k in range(0, n-1):
  j = p
  h = q
  theta[h] = 0
  KR[h] = KR[j]
  v[h] = KR[j] - theta[h]
  KL[h] = theta[h] - v[h]
  j = j+1
  for i in range(h+1, n-p+q):
        KR[i] = KR[j]
        KL[i] = KL[i-1]
        theta[i] = 0.5*(KL[i]+KR[i])
        v[i] = 0.5*(KR[i]-KL[i])
        j = j+1
  if i == n-p+q-1:
     h = i+1
  else:
     h = h+1
  theta[h] = theta[h-1]
  v[h] = v[h-1]
  KL[h] = KL[h-1]
  KR[h] = KR[h-1]
  p = p+1
  q = h+1
return theta, v, KL, KR
```

```
def cf(gamma, npr, nar, p_atm, p_e):
  p_t = npr*p_atm
  return math.sqrt(((2*gamma**2)/(gamma-1))*((2/(gamma+1))**((gamma+1)/(gamma
      -1)))*(1-(p_e/p_t)**((gamma-1)/gamma)) ) + nar*((p_e - p_atm)/p_t)

def ntr(gamma, mach):
  return (1+((gamma-1)/2)*mach**2)

def ndr(gamma, mach):
  return (1+((gamma-1)/2)*mach**2)**(1/(gamma-1))

def ME(gamma, p_atm, p_i, Mi):
  return math.sqrt(((((1+((gamma-1)/2)*Mi**2)**(gamma/(gamma-1)))/(p_atm/p_i)
      )**((gamma-1)/gamma) - 1) * (2/(gamma-1)))

def pe_pi(gamma, mi, me):
  return ((1+((gamma-1)/2)*mi**2) / ((1+((gamma-1)/2)*me**2)))**(gamma/(gamma
      -1))

def bl(x, y, me):
  if me <= 4:
    ep = 0.5
  elif me > 4 and me <= 8:
    ep = 0.075*me**2 - 0.65*me + 1.9
  else:
    ep = 0.25*me - 0.5
  div = np.array([])
  for i in range(x.size-1):
    div = np.append(div, np.rad2deg(np.arctan((y[i+1]-y[i])/(x[i+1]-x[i]))))
  div = np.append(div, 0)
  d_bl = np.array([])
  d_y = np.array([])
  d_x = np.array([])
  x_bl = np.array([])
  y_bl = np.array([])
  for i in range(x.size):
    d_bl = np.append(d_bl, x[i]*np.tan(np.tan(np.deg2rad(ep))))
    d_y = np.append(d_y, np.cos(np.deg2rad(div[i]))*d_bl[i])
    d_x = np.append(d_x, np.sin(np.deg2rad(div[i]))*d_bl[i])
    x_bl = np.append(x_bl, x[i]-d_x[i])
    y_bl = np.append(y_bl, y[i]+d_y[i])
  return x_bl, y_bl
```

```
g = np.array([1.4])
for i in range(0, g.size):
  gamma = g[i]
  print('gamma =', gamma)
  #w = np.arange(1, 5, 1)
  w = np.array([4])
  error_vals = np.array([])
  theta_max_vals = np.array([])
  kernel_x_len = np.array([])
  nozzle_x_len = np.array([])
  nar_vals = np.array([])
  npr_vals = np.array([])

  for i in range(0, w.size):
    'INPUTS'
    #gamma = 1.4
    Me = w[i]
    n = 100

    theta_max = PM(Me, gamma) * 180/(2*math.pi)
    theta_0 = (theta_max/n)
    node = int(0.5*n*(4+n-1))

    theta_max_vals = np.append(theta_max_vals, theta_max)

    theta = moc2d(theta_max, theta_0, n)[0]
    mach = InvPM_(moc2d(theta_max, theta_0, n)[1], gamma)
    mu = np.zeros(node)

    wall_points_x = np.array([])
    wall_points_y = np.array([])
    kernel_points_x = np.array([])
    wall_mach = np.array([])
    kernel_mach = np.array([])
    wall_npr = np.array([])
    kernel_npr = np.array([])
    wall_ntr = np.array([])
    kernel_ntr = np.array([])
    wall_ndr = np.array([])
    kernel_ndr = np.array([])
```

```
'GRID GENERATION'
for i in range(0, node):
  mu[i] = Mu(mach[i])
x = np.zeros(node)
y = np.zeros(node)
wall = theta_max
D = 1
i = 0
while i<=n:
  if i==0:
    x[i] = -D/(math.tan(np.deg2rad(theta[i]-mu[i])))
    y[i] = 0
    plt.plot([0, x[i]], [D, y[i]], linewidth=1, color='blue')
    kernel_points_x = np.append(kernel_points_x, x[i])
    kernel_mach = np.append(kernel_mach, mach[i])
    kernel_npr = np.append(kernel_npr, npr(gamma, mach[i]))
    kernel_ntr = np.append(kernel_ntr, ntr(gamma, mach[i]))
    kernel_ndr = np.append(kernel_ndr, ndr(gamma, mach[i]))
  elif i==n:
    x[i] = (y[i-1] - D - x[i-1] * math.tan(np.deg2rad((theta[i-1] + theta
        [i] + mu[i-1] + mu[i])*0.5))) / ((math.tan(np.deg2rad(0.5*(wall+
        theta[i])))) - math.tan(np.deg2rad((theta[i-1]+theta[i]+mu[i-1]+mu
        [i])*0.5)))
    y[i] = D + x[i] * math.tan(np.deg2rad(0.5*(wall+theta[i])))
    plt.plot([x[i-1], x[i]], [y[i-1], y[i]], linewidth=1, color='blue')
    wall_points_x = np.append(wall_points_x, x[i])
    wall_points_y = np.append(wall_points_y, y[i])
    wall_mach = np.append(wall_mach, mach[i])
    wall_npr = np.append(wall_npr, npr(gamma, mach[i]))
    wall_ntr = np.append(wall_ntr, ntr(gamma, mach[i]))
    wall_ndr = np.append(wall_ndr, ndr(gamma, mach[i]))
    plt.plot([0, x[i]], [D, y[i]], linewidth=1, color='blue')
  else:
    x[i] = (D - y[i-1] + x[i-1] * math.tan(np.deg2rad(0.5*(mu[i-1]+theta[
        i-1]+mu[i]+theta[i])))) / ((math.tan(np.deg2rad(0.5*(mu[i-1] +
        theta[i-1] + mu[i] + theta[i] )))) - math.tan(np.deg2rad(theta[i]-
        mu[i])))
    y[i] = math.tan(np.deg2rad(theta[i]-mu[i])) * x[i] + D
    plt.plot([x[i-1], x[i]], [y[i-1], y[i]], linewidth=1, color='blue')
    plt.plot([0, x[i]], [D, y[i]], linewidth=1, color='blue')
  i = i+1
h = i
```

```
k = 0
i = h
for j in range(0, n-1):
  while i <= h+n-k-1:
    if i == h:
      x[i] = x[i-n+k] - y[i-n+k] / (math.tan(np.deg2rad(0.5*(theta[i-n+k]
          + theta[i] - mu[i-n+k] - mu[i]))))
      y[i] = 0
      plt.plot([x[i-n+k], x[i]], [y[i-n+k], y[i]], linewidth=1, color='
          blue')
      kernel_points_x = np.append(kernel_points_x, x[i])
      kernel_mach = np.append(kernel_mach, mach[i])
      kernel_npr = np.append(kernel_npr, npr(gamma, mach[i]))
      kernel_ntr = np.append(kernel_ntr, ntr(gamma, mach[i]))
      kernel_ndr = np.append(kernel_ndr, ndr(gamma, mach[i]))
    elif i == h+n-k-1:
      x[i] = (x[i-n+k] * math.tan(np.deg2rad(0.5*(theta[i-n+k] + theta[i])
          )) - y[i-n+k] + y[i-1] - x[i-1] * math.tan(np.deg2rad(0.5*(theta
          [i-1]+theta[i]+mu[i-1]+mu[i])))) / (math.tan(np.deg2rad(0.5*(
          theta[i-n+k]+theta[i]))) - math.tan(np.deg2rad(0.5*(theta[i-1]+
          theta[i]+mu[i-1]+mu[i]))))
      y[i] = y[i-n+k] + (x[i]-x[i-n+k]) * math.tan(np.deg2rad(0.5*(theta[i
          -n+k]+theta[i])))
      plt.plot([x[i-1], x[i]], [y[i-1], y[i]], linewidth=1, color='blue')
      wall_points_x = np.append(wall_points_x, x[i])
      wall_points_y = np.append(wall_points_y, y[i])
      wall_mach = np.append(wall_mach, mach[i])
      wall_npr = np.append(wall_npr, npr(gamma, mach[i]))
      wall_ntr = np.append(wall_ntr, ntr(gamma, mach[i]))
      wall_ndr = np.append(wall_ndr, ndr(gamma, mach[i]))
      plt.plot([x[i-n+k], x[i]], [y[i-n+k], y[i]], linewidth=1, color='
          blue')
    else:
      s1 = math.tan(np.deg2rad(0.5*(theta[i]+theta[i-1]+mu[i]+mu[i-1])))
      s2 = math.tan(np.deg2rad(0.5*(theta[i]+theta[i-n+k]-mu[i]-mu[i-n+k])
          ))
      x[i] = (y[i-n+k] - y[i-1] + s1 * x[i-1] - s2 * x[i-n+k]) / (s1-s2)
      y[i] = y[i-1] + (x[i]-x[i-1])*s1
      plt.plot([x[i-1], x[i]], [y[i-1], y[i]], linewidth=1, color='blue')
      plt.plot([x[i-n+k], x[i]], [y[i-n+k], y[i]], linewidth=1, color='
          blue')
    i = i+1
```

```
  k = k+1
  h = i
  i = h

wall_points_x = np.insert(wall_points_x, 0, 0)
wall_points_y = np.insert(wall_points_y, 0, 1)
wall_mach = np.insert(wall_mach, 0, 1)
wall_npr = np.insert(wall_npr, 0, npr(gamma, 1))
wall_ntr = np.insert(wall_ntr, 0, ntr(gamma, 1))
wall_ndr = np.insert(wall_ndr, 0, ndr(gamma, 1))
kernel_points_x = np.insert(kernel_points_x, 0, 0)
kernel_mach = np.insert(kernel_mach, 0, 1)
kernel_npr = np.insert(kernel_npr, 0, npr(gamma, 1))
kernel_ntr = np.insert(kernel_ntr, 0, ntr(gamma, 1))
kernel_ndr = np.insert(kernel_ndr, 0, ndr(gamma, 1))

print('Me =', Me)

kernel_x_len = np.append(kernel_x_len, kernel_points_x[-1])
nozzle_x_len = np.append(nozzle_x_len, wall_points_x[-1])
nar_vals = np.append(nar_vals, wall_points_y[-1])
npr_vals = np.append(npr_vals, npr(gamma, mach[-1]))

p_pt = (1+((gamma-1)/2)*mach**2)**(gamma/(gamma-1))
T_Tt = (1+((gamma-1)/2)*mach**2)**(-1)
rho_rhot = (1+((gamma-1)/2)*mach**2)**(-1/(gamma-1))
A_At = ((gamma + 1)/2)**(-(gamma+1)/(2*(gamma-1))) * ((1+((gamma-1)/2)*
    mach**2)**((gamma+1)/(2*(gamma-1)))) / mach

error = (np.abs(y[-1] - nar(gamma, Me)) / nar(gamma, Me)) * 100
error_vals = np.append(error_vals, error)
print('error =', error)

'PLOTS'
pylab.rcParams['figure.figsize'] = (20,10)
plt.xlabel('x/y*')
plt.ylabel('y/y*')
plt.xlim(0,x[-1]+x[-1]*0.1)
plt.ylim(0,y[-1]+y[-1]*0.1)
plt.gca().set_aspect('equal', adjustable='box')
#plt.plot(x,y,'o',color='blue')
plt.show()
```

```
    # plt.plot(wall_points_x, wall_points_y, label = 'gamma = %s' %gamma)
    # plt.xlabel('x/y*')
    # plt.ylabel('y/y*')
    # plt.legend()
    # plt.xlim(0, 11)
    # plt.ylim(0, 3.5)
    # plt.gca().set_aspect('equal', adjustable='box')
    #plt.show()
  #plt.show()

    #pylab.rcParams['figure.figsize'] = (8, 6)
    #plt.plot(kernel_points_x, kernel_ndr**-1, label = 'gamma = %s' %gamma)
    #plt.legend()
    #plt.xlabel('x / y*')
    #plt.ylabel('rho / rho_0 (Lower Flap)')
    #plt.show()
#plt.show()

def fill():
  'FILL INITIAL CONTOUR ZONE'
  x = np.insert(x, 0, 0)
  x = np.insert(x, 0, 0)
  y = np.insert(y, 0, 1)
  y = np.insert(y, 0, 0)
  mach = np.insert(mach, 0, 1)
  mach = np.insert(mach, 0, 1)
  p_pt = np.insert(p_pt, 0, (1+((gamma-1)/2)*1**2)**(gamma/(gamma-1)))
  p_pt = np.insert(p_pt, 0, (1+((gamma-1)/2)*1**2)**(gamma/(gamma-1)))
  T_Tt = np.insert(T_Tt, 0, (1+((gamma-1)/2)*1**2)**(-1))
  T_Tt = np.insert(T_Tt, 0, (1+((gamma-1)/2)*1**2)**(-1))
  rho_rhot = np.insert(rho_rhot, 0, (1+((gamma-1)/2)*1**2)**(-1/(gamma-1)))
  rho_rhot = np.insert(rho_rhot, 0, (1+((gamma-1)/2)*1**2)**(-1/(gamma-1)))
  A_At = np.insert(A_At, 0, ((gamma + 1)/2)**(-(gamma+1)/(2*(gamma-1))) *
      ((1+((gamma-1)/2)*1**2)**((gamma+1)/(2*(gamma-1)))) / 1)
  A_At = np.insert(A_At, 0, ((gamma + 1)/2)**(-(gamma+1)/(2*(gamma-1))) *
      ((1+((gamma-1)/2)*1**2)**((gamma+1)/(2*(gamma-1)))) / 1)
  return
def contours():
  plt.tricontourf(x, y, mach, mach.size, cmap='jet')
  plt.xlim(0,x[-1]+x[-1]*0.1)
  plt.ylim(0,y[-1]+y[-1]*0.1)
```

```
  plt.xlabel('x/y*')
  plt.ylabel('y/y*')
  plt.gca().set_aspect('equal', adjustable='box')
  tick_m = np.linspace(mach[0], mach[-1], 10)
  plt.colorbar(label ='Mach', shrink = 0.5, ticks=tick_m)
  plt.show()

  plt.tricontourf(x, y, p_pt**-1, p_pt.size, cmap='jet')
  plt.xlim(0,x[-1]+x[-1]*0.1)
  plt.ylim(0,y[-1]+y[-1]*0.1)
  plt.xlabel('x/y*')
  plt.ylabel('y/y*')
  plt.gca().set_aspect('equal', adjustable='box')
  tick_p = np.linspace(p_pt[0]**-1, p_pt[-1]**-1, 10)
  plt.colorbar(label ='p / p_0', shrink = 0.5, ticks=tick_p)
  plt.show()

  plt.tricontourf(x, y, T_Tt, T_Tt.size, cmap='jet')
  plt.xlim(0,x[-1]+x[-1]*0.1)
  plt.ylim(0,y[-1]+y[-1]*0.1)
  plt.xlabel('x/y*')
  plt.ylabel('y/y*')
  plt.gca().set_aspect('equal', adjustable='box')
  tick_t = np.linspace(T_Tt[0], T_Tt[-1], 10)
  plt.colorbar(label ='T / T_0', shrink = 0.5, ticks=tick_t)
  plt.show()

  plt.tricontourf(x, y, rho_rhot, rho_rhot.size, cmap='jet')
  plt.xlim(0,x[-1]+x[-1]*0.1)
  plt.ylim(0,y[-1]+y[-1]*0.1)
  plt.xlabel('x/y*')
  plt.ylabel('y/y*')
  plt.gca().set_aspect('equal', adjustable='box')
  tick_rho = np.linspace(rho_rhot[0], rho_rhot[-1], 10)
  plt.colorbar(label ='rho / rho_0', shrink = 0.5, ticks=tick_rho)
  plt.show()
  return

print('x kernel =', kernel_x_len)
print('x ramp =', wall_points_x[-1])
print('y ramp =', wall_points_y[-1])
print(kernel_points_x.size, wall_points_x.size)
```

```
wall_points_xy = np.column_stack((wall_points_x, wall_points_y))

bl_wall_points_x = bl(wall_points_x, wall_points_y,w)[0]
bl_wall_points_y = bl(wall_points_x, wall_points_y,w)[1]
bl_wall_points_xy = np.column_stack((bl_wall_points_x, bl_wall_points_y))

pylab.rcParams['figure.figsize'] = (20,10)
plt.gca().set_aspect('equal', adjustable='box')
plt.xlabel('x/y*')
plt.ylabel('y/y*')
plt.xlim(0,wall_points_x[-1]+wall_points_x[-1]*0.1)
plt.ylim(0,wall_points_y[-1]+wall_points_y[-1]*0.1)
plt.plot(wall_points_x, wall_points_y, label='Inviscid Contour')
plt.plot(bl(wall_points_x, wall_points_y,w)[0], bl(wall_points_x,
    wall_points_y,w)[1], label='Boundary Layer Corrected Contour')
plt.legend()
plt.show()

pylab.rcParams['figure.figsize'] = (20,10)
plt.gca().set_aspect('equal', adjustable='box')
plt.xlabel('x/y*')
plt.ylabel('y/y*')
#plt.xlim(0,wall_points_x[-1]+wall_points_x[-1]*0.1)
plt.xlim(0, 35)
plt.ylim(-1,wall_points_y[-1]+wall_points_y[-1]*0.1)
#plt.plot(wall_points_x, wall_points_y, label='Inviscid Contour')
plt.plot(bl(wall_points_x, wall_points_y,w)[0], bl(wall_points_x,
    wall_points_y,w)[1],'b', label='Boundary Layer Corrected Contour')
plt.plot([0, 11.548], [0, 0], 'b')
plt.plot([31.89519, 31.89519], [6, 12], 'b')
#plt.legend()
plt.show()

  #div = np.rad2deg(np.atan((y[])))

#np.savetxt('nozzle.csv', wall_points_xy, delimiter=',')
#files.download('nozzle.csv')
#np.savetxt('nozzle_bl.csv', bl_wall_points_xy, delimiter=',')
#files.download('nozzle_bl.csv')
```